MICROSTRUCTURE AND TEXTURE STUDIES ON MAGNESIUM SHEET ALLOYS

By

Mohsen Masoumi

A Thesis Submitted to the Faculty of Graduate Studies and Research in Partial Fulfillment of the Requirements for the Degree of Doctor of Philosophy

Department of Mining and Materials Engineering

McGill University

Montreal, Canada

May 2011

ABSTRACT

Automotive applications of magnesium alloys have received significant attention for the purpose of vehicle weight reduction. Magnesium sheet can be used for automotive body panels and closures. However, due to several heating and rolling processes required to manufacture Mg sheet, production costs by conventional processes are relatively high. Twin-roll casting (TRC) is a process which can reduce the production costs of magnesium sheet by reducing the number of processing steps.

AZ31 (Mg-3wt.%Al-1wt.%Zn), the most common Mg sheet alloy, is currently produced by hot rolling of the direct chill (DC) cast ingot. In general, Mg wrought alloys have limited formability due to a hexagonal close-packed structure and preferred orientation (known as texture). Twin-roll cast sheet products usually differ from conventional ingot-cast and rolled products exhibiting weaker textures as known in aluminum sheet production. In order to improve magnesium sheet formability, a better understanding of microstructure and texture evolution after twin-roll casting is necessary. The primary objectives of this research were to study the microstructure and texture evolution in twin-roll cast AZ31 Mg sheet alloy and to develop alloy compositions with improved mechanical properties (i.e. weakened texture of the sheet product). New alloys were based on Mg-Mn and Mg-Zn alloys with Ce and Sr additions. Experimental techniques such as optical microscopy, thermal analysis, Scanning Electron Microscopy (SEM), Energy Dispersive Spectrometry (EDS), Electron Probe Micro-Analysis (EPMA), Electron Back Scattering Diffraction (EBSD) and X-ray diffraction were used to thoroughly characterise the materials microstructure and texture.

In the first part of this study, the influence of cooling rate (CR) on the casting microstructure of AZ31 magnesium alloy was investigated, as a background to understand microstructural development in TRC AZ31. This was achieved by using different moulds to obtain slow to moderate cooling rates. It was found that the grain size and secondary dendrite arm spacing (SDAS) reduces as the cooling rate increases. SDAS, λ, was related to cooling rate as $\lambda = 85.15(CR)^{-0.42}$, where λ is in μm and CR is cooling rate in ^{o}C/s. Additionally it was observed that with an increase in CR the fraction of

second phase particles increased and the second phase particles became finer.

The second part of this study characterised the microstructure and texture of the TRC AZ31 (Mg-3wt.%Al-1wt.%Zn) sheet. The results indicated that TRC AZ31 exhibited a dendritic microstructure with columnar and equiaxed grains. The TRC alloy contained Al-Mn and Mg-Al-Zn second-phase particles that are approximately 1μm in size and were more abundant than in conventionally cast AZ31. The heterogeneous structure was attributed to the effect of the CR, which varies from ~325 ^{o}C/s on the surface to ~150 ^{o}C/s in the mid-thickness of the sheet. No surface segregation was detected, however, a certain degree of macrosegregation was observed in the mid-thickness which persists after annealing and rolling. Recrystallization at 420 ^{o}C lead to a bimodal grain-size distribution, while a fine-grain structure was obtained after rolling and annealing. The TRC AZ31 sheet exhibited basal textures in the as-received, rolled and rolled-annealed conditions. Significantly, post-annealing of TRC AZ31 at 420 ^{o}C produced a relatively random texture that has not previously been observed in the conventional AZ31 sheet. This texture randomization was attributed to the particle-stimulated nucleation of new grains in the TRC structure. Preliminary mechanical analyses indicated that such annealing treatment slightly increases the ultimate tensile strength (UTS), but significantly improves elongation.

In the final of part of the study, the microstructures and textures of rolled and rolled-annealed Mg-1wt.%Mn-based and Mg-1wt.%Zn-based alloys containing different levels of Ce and Sr were examined. Addition of Ce refined the as-cast and rolled-annealed grain structure of Mg-1wt.%Mn (M1) alloy. The overall texture intensity of basal poles were weakened for both rolled and rolled-annealed Mg-Mn-Ce alloys compared to the M1 alloy. This texture weakening was attributed to the solid solubility of Ce in Mg rather than particle stimulated nucleation (PSN) or *c/a* ratio alteration. Addition of Sr also refined the rolled-annealed grain structure of M1 alloy. The overall texture intensity of basal poles were weakened for both rolled and rolled-annealed Mg-1wt.%Mn-Sr (MJ) alloys containing 0.5 and 1.0 wt% Sr, compared to the M1 alloy. The texture weakening was attributed to PSN of new grains with random orientations. Sr addition also refined the as-cast and rolled-annealed grain structure of Mg-1wt.%Zn (Z1)

alloy. The overall texture intensity of basal poles were weakened for rolled and rolled-annealed Mg-Zn-Sr (ZJ) alloys compared to the Z1 alloy. As with the M1 alloy, the texture weakening was also attributed to particle stimulated nucleation (PSN).

RÉSUMÉ

Les applications automobiles des alliages de magnésium ont reçu une attention particulière pour la réduction de poids des véhicules. La feuille de magnésium peut être utilisée pour les panneaux de carrosserie automobile et pour les portières. Toutefois, en raison de plusieurs procédés de chauffage et de laminage, la production de feuilles de magnésium par un procédé classique est relativement coûteuse. La coulée entre des cylindres est un procédé qui peut réduire le coût de production des tôles de magnésium en réduisant les étapes de traitement.

L'alliage de magnésium AZ31 (Mg-3%Al-1% Zn), est l'alliage commun le plus utilisé pour la production de la feuille de magnésium. La feuille est actuellement produite par le procédé de coulée semi-continue. En général, les alliages de magnésium pour le laminage, sont limités au niveau de la formabilité en raison de leur structure cristalline hexagonale compacte et aussi à cause de l'orientation préférentielle de leur texture. Les produits fabriqués à partir du procédé de coulée entre des cylindres de la feuille de magnésium sont généralement différents de ceux fabriqués à partir de lingots coulés et laminés par le procédé conventionnel comme par exemple pour la production de la feuille d'aluminium. Ils démontrent aussi une texture plus faible. Il est par conséquent important d' utiliser le procédé de coulée entre des cylindres pour les alliages actuels de magnésium et également de développer de nouveaux alliages de magnésium qui seront plus appropriés pour le procédé de coulée entre des cylindres. Afin d'améliorer la formabilité de la feuille de magnésium, une bonne compréhension de la microstructure et de l'évolution de la texture lors de la coulée entre des cylindres est nécessaire.

Les principaux objectifs de cette recherche ont été d'étudier la microstructure et l'évolution de texture de la feuille d'alliage de magnésium AZ31 coulée entre deux cylindres et de développer ou de modifier la composition des alliages afin d'obtenir des propriétés mécaniques améliorées (i.e. textures affaiblie de la fiche produit). Les nouveaux alliages étudiés dans ce travail de recherche ont été faits à partir des systèmes binaires de Mg-Mn et Mg-Zn avec des ajouts de cérium et de strontium. Les alliages sont alors synthétisés, coulés et laminés dans notre laboratoire. Les techniques

expérimentales telles que : la microscopie optique, l'analyse thermique, la microscopie électronique à balayage (MEB), la spectroscopie à l'énergie dispersive (EDS), la micro-sonde (EPMA), la diffraction par électrons rétrodiffusés (EPCA) et diffraction des rayons X ont été utilisés pour les analyses de la microstructure et de la texture.

Dans la première partie de cette présente étude, l'influence de la vitesse de refroidissement sur la structure de coulée de l'alliage de magnésium AZ31 a été étudiée à titre de référence et dans le but de comprendre le développement de la microstructure de l'alliage AZ31 coulé entre des cylindres. Ce travail a été effectué en utilisant différents types de moules afin d'obtenir des taux de refroidissement de lent à modéré. Il a été alors possible de constater que la taille des grains et l'espacement entre les bras des dendrites secondaires diminuent à mesure que les taux de refroidissement augmentent. L'espacement entre les bras des dendrites secondaires, λ, est lié à la vitesse de refroidissement alors que $\lambda = 85.15^{-0,42}$ (taux de refroidissement) où λ est en microns et le taux de refroidissement en degrés Celsius/seconde. En outre, il a été observé qu'une augmentation du taux de refroidissement a pour effet d'augmenter la dispersion des particules de phases secondaires et celles-ci deviennent alors plus fines.

La deuxième partie a été axée plus spécifiquement sur l'étude de la microstructure et de la texture de la feuille d'alliage de magnésium AZ31 (Mg-3%Al-1% Zn) coulée entre deux cylindres. Les résultats indiquent que la feuille d'alliage AZ31 coulée entre deux cylindres présente une microstructure dendritique avec des grains en colonnes et équiaxes. L'alliage de coulée entre des cylindres contient des particules de phase secondaire Al-Mn et Mg-Al-Zn qui sont de taille d'environ 1 micron. Il a été noté que la quantité de ces deux phases secondaires dans l'alliage de coulée entre des cylindres est supérieure à l'alliage usuel AZ31. La structure hétérogène a été attribuée à l'effet de la vitesse de refroidissement, qui varie d'environ 325 °C/s à la surface et d'environ 150 °C/s au niveau de la moitié de l'épaisseur de la feuille. Pas de ségrégation de surface a été détectée, mais un certain degré de macroségrégation a été observé dans la moitié de l'épaisseur et ce phénomène persiste même après le laminage et le recuit. La recristallisation effectuée à 420 °C conduit à une distribution de la granulométrie selon deux modes distincts, alors qu'une structure à grains fins est obtenue après le laminage et

le recuit. La feuille de AZ31 coulée entre deux cylindres laisse voir diverses textures de base (i) telle que reçue, (ii) telle que laminée et (iii) conditions de laminage et de recuit. Toutefois, après le recuit de la feuille de l'alliage AZ31 coulée entre des cylindres à 420 ^{o}C, un procédé développé dans cette étude, il est possible de voir une texture relativement aléatoire qui n'a pas été observée auparavant dans la feuille classique de l'alliage AZ31. La texture aléatoire est attribuée à la nucléation de particules stimulées par de nouveaux grains créés dans la structure lors de la coulée entre des cylindres. L'évaluation préliminaire des propriétés mécaniques indique que le traitement de recuit augmente légèrement la résistance à la rupture (UTS), mais améliore de façon significative l'allongement.

Dans la troisième partie de cette étude de nouvelles compositions d'alliage à base de Mg-1%Mn et Mg-1%Zn contenant différents niveaux de cérium et de strontium sont développées et analysées afin de mieux comprendre les microstructures et les textures dans les conditions de laminage et de recuit après le laminage. Il a été possible de constater que l'ajout de cérium affine la structure des grains dans les présentes conditions : telle que coulée et laminée-recuit pour l'alliage Mg-1%Mn (M1). De plus, l'intensité de la texture globale du plan de base a été réduite dans les conditions de laminage ainsi que laminage et recuit des alliages Mg-Mn-Ce comparativement à l'alliage M1. Le micromécanisme provocant l'affaiblissement de la texture a été expliqué par la solubilité solide du cérium dans le magnésium.

L'ajout de strontium affine également la structure de grain de l'alliage M1 après le traitement de laminage et de recuit. De plus, l'intensité globale de la texture des pôles des plans de base est affaiblie pour les alliages de Mg-1%Mn-Sr (MJ) contenant 0,5% et 1.0% de strontium en comparaison avec l'alliage M1.L'affaiblissement de la texture a été associe et explique par la nucleation de nouveaux grains relies a des particules stimulées montrant des orientations aléatoires. L'ajout de strontium affine aussi la structure de grain de l'alliage Mg-1%Zn de l'alliage Z1dans les conditions telle que coulée et laminé et recuit. En outre, l'intensité de la texture globale du pôle de base pour les alliages Mg-Zn-Sr (ZJ) a été affaiblie après le laminage ainsi que le laminage et le recuit par rapport à l'alliage Z1. L'affaiblissement de la texture a de nouveau été attribué à la nucléation de

particules stimulées. Ces alliages présentent un bon potentiel de dévelopment pour de futurs alliages de magnésium pour la coulée de tôles avec une formabilité améliorée.

ACKNOWLEDGEMENTS

I would like to express my deepest gratitude to my supervisor, Professor Mihriban Pekguleryuz, for her excellent supervision and providing me with the opportunity to undertake my PhD degree in the engineering materials program of McGill University. I was very impressed, not only by her solid knowledge of the physical metallurgy of light metals and her creativity in novel alloy development, but also by her personality and dedication to her students.

Special thanks go to Dr. Faramarz Zarandi and Dr. Majid Hoseini for valuable discussions and for sharing their knowledge and expertise. I am also grateful to Pierre Vermette for his in-depth industrial experience and for providing safety training for experimental procedures, Helen Campbell and Lang Shi for their help in electron microanalysis, and Barbara Hanley for keeping us informed and updated of research information.

Many thanks go to Xin Zhang, Yingling, Erol Ozbakir, Mert Celikin, Deniz Temur Sultan, Hemant Borkar, Alireza Sadeghi, Amir Farkoosh and Mandana Bornapour for helpful discussions during our group meetings. My appreciation also goes to my friends in the department, especially John Roumeliotis, Ahmad Rezaeian, Pantcho Stoyanov, Amir Farzadfar, Mehdi Sanjari, Hashem Mousavai, Ramona, Paula, Yaneth and Mayeli Alvarez Silva. They made my life at McGill more than just research. I will never forget the fun times at Graduate House and the graduate softball games we shared.

Last, but not least, I owe special thanks to my parents, brother, sisters and my nieces and nephews. I am always grateful for their enduring support and encouragement in every step in my life, career and study. This work would not have been possible without their endless love and support.

CONTRIBUTIONS OF AUTHORS

This thesis was prepared according to the guidelines for a manuscript-based thesis. These guidelines are published by the Graduate and Postdoctoral Studies office of McGill University. The information related to the authors of the manuscripts is cited as follows:

"In general, when co-authored papers are included in a thesis, the candidate must be the primary author (the author who has made the most substantial contribution) for all papers included in the thesis. In addition, the candidate is required to make an explicit statement in the thesis as to who contributed to such work and to what extent. This statement should appear in a single section entitled "Contributions of Authors" as a preface to the thesis. The supervisor must attest to the accuracy of this statement at the doctoral oral defence. Since the task of the examiners is made more difficult in these cases, it is in the candidate's interest to clearly specify the responsibilities of all the authors of the co-authored papers."

The following six manuscripts were used to prepare this thesis. The first three are incorporated in Chapter 3, appearing as sections 3.1, 3.2 and 3.3. The final three are included in Chapter 4, appearing as sections 4.1, 4.2, and 4.3, respectively. All the manuscripts have been published, accepted or submitted for publication as indicated.

1- **Masoumi M.**, Pekguleryuz, M., "Effect of Cooling Rate on the Microstructure of AZ31 Magnesium Alloy" Trans. Am. Foundry Soc., 2009, Vol. 117, pp. 617-626.
2- **Masoumi M.**, Zarandi, F., Pekguleryuz, M., "Alleviation of Basal Texture in Mg-3Al-1Zn" Scripta Mater., vol. 62, no 11, 2010, pp. 823-826
3- **Masoumi M.**, Zarandi, F., Pekguleryuz, M., "Microstructure and texture studies on twin-roll cast AZ31 alloy and the effect of thermomechanical processing" Mat. Sci. Eng. Vol. 528, no 3, 2011, pp. 1268-1279
4- **Masoumi, M.**, Hoseini, M., Pekguleryuz, M., "The influence of Ce on the microstructure and rolling texture of Mg–1%Mn alloy" Mat. Sci. Eng. A, Vol. 528, no 7-8, 2011, pp. 3122-3129
5- **Masoumi M.**, Pekguleryuz, M., "Effect of Sr on the texture of rolled Mg-Mn-based

alloys" submitted to Scripta Mater.

6- **Masoumi M.**, Pekguleryuz, M., "The influence of Sr on the Microstructure and Texture Evolution of Rolled Mg-1%Zn Alloy". Accepted for publication in Mat. Sci. Eng. A.

All the manuscripts are co-authored by Prof. M. O. Pekguleryuz, the research project supervisor. All the experiments were conducted by the candidate. Two of the manuscripts include Dr. Faramarz Zarandi (post-doctoral researcher, Department of Mining and Materials Engineering, McGill University) for his contribution in understanding the deformation structure and texture analysis. Manuscript 4 includes Dr. Majid Hoseini (Department of Mining and Materials Engineering, McGill University) for his contribution in texture analysis. All the work presented in this thesis, apart from the co-author contributions mentioned above, was performed by the candidate.

TABLE OF CONTENTS

ABSTRACT i
RESUMÉ iv
ACKNOWLEDGEMENTS viii
CONTRIBUTIONS OF AUTHORS ix
TABLE OF CONTENTS xi
LIST OF FIGURES xiv
LIST OF TABLES xx
CHAPTER 1 1
CHAPTER 2 6
2.1 Deformation Characteristics of Magnesium 6
2.1.1 Slip 6
2.1.2 Twinning 8
2.2 Magnesium Rolling Texture 10
2.3 Formability of Magnesium Alloys 11
2.4 Effect of Alloying Elements on Formability of Magnesium 13
2.4.1 Grain refining 13
2.4.2 Texture Weakening 14
2.5 Mg Sheet Alloys 18
2.5.1 Mg-Al-Based Alloys 18
2.5.2 Mg-Mn Based Alloys 18
2.5.3 Mg-Zn-Based Alloys 18
2.5.4 Mg-Li-Based Alloy 19
2.6 Magnesium Sheet Production 19
2.6.1 Conventional Magnesium Sheet Production 19
2.6.2 Twin-Roll Casting (TRC) 20
2.6.3 Twin Roll Casting of Magnesium 21
2.7 Summary 28
2.8 References 29

CHAPTER 3 3
3.1 Effect of Cooling Rate on the Microstructure of AZ31 Mg Alloy 35
3.1.1 Introduction 35
3.1.2 Experimental Procedure 37
3.1.3 Results and Discussion 39
3.1.4 Conclusions 47
3.1.5 References 47
3.2 Alleviation of Basal Texture in Twin-Roll Cast Mg-3Al-1Zn Alloy 49
3.2.1 Introduction 49
3.2.2 Experimental Procedure 50
3.2.3 Results and Discussion 51
3.2.4 References 56
3.3 Microstructure and Texture Studies on Twin-Roll Cast AZ31 Alloy and the Effect of Thermomechanical Processing 58
3.3.1 Introduction and Background 58
3.3.2 Experimental Procedure 60
3.3.3 Results and Discussion 62
3.3.3.1 Microstructure and texture of commercial AZ31-H24 sheet 62
3.3.3.2 TRC AZ31 62
3.3.3.3 Thermomechanically Treated TRC AZ31 71
3.3.3.4 The Tensile Properties of TRC AZ31 78
3.3.5 Conclusions 81
3.3.6 References 82
CHAPTER 4 85
4.1 The influence of Ce on the Microstructure and Rolling Texture of Mg-1%Mn alloy 86
4.1.1 Introduction 86
4.1.2 Experimental Procedure 88
4.1.3 Results and Discussion 89
4.1.3.1 As-cast Microstructures 89

4.1.3.2 Microstructures of rolled and rolled-annealedalloys 94
4.1.3.3 Texture of rolled and rolled-annealedalloys 95
4.1.3.4 The Mechanism of Texture Evolution in ME Alloys 98
4.1.4 Conclusions 100
4.1.5 References 101
4.2 Effect of Sr on the Microstructure and texture of rolled Mg-Mn -based alloys . 104
4.2.1 Introduction 104
4.2.2 Experimental Procedure 105
4.2.3 Results and Discussion 106
4.2.4 References 111
4.3 The influence of Sr on the Microstructure and Texture Evolution of Rolled Mg-1%Zn Alloy 113
4.3.1 Introduction and Background 113
4.3.2 Experimental Procedure 115
4.3.3 Results and Discussion 116
4.3.3.1 As-cast Microstructures 116
4.3.3.2 Microstructures of rolled and rolled-annealed alloys 119
4.3.3.3 Texture of rolled and rolled-annealed alloys 122
4.3.3.4 The Mechanism of Texture Evolution in ZJ Alloys 126
4.3.4 Conclusions 129
4.3.5 References 130
4.3 A Look at Texture Alteration Micro-Mechanisms in the Mg alloys Studied in this Thesis 133
4.4.1 References 136
CHAPTER 5 137
CHAPTER 6 141
Appendix 144

LIST OF FIGURES

Fig. 1.1 Process routes for hot strip production [15] 2
Fig. 2.1 Slip and twinning planes in HCP magnesium [3]..... 7
Fig. 2.2 The effect of deformation temperature on the CRSS value of slip systems and twinning in pure Mg [4]... 8
Fig. 2.3 Effect of alloying on CRSS for basal slip in Mg [3] 8
Fig. 2.4 The {10-12} tensile twinning system for magnesium 9
Fig. 2.5 Schematic diagram showing double twinning process: (a) {10-11} Twinning reorients the basal plane by 61.9^{o} (b) followed by retwinning on { 10-12} [16]..... 10
Fig. 2.6 {0002} Pole figures in AZ31 after hot rolling of cast material a) 250 ^{o}C) b) 400 ^{o}C [11]..... 11
Fig. 2.7 True stress-strain curve for low and high n-values values [21]..... 12
Fig. 2.8 Schematic depiction of strip caster by H. Bessemer strip caster patented in 1865 [52, 53]... 21
Fig. 2.9 Schematic view of twin roll caster with controlled parameters [51]..... 22
Fig. 2.10 Microstructure of as-cast Mg AZ31 sheet using twin-roll [50].... 24
Fig. 2.11 Micrographs of as TRC ZM61–Al alloys: (a) ZM61 (b) ZMA611 and (c) ZMA613 [71]..... 25
Fig. 2.12 Microstructure annealed Mg sheet in casting direction. (a) columnar region, and (b) central region [50] 25
Fig. 2.13 Microstructure of as-rolled AZ31 (a) twin-roll strip cast / warm rolled (b) DC cast / warm rolled commercial products[50]... 26
Fig. 2.14 Micrographs of TRC ZM61–Al alloys in T4 condition (a) ZM61, (b) ZMA611, (c, d) ZMA613 [71]..... 27
Fig. 2.15 Texture of the as-received TRC material (a) and upon annealing at 400 ^{o}C for 20 h (b) presented in terms of (0002) recalculated pole figures [73].... 29
Fig. 2.16 Texture development during rolling at 400 ^{o}C up to 90% final thickness reduction using 10% and 40% reduction per pass [73]..... 28

Fig. 3.1 (a) Induction furnace (b) Moulds used in thermal analysis. 38
Fig. 3.2 Cooling rate curves of solidifying AZ31B: (a) sand cup (b) graphite cup... . 39
Fig. 3.3 As-cast microstructure of AZ31 cast in (a) sand mould (b) steel thin- wall die (c) graphite mould (d) steel thick wall die (e) copper die, edge (f) copper die, mid-thickness. 40
Fig. 3.4 Effect of cooling rate on (a) grain size and (b) SDAS of AZ31B alloy 41
Fig. 3.5 The effect of cooling rate on the average size of secondary phases of AZ31 alloy..... 41
Fig. 3.6 The effect of cooling rate on the area fraction of secondary phases (fsp) of AZ31 alloy. 42
Fig. 3.7 SEM micrographs showing microstructure of AZ31 cast in copper die... 43
Fig. 3.8 EDS spectrum from the matrix in Fig. 3.7 43
Fig. 3.9 EDS spectrum from the Al-Mn particles in Fig. 3.7 43
Fig. 3.10 EDS spectrum from the Mg-Al-Zn particles in Fig. 3.7..... 44
Fig. 3.11 SEM micrographs showing microstructure of AZ31 cast in sand cup. 44
Fig. 3.12 EDS spectrum from the matrix in Fig. 3.11... 45
Fig. 3.13 EDS spectrum from the Al-Mn particles in Fig. 3.11 45
Fig. 3.14 EDS spectrum from the Mg-Al-Zn phases in Fig. 3.11..... 45
Fig. 3.15 Thickness microstructures (RD-ND plane) of commercial AZ31-H24 sheet; (a) before and (b) after annealing heat treatment at 420oC for one hour. (c) and (d) {0001} pole figures corresponding to (a) and (b), respectively. RD and TD are the sheet rolling and transverse directions, respectively. . 51
Fig. 3.16 RD-ND microstructure of the as-received TRC AZ31; (a) edge (b) mid-thickness. (c) {0001} pole figure and (d) EBSD map from RD-TD plane of the as-received TRC AZ31. ND is the sheet normal direction... 52
Fig. 3.17 Microstructures of the heat treated (one hour at 420 ^{o}C) TRC AZ31 in (a) edge and (b) mid-thickness. (c) {0001} pole figure of the heat treated TRC AZ31. (d) EBSD map of the RD-ND plane 54
Fig. 3.18 Simulated DC AZ31: (a) as-cast microstructure, (b) cold-rolled {0001} pole figure, and (c) annealed {0001} pole figure. Simulated TRC AZ31:

(d) as-cast thickness (RD-ND) microstructure, (e) cold-rolled {0001} pole figure, and (f) annealed {0001} pole figure..... 55
Fig. 3.19: (a) The thickness (RD-ND) microstructure of AZ31-H24 and (b) the {0001} pole figure. (c) The thickness (RD-ND) microstructure of the commercial AZ31-H24 after 1 hour at 420 oC and (d) the corresponding texture 63
Fig. 3.20 Thickness microstructure of the as-received TRC sheet; (a) edge region exhibiting the columnar grains grown almost normal to the sheet surface, and (b)mid-thickness showing the dendritic structure with equiaxed grains in the middle. 64
Fig. 3.21 Small equiaxed grains in the as-received TRC AZ31 sheet; (a) edge, (b) mid-thickness... 64
Fig. 3.22 Distribution of second phases in the as-received TRC AZ31 sheet; (a) away from the sheet surface and (b) close to the sheet surface 66
Fig. 3.23 SEM micrograph showing the second phase particles and EDS spectrum of the matrix in the as-received TRC AZ31 sheet 67
Fig. 3.24 (a) Centerline segregation in the as-received TRC AZ31 and EPMA micrographs of (b) Al, (c) Zn, and (d) Mn (The region with higher element percentage appears brighter 67
Fig. 3.25 TEM observations on the as–received TRC AZ31 sheet (a) dislocation pile-up around the second phase particles (b) nano-size particles. 68
Fig. 3.26 Pole figure from the as-received TRC AZ31 sheet; (a) surface, (b) mid-thickness..... 68
Fig. 3.27 The Quasi-TRC plate; a) thickness microstructure, b) surface texture (heat transfer axis is parallel to ND in this figure and RD-TD plane is the plate surface)..... 70
Fig. 3.28 EBSD map from the RD-TD plane of the as-received TRC AZ31 sheet.... 70
Fig. 3.29 EBSD map from the RD-ND plane of the as-received TRC AZ31 sheet (close to the edge) 70
Fig. 3.30 EBSD map from the RD-ND plane of the as-received TRC AZ31 sheet (mid-thickness). 71

Fig. 3.31 The thickness microstructure of the TRC AZ31 sheet after 1 hr at 420 ^{o}C; (a) edge and (b) mid-thickness..... 72
Fig. 3.32 TRC AZ31 sheet after 1 hr at 420oC; (a) surface pole figure and (b) EBSD map on the RD-ND plane 73
Fig. 3.33 (a-c) Microstructures and (d-f) corresponding surface texture pole figures of the as-received TRC AZ31 sheet annealed at 420 ^{o}C for 3, 5 and 20 min, respectively 73
Fig. 3.34 (a-c) Microstructures and (d-f) corresponding surface texture pole figures of the as-received TRC AZ31 annealed for one hour at 350 ^{o}C, 375 ^{o}C and 400 ^{o}C, respectively. 74
Fig. 3.35 TRC AZ31 sheet after annealing for 5min at 420 ^{o}C; (a) EBSD map on the RD-ND plane, (b) Magnified area in the white square... 76
Fig. 3.36 (a) Thickness microstructure and (b) surface texture of the TRC sheet rolled at 400 ^{o}C..... 77
Fig. 3.37 (a) Thickness microstructure and (b) surface texture of the TRC sheet rolled and annealed at 400 ^{o}C..... 77
Fig. 3.38 (a) Centerline segregation in the rolled-annealed TRC AZ31 and the EPMA micrographs of (b) Al, (c) Zn, and (d) Mn (the region with higher element percentage appears brighter) 78
Fig. 3.39 map from the RD-ND plane of the rolled-annealed TRC AZ31 sheet (mid-thickness). 79
Fig. 3.40 Tensile flow curves of the as-received TRC AZ31 (RD and TD) and the annealed (one hour at 420 ^{o}C) TRC AZ31 (RDH and TDH). RD and TD are rolling, and transverse directions... 80
Fig. 4.1 As-cast microstructure of M1 (a) edge (b) mid-thickness. (c) SEM micrograph showing the secondary phases in M1 (d) EDS spectrum from the Mg-Mn-Ce-Si particles 90
Fig. 4.2 (As-cast microstructures of ME10 alloys (a) Edge and (b) mid-thickness of ME10(0.05Ce). (c) Edge (d) mid-thickness of ME10(0.1Ce). (e) Edge (f) mid-thickness of ME10(0.2Ce 92

Fig. 4.3 Microstructures of as-cast ME11 alloys (a) Edge and (b) mid-thickness of ME11(0.5Ce). (c) Edge and (d) mid-thickness of ME11(1.0Ce) 93

Fig. 4.4 SEM micrographs showing the second phases: (a) ME11(0.5Ce) at the edge and (b) the EDS spectrum of the Mg-Mn-Ce particles. (c) ME11(0.5Ce) in the mid-thickness and (d) the EDS spectrum of the Mg-Mn-Ce-Si particles..... 94

Fig. 4.5 EBSD maps from the RD-ND plane of the as-rolled at 400 ^{o}C: (a) M1 alloy (b) ME11(0.05Ce) and (c) ME10(0.1Ce) 95

Fig. 4.6 Microstructures of the alloys in the rolled-annealed condition (a) M1, (b) ME10(0.05Ce), (c) ME10(0.1Ce), (d) ME10(0.2Ce), (e) ME11(0.5Ce) and (f) ME11(1.0Ce) 96

Fig. 4.7 Surface texture pole figures of alloys rolled at 400 ^{o}C: (a) M1, (b) ME10(0.05Ce), (c) ME10(0.1Ce), (d) ME10(0.2Ce), (e) ME11(0.5Ce) and (f) ME11(1.0Ce)..... 97

Fig. 4.8 Surface texture pole figures of alloys rolled and annealed at 450 ^{o}C: (a) M1, (b) ME10(0.05Ce), (c) ME10(0.1Ce), (d) ME10(0.2Ce), (e) ME11(0.5Ce) and (f) ME11(1.0Ce)..... 97

Fig. 4.9 Density of basal planes versus deviation angle from sheet normal direction (a) as-rolled (b) annealed 98

Fig. 4.10 (a) As-rolled microstructure of AZ31. EBSD maps from the RD-ND plane of the as rolled at 400 ^{o}C (b) M1 (c) MJ1(0.5Sr)..... 107

Fig. 4.11 Microstructures of the alloys in the rolled-annealed condition (d) AZ31 (e) M1 (f) MJ10(0.2Sr) (g) MJ11(0.5Sr) (h) MJ11(1.0Sr). 108

Fig. 4.12 Surface texture pole figures of alloys, rolled at 400 ^{o}C (a) AZ31 (b) M1 (c) MJ10(0.2Sr) (d) MJ11(0.5Sr) (e) MJ11(1.0Sr), annealed at 450 ^{o}C for 15 min: (f) AZ31 (h) (M1) MJ10(0.2Sr) (j) MJ11(0.5Sr) (k)MJ11(1.0Sr). Density of basal planes versus deviation angle from sheet normal direction (i) as-rolled and (m) annealed 109

Fig. 4.13 The MJ11(0.5Sr) after annealing for 4 min at 450 °C: (a) EBSD map on the RD–TD plane and (b) magnified area in the white square c) misorientation gradient along the CD direction shown in Fig4.13b d) texture pole figure

of grain A and B e) texture pole figure of fine grain close to stringer..... 111
Fig. 4.14 As-cast microstructure of (a) AZ31 (b) Z1 (c) ZJ10(0.1Sr) (d) ZJ10(0.3Sr) (e) ZJ11(0.5Sr) (f) ZJ11 (1.0Sr)..... 118
Fig. 4.15 SEM micrograph showing second phase particles (a) Z1 (b) ZJ11(0.5Sr) 119
Fig. 4.16 Microstructures of the alloys in the rolled condition (a) AZ31, (b) Z1 (c) ZJ10(0.1Sr), (d) ZJ10(0.3Sr), (e) ZJ11(0.5Sr) and (f) ZJ11(1.0Sr)..... 120
Fig. 4.17 Microstructures of the alloys in the rolled-annealed condition (a) AZ31, (b) Z1(c) ZJ10(0.1Sr), (d) ZJ10(0.3Sr), (e) ZJ11(0.5Sr) and (f) ZJ11(1.0Sr)... 121
Fig. 4.18 Surface texture pole figures of alloys rolled at 400 ^{o}C: (a) AZ31, (b) Z1 (c) ZJ10(0.1Sr), (d) ZJ10(0.3Sr), (e) ZJ11(0.5Sr) and (f) ZJ11(1.0Sr). ... 123
Fig. 4.19 twins in annealed a) Z1 b) ZJ11(1.0Sr). 123
Fig. 4.20 Density of basal planes versus deviation angle from sheet normal direction in as-rolled condition. 125
Fig. 4.21 Surface texture pole figures of alloys rolled and annealed at 400 ^{o}C for 5 min: (a) AZ31, (b) Z1 (c) ZJ10(0.1Sr), (d) ZJ10(0.3Sr), (e) ZJ11(0.5Sr) and (f) ZJ11(1.0Sr)..... 126
Fig. 4.22 The ZJ11(1.0Sr) after annealing for 3 min at 400 °C: (a) EBSD map on the RD–TD plane and (b) magnified area in the white square c) texture pole figure of grain A d) texture pole figure of fine grain close to stringer... .. 129

LIST OF TABLES

Table 2.1 Slip Systems in Magnesium [8] 7
Table 2.2 Mechanical Properties of AZ31 Sheet Produced by TRC/Coil Rolling Process in Comparison with Commercial Products Produced by DC Casting/ Warm Rolling Process [50, 61] 27
Table 3.1 Comparison of AZ31 solidified in sand cup and copper mould... 46
Table 3.2 Tensile Properties of TRC AZ31 in Rolling and Transverse Directions (RD, TD) 80
Table 3.3 The Microstructure and Texture of AZ31 in Various Conditions 82
Table 4.1 Alloy Compositions 88
Table 4.2 Grain Size of M1 and ME Alloys 93
Table 4.3 Composition of alloys used in this study 105
Table 4.4 Chemical Composition of the Alloys..... 116
Table 4.5 Second phases in Mg sheet alloys studied in this work [4-7]..... 134
Table 4.6 Crystal structure and parameters of second phase particles in this study [4, 8] 135

CHAPTER 1

INTRODUCTION

Magnesium (Mg) is the lightest structural metal with a density of 1.74 g cm^{-3}; 35% lighter than aluminum (Al) and over 400% lighter than iron [1]. The automotive industry has long-term objectives to decrease vehicle weight for the improvement of fuel consumption and reduction of emissions; this goal must be balanced with cost targets and reliability. To date, the use of Mg in cars has been limited to die cast parts, such as steering column upper brackets, steering wheel cores, engine head covers, disk wheels, brake pedal brackets, meter panel housings, seat frames, air bag plates, oil pans, instrument panel reinforcements, transmission cases and engine blocks [2, 3]. The application of Mg in automotive body construction has great potential for further weight reduction [4]. In general, the automotive body largely consists of sheet metal parts and comprises almost 25% of vehicle weight. In the past, Al has been the first choice for vehicle weight reduction [5, 6]. To replace Al sheet with Mg sheet in automotive, recently the interest in low cost Mg sheet has significantly increased [4].

AZ31 (Mg-3wt.%Al-1wt.%Zn), the most common Mg sheet alloy, is currently produced by hot rolling of the DC cast ingot. The hot-rolled sheet, designated as AZ31-H24, exhibits a non-uniform grain size [7, 8], while sheet rolled at lower temperatures is prone to extensive twining. Rolling orients the {0001} basal planes of the hexagonal closed packed (HCP) Mg crystals parallel to the sheet surface [7-9], leading to preferred orientation known as basal texture. Hot rolling produces a perfect basal texture, while the warm-rolled sheet exhibits an egg-shaped distribution of {0001} planes in the pole figure [7-9]. The presence of basal texture adversely affects formability and as a consequence considerably limits the variety of components which can be manufactured from Mg sheet. The possibility to enhance the formability of magnesium alloys by modifying the texture

has been verified [10]. Considerable effort is currently being conducted to weaken the basal texture or attain random texture in rolled magnesium sheet [11-13].

Due to several heating and rolling processes, Mg sheet production by conventional processes is relatively expensive [4]. If the cost of Mg sheet production were reduced, the demand for Mg sheet would increase significantly [14]. In order to lower Mg sheet production costs, near-net shape sheet casting processes including thin slab casting, single-belt casting and twin-roll casting (TRC) have been developed (Fig. 1.1) [15]. Among the near-net shape casting processes, TRC produces the thinnest as-cast sheet with thicknesses less than 6 mm [16]. The investment and operation costs of TRC are 1/3 to 1/4 of the conventional Mg sheet production processes [17-19]. Therefore TRC is considered to be the most promising candidate for low-cost production of Mg sheet [18].

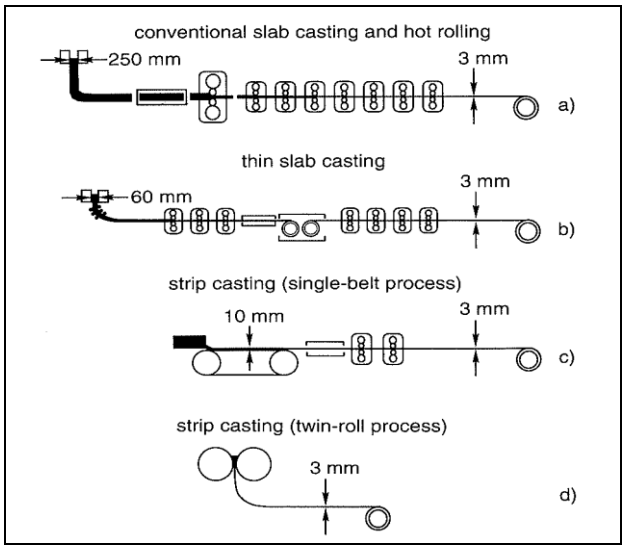

Fig. 1.1 Process routes for hot strip production [15].

Despite industrial interest in TRC AZ31, which is available on a limited scale globally, very little information exists on its microstructure and texture. TRC that combines casting and *in situ* warm rolling produces a unique combination of cast and deformed structure. The structure of TRC AZ31 sheet consists of a chilled-zone close to the sheet surface, followed by columnar-grains formed as a result of directional

solidification [4, 14]. Equiaxed grains observed in the central region of the TRC sheet can be attributed to constitutional undercooling. Kawala *et al.* [20] have reported a texture gradient from the central region to the near-surface layers of the TRC sheet. Since strain is accumulated in the columnar grains during the *in situ* rolling of the TRC process, Park *et al.* [21, 22] have observed that subsequent annealing transforms the large columnar grains into fine equiaxed grains. Fine equiaxed grains with an average size of 6 μm are produced via TRC followed by warm rolling and annealing [4, 22]. TRC may reduce the cost of sheet production, but does not solve the intrinsic formability problems of Mg due to its HCP crystal structure.

The long-term objective of this study was to develop Mg Sheet alloys for twin-roll casting with acceptable moderate temperature formability. Furthermore, although the principal effects of rare earth (RE) elements on the texture development during rolling and following annealing is well established, the mechanisms responsible for these alterations in texture are still under investigation. Therefore secondary objectives were:

1) To understand the microstructure and texture of TRC AZ31 (as-received and themomechanically processed), to investigate the effects of annealing on the texture of rolled sheet and to determine the underlying mechanisms in texture development.
2) To develop new alloys with weakened texture that can lead to improved formability, and to understand the mechanisms in texture evolution in these new alloys and determine the general trends in texture development in Mg alloys.

This work contains six chapters. Chapter 1 provides a general background of magnesium sheet production. Chapter 2 presents a literature review which focuses on TRC of Mg, its metallurgical aspects and Mg formability. Chapter 3 reports results of experiments conducted on TRC AZ31 alloy and more significantly on a pre-roll annealing treatment that weakens the post TRC rolling texture, which is related to the metastable microstructure of the TRC AZ31. Chapter 4 reports new alloys developed via the additions of Ce or Sr to Mg-Mn and Mg-Zn base alloys, which lead to texture weakening. Finally, Chapters 5 and 6 present the major conclusions and the contribution

to original knowledge of this work, respectively.

References

1. M. M. Avedesian, H. Baker, Magnesium and Magnesium Alloys 1999: ASM International, Materials Park, OH 44073-0002, USA, . pp. 314.
2. T. Kaneko, M. Suzuki, , Mater. Sci. Forum, 2003, 419-422, pp. 67-72.
3. B. Engl, , Light Metal Age, 2005. 63(5), pp.14-19.
4. I.-H. Jung, W. Bang, I. J. Kim, , H. I.Sung, , W. J.Park,; D. Choo, , S. Ahn, , in: R. S. Beals (Ed.) Magnesium Technology. 2007 TMS Orlando, FL, USA pp. 85-88.
5. E. J. Vinarcik, Light Metal Age., 2004. 62(3-4): pp. 56-57.
6. E. Doege, K. Droder, J. Mater. Process. Technol., 2001. 115: pp. 14–19
7. F. Kaiser, J. Bohlen, D. Letzig, K.-U. Kainer, A. Syczynski, C. Hartig, Adv. Eng. Mater., 2003. 5(12): pp. 891-896.
8. A. Jager, P. Lukac, V. Gartnerova, J. Haloda, M. Dopita, Mater. Sci. and Eng. A 2006. 432: pp. 20–25.
9. M. R. Barnett, M. D. Navea, C. J. Bettlesb, Mater. Sci. Eng. A 2004. 386: pp. 205–211.
10. E. Yukutake, J. Kaneko M. Sugamata, Mater. Trans., 2003. 44(4) pp. 452-457.
11. L.W.F. Mackenzie, M. Pekguleryuz, Mater. Sci. Eng. A, 2008. 480(1-2): pp. 189-197.
12. L.W.F. Mackenzie, M. O. Pekguleryuz, Scr. Mater., 2008. 59(6): pp. 665-668.
13. J. Bohlen, M. R. Nürnberg, J. W. Senn, D. Letzig, S. R. Agnew, Acta Mater., 2007. 55(6): pp. 2101-2112.
14. Y. Nakaura, A. Watanabe, K. Ohori, Mater. Trans., 2006. 47(7): pp. 1743-1749.
15. K. Schwerdtefeger, ISIJ International, 1998. 38 (8), pp. 852-861.
16. C. Yang, P. Ding, D. Zhang, , F. Pan, Mater. Sci. Forum. 2005. pp. 427-430.
17. D. R. Herling, J. A. Carpenter, P. S. Sklad, in FY2005 Progress Report for Automotive Lightweighting Materials. 2005, US department of Energy.
18. H. Watari, T. Haga, , N. Koga, , K. Davey, , J. Mater. Process. Technol., 2007. 192-193: pp. 300-305.

19. D. Liang, C. B. Cowley, JOM, 2004. 56(5): pp. 26-28.
20. R. Kawalla, M. Oswald, C. Schmidt, M. Ullmann, H.-P. Vogt, N. D. Cuong, (Ed.), Magnesium Technology,TMS 2008, USA, pp. 177-182.
21. S. S. Park, G. T. Bae, D. H. Kang, I. H.Jung, K. S. Shin, N. J. Kim, Scr. Mater., 2007. 57(9): pp. 793-796.
22. S. S. Park, J. G.Lee, H. C. Lee, N. J. Kim, , in A.A. Luo (Ed.) Magnesium Technology 2004 TMS, USA, pp. 107-112.

CHAPTER 2

LITERATURE REVIEW

The Automotive Industry has a long-term goal of vehicle weight reduction for improved fuel economy, enhanced performance and reduced emissions. This goal must be balanced with cost targets and reliability. To achieve this goal, car companies are identifying lightweight materials and related processes which will cost-effectively enable weight reductions without sacrificing strength and functionality. The focus of this literature review is two-fold:

1. The deformation characteristics of Mg, formability, rolling texture, and the effects of alloying elements are reviewed in sections 2.1 to 2.4.
2. Twin-roll casting of magnesium is reviewed in section 2.5.

2.1 Deformation Characteristics of Magnesium

Deformation of hexagonal-close-packed (HCP) Mg is primarily characterized by (i) basal slip at room temperature and (ii) non-basal (pyramidal, prismatic) slip at temperatures above 200-250 ^{o}C depending on alloy composition. Twinning is also seen both at room temperature and to a lesser extent at elevated temperatures [1].

2.1.1 Slip

It is generally known that cubic metals with body-centered and face-centered cubic structures (BCC & FCC) are more formable than HCP metals such as magnesium, since they can provide at least five independent slip systems required by von Mises criterion for homogenous plastic deformation to maintain integrity of the grain boundary [2]. HCP Mg only has two independent slip systems at room temperature, therefore to improve formability additional slip systems must be activated. At high temperatures the

formability of Mg improves significantly due to activation of prismatic and pyramidal slip planes [3]. The slip planes and the total number of slip systems in Mg are shown in Fig 2.1 and Table 2.1. Except for the 2nd order pyramidal slip, Burgers vectors for all of the slip systems, is <11-20>) or <a>.

Critical resolved shear stresses (CRSS) determine the ease of glide on each slip system. The effect of temperature on the CRSS of single crystal Mg, for each slip system, is illustrated in Fig. 2.2 [4]. At temperatures in excess of 230 ^{o}C, the differences in the CRSS of basal slip and non-basal slip systems drop to twice from 10× at room temperature. This is due to the change in lattice parameters from thermal contraction and electron overlap [5]. The CRSS is expected to depend on solid solution alloying since this affects electron overlap and lattice spacing (Fig. 2.3). Due to the activation of non-basal slips, cross-slip becomes possible, leading to improved ductility and formability at the expense of mechanical strength [6, 7].

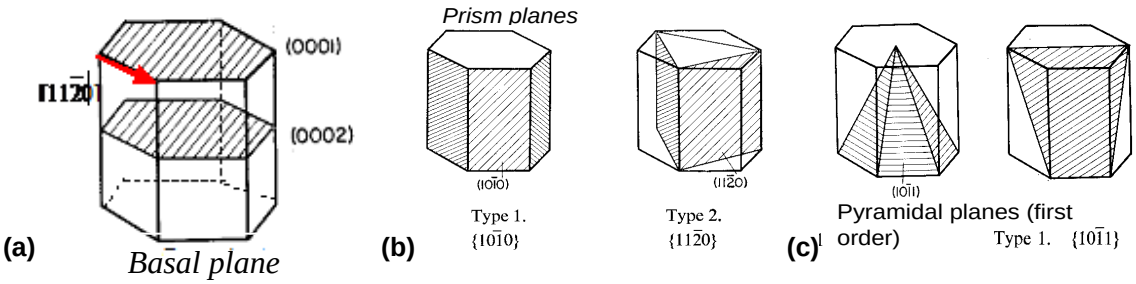

Fig. 2.1 Slip and twinning planes in HCP magnesium [3].

Table 2.1 Slip Systems in Magnesium [7].

Slip System	Direction	Slip plane and direction	Independent slip systems
Basal	*a*	{0001}<11-20>	2
Prismatic	*a*	{10-10}<11-20>	2
Pyramidal type I	*a*	{10-11}<11-20>	4
Pyramidal type II	*c+a*	{11-22}<11-23}	5

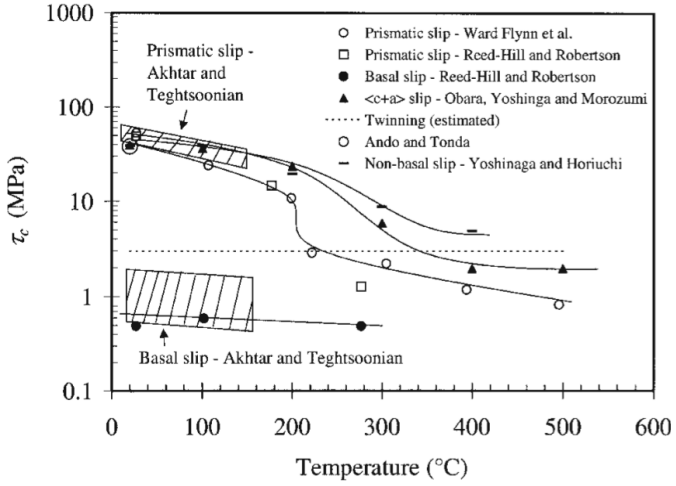

Fig. 2.2 The effect of deformation temperature on the CRSS value of slip systems and twinning in pure Mg [4].

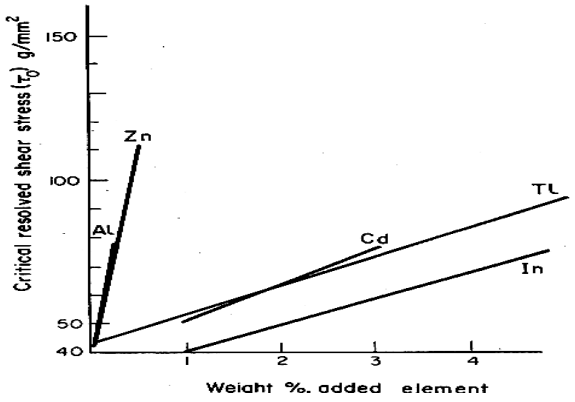

Fig. 2.3 Effect of alloying on CRSS for basal slip in Mg [3].

2.1.2 Twinning

Due to low CRSS of twining, which is comparable close to CRSS of basal slip, twinning is a predominant deformation mechanism in Mg both at room and elevated temperatures. Twinning occurs on a number of planes, the most common being $\{10\bar{1}2\}$ (Fig. 2.4); however, $\{10\bar{1}1\}$ can also be frequently observed [3].

Twinning is favoured by compression parallel to the basal plane and tension parallel to the c-axis in the case of Mg (Since <*a*> slip direction is perpendicular to the *c*-axis). In Mg, the $\{10\bar{1}2\}$ twins are referred to as "tension" twins as they are preferred

when tension is applied along the *c*-axis [3, 7]. On the other hand, $\{10\bar{1}1\}$ and $\{10\bar{1}3\}$ twins are referred to as "compression" twins $\{10\bar{1}1\}$ twins, as they are allowed for compression along the *c*-axis [7].

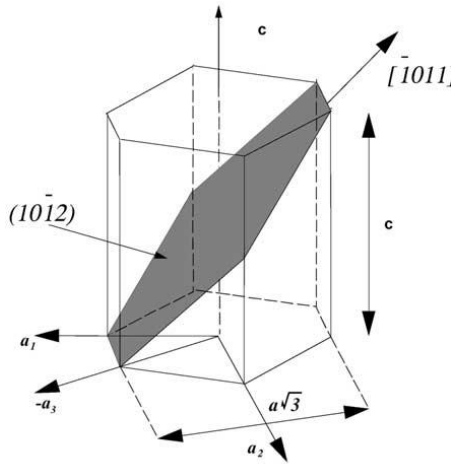

Fig. 2.4 *The* $\{10\bar{1}2\}$ *tensile twinning system for magnesium.*

Twinning rotates the basal planes to a different orientation, which can be favourable or unfavourable [7, 8] for further slip. $\{10\bar{1}2\}$ twinning rotates the crystal by 86^o where basal planes that were unfavourable, stay unfavourable. The $\{10\bar{1}1\}$ and $\{10\bar{1}3\}$ twins rotate the basal planes by 56^o and 64^o, which make the initial basal planes that were unfavourably oriented for slip to a favourable orientation.

Mg also exhibits double twinning through formation of $\{10\bar{1}2\}$ extension twins within the $\{10\bar{1}1\}$ contraction twins (Fig 2.5) [7, 9]. As a result of this double twinning, unfavourably oriented basal planes reorient to a nearly favourable orientation (38° and 22° reorientation after $\{10\bar{1}1\}$–$\{10\bar{1}2\}$ and $\{10\bar{1}3\}$–$\{10\bar{1}2\}$ double twinning, respectively).

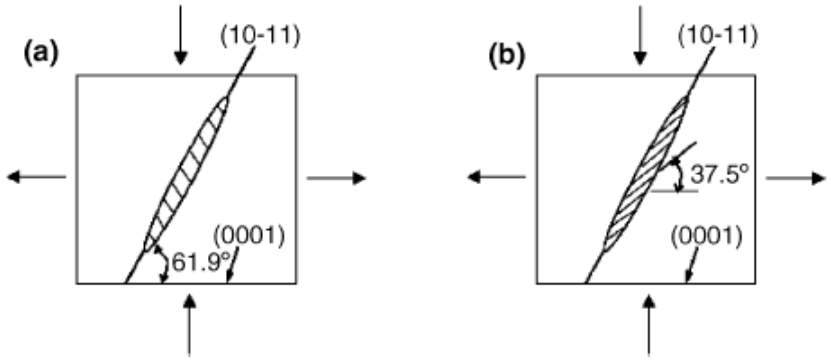

Fig. 2.5 Schematic diagram showing double twinning process: (a) $\{10\bar{1}1\}$ Twinning reorients the basal plane by 61.9^o (b) followed by retwinning on $\{10\bar{1}2\}$ [16].

2.2 Magnesium Rolling Texture

Rolling orients the {0001} basal planes of the HCP Mg crystals parallel to the sheet surface with the $[10\bar{1}0]$ axis in the rolling direction [10-14], leading to a preferred orientation known as the basal texture. This phenomenon is related to the low critical resolved shear stress (CRSS) of basal slip in Mg. When the *c*-axis of a grain is parallel to the compression axis, the resolved shear stress on this basal slip system is almost zero. So the accumulation of basal <*a*> dislocations (which is necessary for recrystallization) in this grain is less when compared to the grains with other orientations, where the basal slip system receives a finite amount of resolved shear stress. Therefore, the grains with *c*-axes parallel to the compression axis (which are most of the grains in the sheet with basal texture) are stable, and therefore nucleation and growth is retarded. Since there is no new grain formation, the basal texture is maintained [15]. On the other hand, grains with other orientations are easily consumed by repeated dynamic recrystallization. As the deformation proceeds, more and more grains with their *c*-axes parallel to the compressive stress direction take up a basal orientation and the basal texture is gradually reinforced [15].

Hot rolling produces a perfect basal texture, while the warm-rolled sheet exhibits an egg-shaped distribution of {0001} planes in the X-ray pole figure (Fig. 2.6) [10-14]. The formation of two-pole basal texture during rolling has been related to different phenomena [5, 17, and 18]. Texture simulation has attributed the formation of an egg

shaped distribution to the activation of <*c*+*a*> slip [17], while other investigators have argued that it is due to the formation of $\{10\bar{1}1\}$ compression twinning followed by $\{10\bar{1}2\}$ re-twinning [18]. Additionally it has been hypothesized that on the sheet surface, basal normals are perpendicular to the rolling plane yielding a single texture, but that they may deviate up to 15^{o} as one moves deeper into the sheet, resulting in double textures [5].

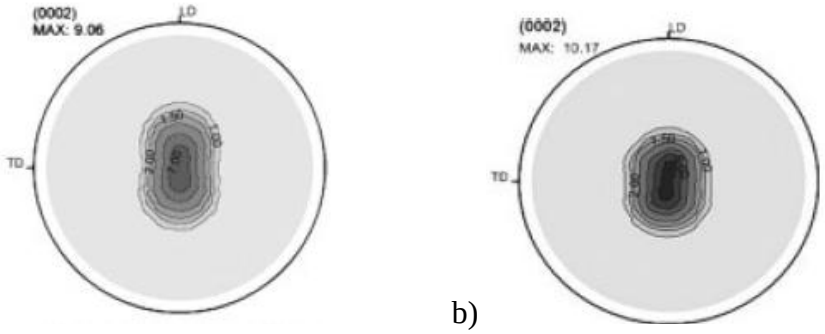

a) b)

*Fig. 2.6 {*0002*} Pole figures in AZ31 after hot rolling of cast material a) 250 ^{o}C) b) 400 ^{o}C [11].*

2.3 Formability of Magnesium Alloys

Formability is characterized by a number of parameters such as the number of independent active slip systems, total elongation, work-hardening exponent *n*, strain-rate sensitivity *m*, *r*-values, the related texture, maximum bending radius and spring-back. Depending on the type of forming operation, one or two of these parameters become more important. In stretch forming, total elongation, and to some extent the work-hardening exponent, *n*, are important. The *n*-value is the work-hardening exponent (slope of the plastic portion of true stress –true strain curve) and a measure of the deformation level (Fig. 2.7). It correlates the ability of the material to be stretch-formed to avoid necking and tearing. High n means the metal strengthens while deforming and hence exhibits uniform deformation during stretching. To assess the performance in deep-drawing, press forming and stamping, plastic strain ratio (ratio of true strain in width to true strain in thickness) and anisotropy of the sheet material are important. Plastic strain ratio is a measure of the resistance to thinning during deep drawing. The two plastic

strain ratio parameters, normal anisotropy (*r*-value or r_m) and the planar anisotropy Δr, characterize the ability for deep drawing. For good deep drawability, a high *r*-value (above 0.6) is desirable (Al =0.75, steel=1.6). A small Δr is needed to minimize ear formation.

The room temperature formability of Mg is poor, however at 230-400 ^{o}C formability greatly improves and, in fact, has several advantages over cold-forming of other metals [19]. These are: low spring back, larger deformation in single operation, less power and versatile die materials. The *n* value for AZ31-H24 has been determined to be 0.12 [20] (compared to *n* =0.16-0.25 for steel and Al). A high *n* value is also desirable for good stretch forming. On the other hand, total elongation is useful in comparing stretchability; in general, the greater the total elongation the greater the stretch formability. Mg AZ31-H24 Mg sheet exhibits a total elongation of 20% (compared to 40% of steel); this increases to 60% at 250 ^{o}C [20].

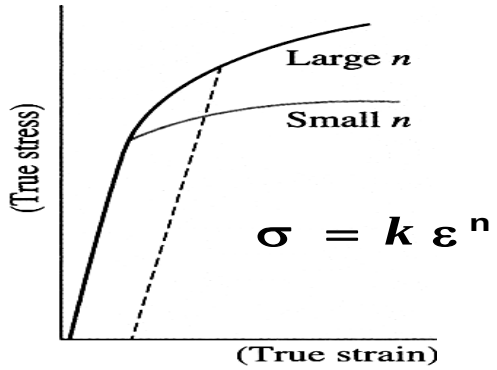

Figure 2.7 True stress-strain curve for low and high n-values values [21].

As explained earlier, the texture also needs to be engineered (balanced via thermo-mechanical processing) to attain uniform deformation. Kaiser *et al.* [11] have shown that the difference in transverse *vs.* longitudinal yield stress is 50 MPa in rolled AZ31 sheet. The tensile elongation of AZ31 is relatively constant over the 150-225 ^{o}C temperature range [3]. For AZ31, the difference in Lankford coefficients (*r*-value) was found to be large: *r* = 1.0 in the rolling direction and *r* = 3.5 in the transverse direction.

This anisotropy was minimized in fine-grained sheets due to the contribution of grain boundaries to strength.

2.4 Effect of Alloying Elements on Formability of Magnesium

Attempts to improve the formability of Mg sheet have been motivated by the interest of using Mg sheet for automotive applications. In the following sections, the effect of alloying elements on 1) grain refining and 2) texture weakening will be discussed since these two factors have a significant influence on formability.

2.4.1 Grain refining

It is well known that as the grain size decreases, deformation becomes more homogeneous and formability improves [2]. Alloying elements can be used to refine the initial (cast) grain size and to maintain fine grains throughout further forming operations. Mg alloys which are free of Al are effectively grain-refined by Zr [1]. During solidification, Zr-rich solid particles form in the early stage of melt freezing, which provide sites for heterogeneous nucleation of Mg grains [1]. Certain experimental alloys indicate that Zr also produces fine grained material in Al containing alloys [22]. Al-containing alloys, more commonly, require carbon inoculation (via hexachloroethane) or Ca and Sr trace additions to refine their grain size [1]. Ca at 0.15% has been used to improve the rolling properties of AZ31 alloy, possibly due to grain refining and the refinement of the $Mg_{17}Al_{12}$ phase [3]. Sr at 0.2% has been used in the AZ80 forging alloy to refine grain size and improve the forgeability of the alloy [23]. Sr is one of the most effective alloying elements, since it acts as a growth-poisoner and also prevents abnormal grain growth [24].

Usually alloying elements with a high growth restriction factor, Q, lead to grain refinement [25]. Grain size, d, is related to Q which in turn is related to phase diagram parameters through:

$$d=a+(b/Q)$$

where a, b = constants; $Q = m_L C_o (k-1)$; m_L= slope of the liquidus line; C_o= alloy solute concentration k= partition coefficient = C_S/C_L; C_S= solute concentration in the solid; C_L=

solute concentration in the liquid. Certain elements such as Zn have high Q factor leading to grain refining [25].

These conventional methods only give a limited amount of grain refinement, from 1000 μm to approximately 250 - 100 μm, and not the 5-10 μm sizes required for substantially improved formability. Therefore, the application of thermomechanical processing has been introduced to further reduce the grain size of Mg alloys [26, 27]. Yamashita *et al.* applied an equal-channel-angular extrusion (ECAE) technique to reduce the grain size from 400 to 17 μm [26]. It has been shown that in coarse-grain Al, the strain near to grain boundaries is different from the strain at the center of the grain. Deformation is more homogeneous as the grain size decreases and strain increases. This is due to activation of slips on non-close-packed planes in regions in the vicinity of grain boundaries [2]. Enhanced grain boundary sliding and non-basal slip has been reported in Mg that has very fine grains [6].

2.4.2 Texture Weakening

The presence of basal texture in Mg adversely affects the formability and, as a consequence, considerably limits the variety of components which can be manufactured from Mg sheet. The possibility of enhancing the formability of magnesium alloys by weakening the texture has been shown [28-30]. Here, rolled specimens with lower texture intensity in the (0002) plane exhibited enhanced stretch formability [29]. Another investigation revealed that the *r*-value (Lankford coefficient), deep drawing and stretch forming of AZ31 alloy is strongly affected by texture variation [28]. It was reported that the Erichsen value at room temperature improves significantly as the basal texture intensity reduces [30]. In comparison to conventional Mg alloys (containing Al and/or Zn), it was shown that Mg alloys containing rare-earth (RE) elements exhibit higher *r*-values, which was attributed to weaker textures [31]. It was reported that the addition of Ce to Mg improves its elongation, rollability and stretch formability [12, 32]. Due to weaker texture, the alloys containing yttrium (Y) show improved stretch formability [33]. It has also been shown that texture randomization results in stretch formability

improvement of TRC Mg alloys at room temperature [34]. A weaker basal texture means that a larger volume fraction of grains are oriented favourably to accommodate the deformation by basal slip and twinning, which promotes sheet thinning [31]. Therefore considerable effort is currently being conducted to weaken the basal texture or attain random textures in rolled magnesium sheet by modifying existing alloys, developing new alloys and uncovering the mechanisms responsible for texture weakening [11, 17, 31, 35-38].

i) The Mechanism of Texture Weakening in Mg Alloys

Texture weakening (randomization) is usually attributed to recrystallization phenomena known as particle-stimulated nucleation (PSN) where sub-grains formed at the particle-matrix interfaces coalesce to form new grains with orientations different from the parent grains [39-41]. It is well known that gliding dislocations do not shear non-coherent precipitates. As a result, dislocation pile-up or looping at the particle-matrix interface occurs. The polarity of the tension-compression strain fields of these dislocations leads to the local bending of the crystal at the precipitate-matrix interface. The local strain (and bending) is relieved via the formation of cell and sub-grain formation upon annealing. Sub-grains that form during the recovery stage coalesce through rotation according to the five-degrees of freedom of low-angle boundaries (tilt, twist, rotation) and nucleate into grains with substantially different orientations than the parent grain, leading to texture weakening [42]. This recrystallization mechanism is different from the grain-boundary bulging mechanism which results in new grain orientations closely associated with those of the parent grains. PSN has been attributed as the texture weakening mechanism for Mg alloys by several researchers [39, 40].

Alloying can also alter the lattice parameters and the axial ratio (*c/a*) of Mg. the effect of The Li, In and/or Zn on the lattice parameters of Mg alloys have been determined via X-ray diffraction (XRD) by Becerra *et al.* [43]. Li decreased the axial ratio (*c/a*) of magnesium from 1.6424 to 1.6068 within 0-16at%Li. In increased *c/a* of Mg to 1.6261 as In increased towards 3.3at% while Zn showed no effect on *c/a* in the

0.2-0.7at% range. It has also been observed that a large decrease in *a* results when In >0.2at% and when Zn >0.2at% [43].

In HCP metals, the *c/a* ratio affects the difference in the critical resolved shear stress between basal slip and non-basal slip. The reduction of *c/a* can enhance the activity of the non-basal slips [5]. The *c/a* ratio of 1.624, as in Mg, results in low critical resolved shear stresses on the basal plane, favouring basal slip. Ti on the other hand, with a much lower *c/a* ratio (1.58) than Mg, has a high basal CRSS but low prismatic CRSS [5]. Li has received much interest as an alloying addition to Mg due to its extensive effects on lattice parameters, ductility and formability of Mg. Due to its size factor, Li has a high solid solubility in Mg [1]. 11wt.% Li changes the HCP to a Mg-Li solid solution with a BCC crystal structure, thereby improving the formability of wrought products [1]. Li in the solid solution reduces the *c/a* ratio in the α-Mg phase from 1.624 to 1.61 and reduces the corresponding CRSS of the prismatic slip and the strain-hardening rate [5], so that more slip systems can be activated at lower temperatures. Other alloying elements that can change the lattice parameters also exist, for example Au, Mn, Rh and Zr decrease *a*-spacing, Au, Ce and Pd decrease *c/a* while Ba, Ir, Pt, Rh, Ti and Zr increase *c/a* ratio [5].

The stacking fault energy is another factor which could effect texture development during deformation [41, 44]. Alloying elements could change the stacking fault energy of Mg [45, 46]]. Texture modeling and TEM studies suggested that Li and Y increase the glide of <*c* + *a*> dislocations on pyramidal planes in HCP α-Mg, where the role of Li and Y was attributed to the stability of partial dislocations of <*c* + *a*> [17].

ii) Effect of Alloying Element on Texture of Mg Sheet alloys

Although the principal effect of RE elements on texture development during rolling and subsequent annealing is well established, the mechanisms responsible for texture alteration are still under investigation. Bohlen *et al.* [31] studied the effect of RE elements on the texture of Zn based alloys with 1 wt% and 4 wt% of Zn. ZM21 (Mg-2wt.%Zn-1wt.%Mn) and ZK10 (Mg-1.5wt.%Zn-0.4wt.%Zr) alloys were also investigated as benchmarks. ZM21 and ZK10 showed the strongest basal texture, with 8 multiples of a random distribution (MRD) while other alloys containing RE show weaker

basal texture (about 4 MRD) [31]. The authors could not relate the texture weakening to a higher amount of second phases in Mg alloys containing RE, as the same amount of intermetallic phases (but different intermetallic types) were observed in ZM21 and ZK10. It was hypothesized that soluble Zn and RE additions were responsible for the modification of rolling texture [31].

Mackenzie and Pekguleryuz [35] reported that an increase of Li from 1wt.% to 3wt.%, broadened the basal contour both in the rolling direction (RD) and transverse direction (TD). The same authors also investigated the effect of Ce on the texture of Mg-Zn alloys [36]. The deformation texture of Mg-Zn alloys was similar to that of conventional Mg alloys. However, the addition of a small amount of cerium weakened the texture significantly. Additionally it was reported that basal textures were broadened more towards TD and the (0002) peaks were ~45^{o} away from the sheet normal direction (ND) [36]. The authors also observed further basal texture weakening after subsequent annealing. The authors concluded that a form of "solute drag" might be responsible for texture weakening, since no evidence of PSN was found [36].

Barnett *et al.* [12] and Chino *et al.* [32] studied the effect of Ce addition on rolled Mg. Barnett *et al.* [12] related texture weakening to an increase of shear band density which was associated to the material within a shear band inclined from the basal pole. However, Chino *et al.* [32] related texture weakening to stacking fault energy alteration, as they observed the activation of prismatic <*a*> slip in Mg-Ce alloy.

Chino *et al.* [33] also studied the effect of Y (up to 1.2wt.%) on the texture of a Mg-Zn alloy. The basal texture was weakened and modified as characterized by the splitting of basal poles toward the TD and RD; this effect was hypothetically attributed to the activation of prismatic <*a*> slips [33].

Stanford [38] reported a texture weakening effect of Gd additions of up to ~1wt.%, however higher Gd concentrations did not exert any further effect on texture. In this case, the texture weakening was attributed to an increase in shear band density. Recently, Hantzsche *et al.* [37] studied the effect of RE (Ce, Nd) and Y on the texture of rolled Mg. They related weakened texture to the solubility level of these elements in Mg [37]. The

texture weakening was attributed to the appearance of deformation bands and to the restriction of grain growth [37].

2.5 Mg Sheet Alloys

2.5.1 Mg-Al-Based Alloys

This group contains the medium strength AZ31 (Mg-3wt.%Al-1wt.%Zn) alloy which is the most common commercial Mg sheet alloy. The addition of Al to Mg alloys improves strength and hardness [1]. Zn is often used in combination with Al to improve the room temperature strength, however in Mg alloys containing 7 to 10 wt% Al, it promotes hot shortness when added in excess of 1 wt% [1]. AZ31 is the most highly alloyed composition which is still reasonably free from stress corrosion cracking, though welded structures made of AZ31 require stress relieving [3]. AZ61 is another sheet alloy in this group which has higher tensile properties than that of AZ31 [3].

2.5.2 Mg-Mn Based Alloys

Mg-Mn alloys have been used as sheet materials due to good rolling behaviour, weldability and corrosion resistance combined with medium strength [3]. This alloy usually has a coarse grain structure and contains insoluble Mn particles [3]. Mg-Mn sheet alloys, designated as M1 and M2, were developed with a relatively high manganese content (1 - 2 wt%) [5, 47]. In these alloys, a peritectic reaction leads to the formation of a Mg solid solution (α-Mg) and α-Mn.

2.5.3 Mg-Zn-Based Alloys

The strength of Mg alloys (both cast and wrought alloys) can be improved with the addition of Zn [1]. Zr and RE elements can also be added to these alloys. The Mg-Zn alloys have improved mechanical properties by age hardening [1]. Zinc also counteracts the detrimental corrosive effect of Fe and Ni impurities [1]. Casting alloys are prone to shrinkage microporosity; however this is not an important problem in wrought alloys [1].

The ternary Mg-Zn-Mn alloy, ZM21, was developed by Magnesium Electron Ltd (UK) as a sheet alloy. ZM21 has good tensile properties (equal to that of AZ31), and is claimed to roll easily and without edge cracking [3]. This alloy has been used in the past in aircraft applications but is not currently produced as a commercial Mg sheet alloy [31]. Another alloy system, ZK (Mg-Zn-Zr), includes ZK3 (Mg-3%Zn-0.6%Zr) and ZK1 (Mg-1.5%Zn-0.6%Zr). ZK3 has high strength but limited weldability; ZK1 has very good weldability but lower tensile properties [3]. These alloys roll easily, are resistant to grain growth and lose room temperature strength upon hot working or annealing [3]. The ZE10 (Mg-1%Zn-0.25%RE) has lower strength than AZ31 but has the best toughness of any Mg sheet alloy. This alloy is also weldable and does not need stress relief after welding [3].

2.5.4 Mg-Li-Based Alloys

Several ultra-light Mg alloys have been developed that contain Li along with Al, Zn or Si [1]. Alloys such as LA141A (Mg-14wt.%Li-1wt.%Al) and LS141A (Mg-14wt.%Li-1wt.%Si) have been well developed but are rarely used [1]. Li changes the crystal structure of Mg from HCP to BCC and significantly improves formability. As these alloys are very light and have high specific stiffness, they are very attractive for aerospace applications [1].

2.6 Magnesium Sheet Production

2.6.1 Conventional Magnesium Sheet Production

In conventional sheet production, Mg alloys are direct-chill cast in the form of slabs up to 1800 mm long, 1000 mm wide and up to 300 mm in thickness [48, 49]. The slabs are homogenized for 2 hours at 400-500 ^{o}C and to achieve a clean and smooth surface, the slabs are scalped to a depth of about 3 mm [49, 50]. About 10 - 20% thickness reduction is achieved in rolling each step. Rough hot rolling, with a final product thickness of 5 mm, is carried out at temperature range of 400-460 ^{o}C; this process can comprise of approximately 25 passes of 20% thickness reduction each. Due to the low heat capacity of Mg alloys, reheating is required between passes which causes a reduction in

productivity and an increase in the Mg sheet price [49, 50]. However, due to numerous heating and rolling steps, some of the casting defects can be eliminated and consequently a high-quality sheet can be produced [51].

After rough hot rolling, intermediate hot rolling is executed at 340-430 ^{o}C to reduce the strip thickness to ~ 1 mm. A thickness reduction of about 10% is achieved in each step with up to approximately 10 passes. To keep the temperature of the slab above 340 ^{o}C, reheating is performed after each pass [49, 50]. The intermediate hot rolling is followed by finish rolling to achieve a final thickness of ~0.5 mm, by either warm rolling (190-400 ^{o}C) or cold rolling. Again, heating between each pass is necessary due to rapid cooling of the thin sheet [49, 50].

Different annealing processes can be performed on the Mg alloy sheet to adjust the final mechanical properties. By heating at about 370 ^{o}C for one hour, a soft (O) temper can be obtained; and heating one hour at 260 ^{o}C gives an H24 temper [49, 50]. The production of Mg alloy sheet via conventional sheet production is relatively time and energy consuming. As a result, the cost of Mg sheet production is high, compared to that for Al sheet [49, 50].

2.6.2 Twin-Roll Casting (TRC)

The concept of twin-roll casting was introduced for the first time by Henry Bessemer in the middle of the 19th century [52]. Bessemer started with a simple experiment [52], using two hardened rolls and a small nine kilogram-capacity crucible (Fig. 2.8a). The process was patented in 1865 for the strip casting of steel and iron, as shown in Fig. 2.8b [53]. The first twin roll caster for Al alloy was introduced by Hunter Engineering, in the early 1950's [54].

There are two different types of TRC; vertical and horizontal [48]. In the vertical TRC (Fig. 2.9), the melt pours through a nozzle into the gap between the rolls that rotate toward each other. The rolls are made of steel [55, 56] or copper [57-60]. Side dams are used to form the melt pool on the top of roll gap. As soon as the melt contacts the rotating rolls, a solidified shell forms adjacent to each roll surface. These two shells are welded by the roll separation force at the tip of rolls [51]. The presence of the roll separation force is

necessary in order to weld the shells; otherwise the melt would flow out through the gap in the rolls [51]. It should be noted that a very high separation force causes extreme strip deformation which can lead to segregation by forcing the solute rich liquid out through the shell [51]. The horizontal TRC consists of tundish, nozzle, and rolls. The molten metal is transferred to the tundish where the temperature is stabilized and controlled before being shot through a horizontal nozzle into the rolls.

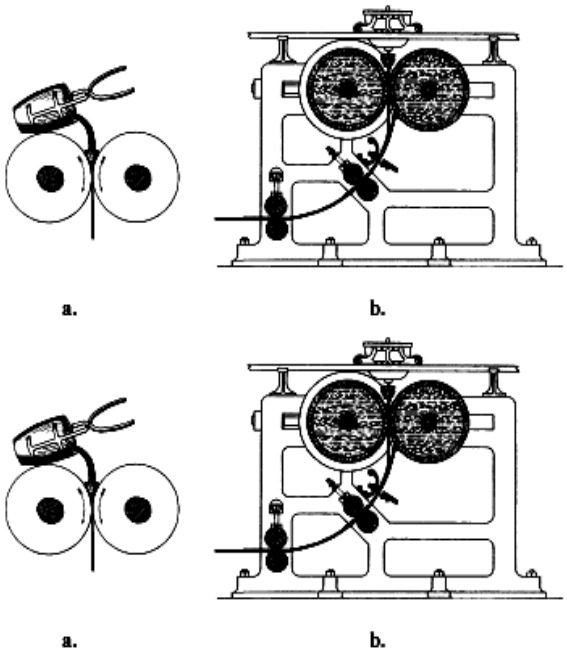

Figure 2.8 Schematic depiction of strip caster by H. Bessemer strip caster patented in 1865 [52, 53].

It is claimed that all alloys can be cast successfully by the twin-roll process if process parameters are well controlled [54]. These parameters include: casting speed, tip set-back, metallostatic head, melt superheat, grain refinement, roll separation force, roll lubrication, roll cooling and roll surface condition [54]. TRC is a commercialized process to produce thin Al sheet directly from the melt, mostly for dilute alloys. A similar technology is used for Mg strip production [48-50]. AZ31 strips of 600 to 700 mm width and 3.0-7.0 mm thickness have already been produced continuously by POSCO and Mg Flachprodukte GmbH [48, 50].

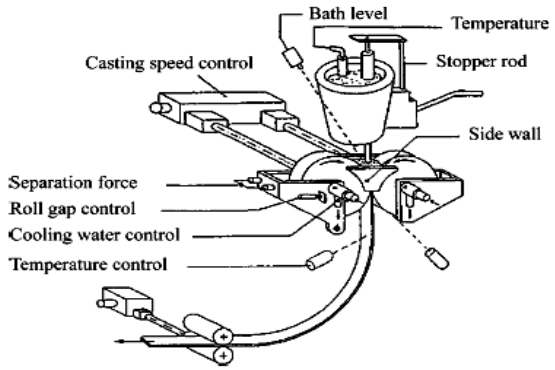

Figure 2.9 Schematic view of twin roll caster with controlled parameters [51].

2.6.3 Twin Roll Casting of Magnesium

Mg strips have been cast from standard alloys (AZ31, AZ61, AM60, AZ91) [50, 57, 59, 61, 62], as well as from certain experimental alloys (AM30+0.2RE, AM31+0.2Ca and AZ41, AZ31+0.7Ca) [62-65]. Some challenges that can be faced during strip casting of Mg alloys include:

(i) If an effective protection system is not used, molten Mg quickly oxidizes and ignites. A high quality strip requires a safe and simple protection system [61, 66].

(ii) Due to the low heat capacity of Mg alloys, liquid Mg freezes faster than liquid Al alloys, therefore making it more difficult to achieve uniform solidification across the strip [61, 66].

(iii) Due to the higher solidification range (about 65 ^{o}C for AZ31, 10~25 ^{o}C for Al alloys 1xxx, 3xxx and 8xxx), the extent of segregation in the AZ31 alloy is more than that of commercial Al alloys [50, 61, 66].

Due to the fast solidification rate of Mg alloys, casting speed and temperature are two very important factors in the TRC process [66]. It is very important to match casting speed with casting temperature, otherwise the casting process could be interrupted due to melt leaking or sticking. Generally, as the strip thickness decreases the castability decreases and the process becomes more susceptible to small changes of process variables. Low pouring temperature is beneficial to form a structure with fine grains, but in this condition, the control of the process becomes increasingly difficult [66]. Yang *et*

al. [66] reported that casting speeds of 8-15 m min^{-1}, and casting temperatures of 640 to 660 ^{o}C are necessary to produce high quality AZ31 strips.

i) As-cast Micro- and Macro-Structure

Cooling rates achieved in the TRC process are in the range of one to several hundred degrees per second [55, 59, 61, 67]. For AZ31, a dendrite arm spacing of 3 to 6.5 μm has been reported, which is much finer than that of 34 μm for DC ingot [55, 59, 68]. This SDAS size was reported to correspond to a cooling rate of 130 to 556 K s^{-1} for AZ31 [55, 59, 68]. These cooling rates are significantly higher than that of ~10 K s^{-1} for DC ingot [59, 67, 68]. This high cooling rate has a significant effect on microstructure, grain size and morphology. All of these characteristics can significantly influence the mechanical properties of finished sheet products [61].

The microstructure of twin-roll cast AZ31 roll is shown in Fig. 2.10, note the chilled zone close to the strip surface [50]. Next to this chilled zone, due to directional heat transfer, a columnar-grain structure is formed toward the mid-thickness region of the strip [50, 55, 59, 67, 69]. In the central region of the strip, due to lower cooling rates, an equiaxed grain structure is formed. Process parameters such as casting speed and cooling rate significantly effect the width of the columnar and central equiaxed grains and the extent of centerline segregation [50].

In TRC, macrosegregation is common due to the roll separating force which squeezes the solute-rich liquid from the mid-thickness region to the outer surface [59]. This inverse segregation is more vigorous for alloys with wider freezing ranges (with high solute content). Centerline segregation is attributed to backwards squeezing of solute rich liquid towards the sump, caused by the rolling action [54]. As the casting speed increases, due to the increase in sump depth, the centerline segregation becomes more significant [54]. This negative segregation can be decreased by controlling the roll separation force which is a function of several process parameters such as melt feeding, roll speed and roll gap [59]. Centerline segregation (channel segregates) have been reported by many researchers [50, 55, 67]. Elemental analysis using electron-probe microanalysis (EPMA) by Nakaura *et al.* [55, 67] revealed that centerline segregation is

rich in Al and Zn with a distribution of coarse Al-Mn intermetallics. However, Park *et al.* [59] could not detect any noticeable macrosegregation through the thickness of horizontal TRC AZ31.

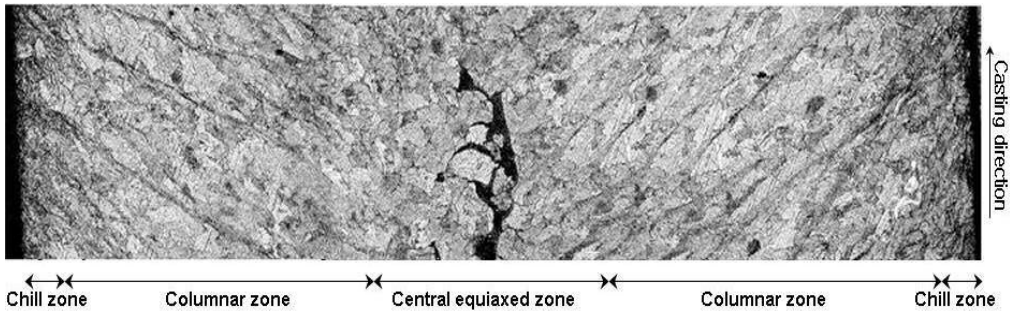

Figure 2.10 Microstructure of as-cast Mg AZ31 sheet using twin-roll [50].

It has been reported that the general microstructural features of TRC AM30+0.2RE, AM31+0.2Ca and AZ41, AZ31+0.7Ca are similar to those of TRC AZ31, including the chill zone, columnar grains and equiaxed grains in the mid-thickness of the sheet [62-65]. However, Kim *et al.* [70] observed equiaxed dendritic structures in ZMA61(Mg-6wt.%Zn-1wt.%Mn-1wt.%Al), but columnar dendritic structures in ZW61(Mg-6wt.%Zn-1wt.%Y). This was attributed to a larger freezing range of ZMA611 (260 ^{o}C) compared to that of ZW61 (100 ^{o}C). Park *et al.* [71] observed that as the amount of Al in TRC ZMA61X alloy (Mg-6wt.%Zn-1wt.%Mn-Xwt.%Al) increased, the grain size reduced. This is expected due to an increasing freezing range and the growth restriction factor of Al. The ZM61 and ZMA611 show uniform as-cast microstructures. However, due to the presence of secondary phases near the outer surfaces of the strip (the surface in contact with the rotating rolls), ZMA613 shows a non-uniform as-cast microstructure (Fig. 2.11) [71]. Secondary phases which precipitate along the grain boundaries and form a continuous network were $MgZn_2$, $MgZn_2$ and Al_8Mn_5 in ZM61, ZMA611 and ZMA613 alloys respectively [71]. The coarse phase present in ZMA613 alloy was found to be $Mg_{21}(Al,Zn)_{17}$.

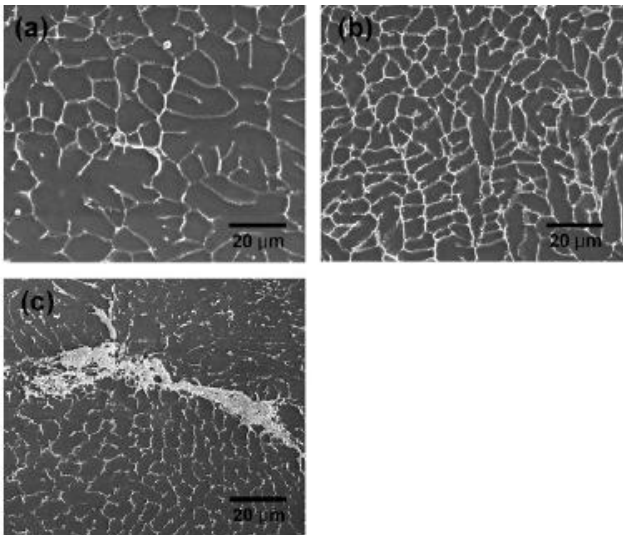

Figure 2.11 Micrographs of as TRC ZM61–Al alloys: (a) ZM61, (b) ZMA611 and (c) ZMA613 [71].

ii) Effect of Thermo-mechanical Processing

Annealing of TRC AZ31 quickly transforms the columnar grain structure to fine equiaxed grains (Fig. 2.12). The retained stress in the columnar grain structure (due to the hot rolling of twin-roll casting) is the driving force for this transformation. It was reported that annealing also reduces the segregation in the central region [50]. The addition of Ca reduces the grain size of annealed and rolled-annealed TRC AZ31 [65].

(a) 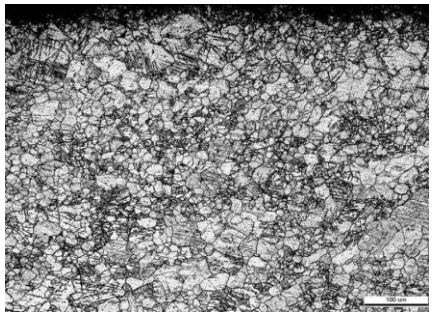 (b) 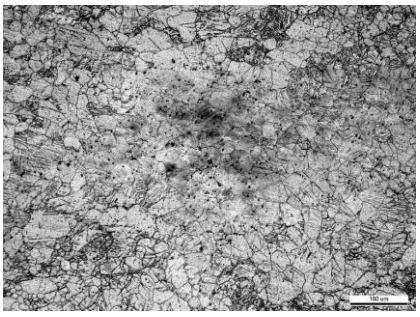

Figure 2.12 Microstructure annealed Mg sheet in casting direction. (a) Columnar region, and (b) central region [50].

The microstructure of AZ31 sheet after strip casting/warm rolling process is shown in Fig. 2.13. Fine equiaxed grains with an average size of 6μm can be achieved,

which is much finer than that of DC cast/warm rolled (of about 17μm) [50, 59, 67-69]. After warm rolling and subsequent annealing the microstructure of TRC AM30+0.2RE, AM31+0.2Ca and AZ41, was found to be finer and more homogenous compared to that of DC casting [62-64].

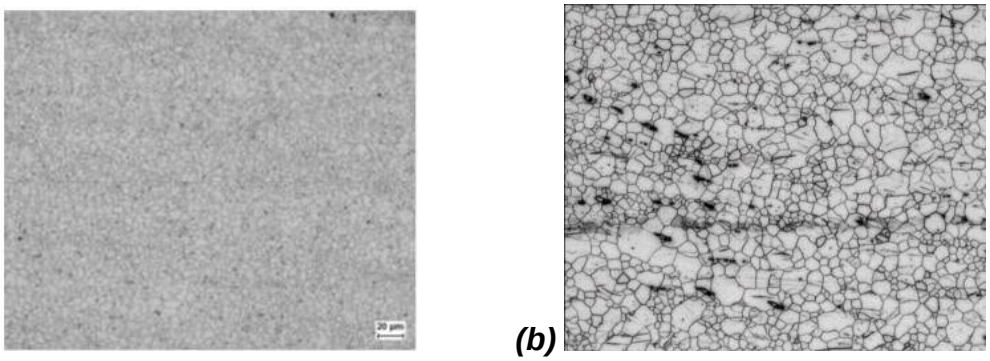

Figure 2.13 Microstructure of as-rolled AZ31 (a) twin-roll strip cast / warm rolled (b)DC cast / warm rolled commercial products [50].

As seen in Fig. 2.14, after T4 solution treatment a finer grain structure forms in all ZMA (Mg-Zn-Al) alloys [71]. As the amount of Al increases the grain structure is refined. As shown in Fig. 2.13d, the coarse phase, presented in the as-cast ZMA613 alloy, was decomposed into other phases [71]. The average grain size of rolled-annealed TRC ZMA611, was found to be 4μm, which is finer than that of TRC AZ31 (6μm) in H24 condition [69].

iii) Mechanical Properties

The mechanical properties of as-rolled/as-cast TRC AZ31 sheet have been compared with those of sheets produced by conventional DC casting/warm rolling process. The results obtained by some researchers are given in Table 2 [50, 61], which shows that the tensile properties of the sheet depend on the thermo-mechanical history [50, 67]. For example, the tensile strength of TRC AZ31 strip (non-homogenized) is higher than that of the conventional DC sheet, but the elongation is lower [55, 67]. In the homogenized condition, the elongation of the TRC sheet increases remarkably [55, 67]. The homogenized strip shows higher elongation than the conventional sheet, however its

tensile strength is equal to that of the non-homogenized strip [55, 67]. Improvement of elongation is attributed to the reduction of microsegregation by homogenization [55, 67]. In general, the tensile properties of sheets produced by TRC are equivalent to those produced by conventional DC/warm rolling processes [50, 55, 59, 61, 67-69].

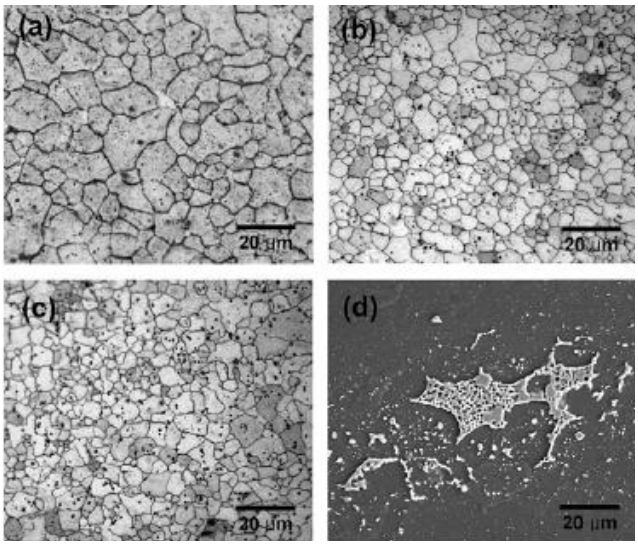

Figure 2.14 Micrographs of TRC ZM61–Al alloys in T4 condition (a) ZM61, (b) ZMA611, (c, d) ZMA613 [71].

Table 2.2 Mechanical Properties of AZ31 Sheet Produced by TRC/Coil Rolling Process Compared with Commercial Products Produced by DCCasting/ Warm Rolling Process

	0.2%Ys(MPa)	UTS(MPa)	Elongation (%)
TRC as annealed [50]	195-210	280-295	18-21
TRC as rolled [50-]	250-265	305-310	13-15
TRC, rolled and annealed [58]	160-180	270-290	13-17
TRC (CSIRO) [58]	213±5	288±5	21±2
Conventional (MEL) [50]	246	295	20
Conventional (Osaka Fuji) [50]	155	245	22
6111-T4	165	295	26

iv) Texture

Texture differences are observed between the central layer and the near-surface layers (80% of strip thickness) of the as-cast TRC AZ31 strip [72, 73]. The central layer of the TRC strip exhibits a weak textured structure [72]. In the layer close to the surface, most

of the crystals are orientated with their basal planes tilted about 45° across the casting direction [72].

Rolling at 400 ^{o}C leads to a texture characterized by basal poles tilted towards the sheet normal; it was observed that the texture intensity is related to the amount of strain per rolling pass (Fig. 2.16) [72, 73]. It was also observed that as the rolling temperature increased, the texture intensity decreased [72].

It was reported that rolled-annealed TRC AZ31 has a weaker texture in comparison to DC cast AZ31 alloy [65]. It was reported that the addition of Ca to TRC AZ31 weakened the texture of rolled-annealed strip [65]. ZMA61(Mg-6wt.%Zn-1wt.%Mn-1wt.%Al) and ZW61(Mg-6wt.%Zn-1wt.%Y) in the as-cast condition presented basal texture, however ZMA611 showed a weaker basal texture than ZW61 [70]. Subsequent homogenization weakened the basal texture of both ZMA611 and ZW61 while both had similar texture intensities [70]. However, after rolling and following annealing the basal texture intensity of ZMA611 was stronger than that of ZW61 [70].

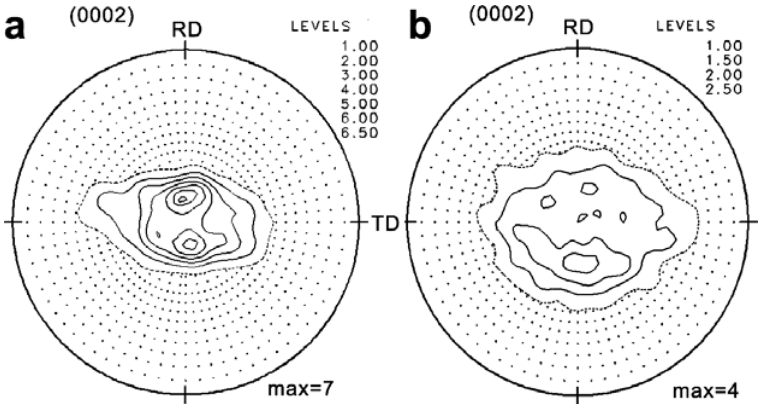

Fig. 2.15 Texture of the as-received TRC material (a) and upon annealing at 400 ^{o}C for 20 h (b) presented in terms of (0002) recalculated pole figures [73].

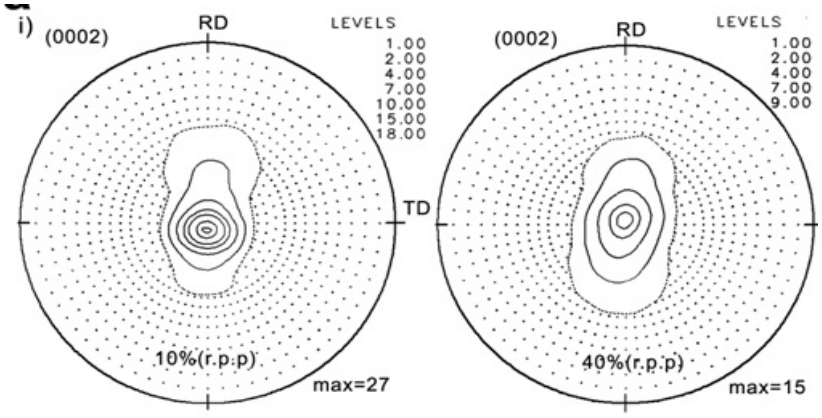

Fig. 2.16 Texture development during rolling at 400 ^{o}C up to 90% final thickness reduction using 10% and 40% reduction per pass [73].

2.7 Summary

In summary, the addition of RE and Y weakens the texture of magnesium alloys, and this is a subject which remains under investigation. The second phases in AZ alloys (e.g. AZ31) can be modified with alkaline earth (Sr, Ca) and RE elements (e.g. Ce) to precipitate very fine intermetallics [74-78]. It is known that second phase particles, depending on their size, spacing and amount can increase the driving force for recrystallization and act as nucleation sites [41]. This effect is not well understood; therefore systematic research to fully understand the effects of these elements on the microstructure and texture of rolled Mg sheet alloys is required for the development of Mg sheet alloy.

2.8 References

1. M. M. Avedesian, H. Baker, Magnesium and Magnesium Alloys 1999: ASM International, Materials Park, OH 44073-0002, USA, . pp. 314.
2. G. E. Dieter, Mechanical Metallurgy. 1976, New York: McGraw-Hill.
3. E. F. Emley, Principles of Magnesium Technology. 1966, London: Pergamon Press.
4. M. Barnett, Metall. Mater. Trans. A, 2003. 34(9): pp. 1799-1806.
5. G. V. Raynor, The Physical Metallurgy of Magnesium and its Alloys. 1959, New York: Pergamon Press.

6. Koike, T. Kobayashi, T. Mukai, H. Watanabe, M. Suzuki, K. Maruyama, K. Higashi, Acta Materialia, 2003. 51(7): pp. 2055-2065.
7. M.Yoo, Metall. Mater. Trans. A, 1981. 12(3): pp. 409-418.
8. P.G. Partridge, Metall. Metallurgical Rev., 1967. 12(26): pp. 169-194.
9. W. H. Hartt, R. E. Reed-Hill, Trans TMS-AIME, 1968. 242: pp. 1127–1133.
10. A. Jager, P. Lukac, V. Gartnerova, J. Haloda, M. Dopita, Mater. Sci. and Eng. A 2006. 432: pp. 20–25.
11. F. Kaiser, J. Bohlen, D. Letzig, K.-U. Kainer, A. Syczynski, C. Hartig, Adv. Eng. Mater., 2003. 5(12): pp. 891-896.
12. M. R. Barnett, M. D. Navea, C. J. Bettlesb, Mater. Sci. Eng. A 2004. 386: pp. 205–211.
13. H. T. Jeong, T. K. Ha, J. Mater. Process. Technol. 2007. 187–188: pp. 559–561.
14. S.-H. Kim , B.-S. You., C. D. Yim, Y.-M. Seo, Mater. Lett. 2005. 59: pp. 3876 – 3880.
15. Q. Jin, S. Y. Shim, S. G. Lim, Scr. Mater., 2006. 55(9): pp. 843-846.
16. L. Jiang, J. J. Jonas, A. A. Luo, A. K. Sachdev, S. Godet, Scr. Mater., 2006. 54(5): pp. 771-775.
17. S. R. Agnew, M. H. Yoo, C. N. Tomé, Acta Metall., 2001. 49(20): p. 4277-42
18. S. L. Couling, J. F. Pashak, L. Sturkey, Trans ASM, 1959. 51: pp. 94-107
19. P. E. Krajewski, , in H. Kaplan (Ed.) Magnesium Technology 2002 TMS, pp. 175-179.
20. S. R. Agnew, O. Duygulu, Mater. Sci. Forum, 2003. 419-422 (part1): pp. 177-188.
21. D. R. Askeland, P. P. Phule, Essentials of Materials Science and Engineering. 1 ed. 2004: CENGAGE-Engineering.
22. Y. Miyahara, K. Matsubara, K. Neishi, Mater. Sci. Forum, 2003. 419-422 (Part 1): pp. 551-556.
23. M. Fujita, N. Sakate, S. Hirahara, Y. Yamamoto, SAE Paper 950422. 1995. doi:10.4271/950422
24. J. E. Gruzleski, A. Aliravci, , US Patent US005143564A, Sep 1992.

25. Y. C. Lee, A. K. Dahle, D. H. St.John, Metall. Mater. Trans. A, 2000. 31A(11): pp. 2895-2906.
26. A. Yamashita, Z. Horita, T. G. Langdon, Mater. Sci. Eng., A, 2001. 300(1-2): pp. 142-147.
27. T. Mukai, M. Yamanoi, H. Watanabe, K. Higashi, Scr. Mater., 2001. 45(1): pp. 89-94.
28. E. Yukutake, J. Kaneko M. Sugamata, Mater. Trans., 2003. 44(4) pp. 452-457.
29. Y. Chino, H. Iwasaki, M. Mabuchi, Mater. Sci. Eng. A 2007. 466: pp. 90–95.
30. K. Iwanaga, H. Tashiro, H. Okamoto, K. Shimizu, J. Mater. Process. Technol., 2004. 155-156: pp. 1313-1316.
31. J. Bohlen, M. R. Nürnberg, J. W. Senn, D. Letzig, S. R. Agnew, Acta Mater., 2007. 55(6): pp. 2101-2112.
32. Y. Chino, M. Kado, M. Mabuchi, Mater. Sci. Eng. A, 2008. 494(1-2): pp. 343-349.
33. Y. Chino, Sassa K., M. Mabuchi, , Mater. Sci. Eng. A, 2009. 513-514: pp. 394-400.
34. D. H. Kang, D.W. Kim, S. Kim, G. T. Bae, K. H. Kim, and N. J. Kim, Scr. Mater., 2009. 61(7): pp. 768-77
35. L.W.F. Mackenzie, M. Pekguleryuz, Mater. Sci. Eng. A, 2008. 480(1-2): pp. 189-197.
36. L.W.F. Mackenzie, M. O. Pekguleryuz, Scr. Mater., 2008. 59(6): pp. 665-668.
37. K. Hantzsche, J. Bohlen, J. Wendt, K. U. Kainer, S. B. Yi, D. Letzig, Scr. Mater. 2010. 63(7): pp. 725-730.
38. N. Stanford, , D. Atwell, and M. R. Barnett, Acta Mater., 2010. 58(20): pp. 6773-6783.
39. L. W. F. MacKenzie, B. Davis, F. J. Humphreys, G. W. Lorimer, Mater. Sci.Technol., 2007. 23(10): pp. 1173-1180.
40. E. A. Ball, P. B. Prangnell, Scr. Mater., 1994. 31(2):p p. 111-116.
41. F. J. Humphreys, M. Hatherly, Recrystallization and Related Annealing Phenomena. 2 ed. 2004: Great Britain by Galliard Ltd., UK, .
42. R. E. Reed-Hill, R.Abbaschian, Physical Metallurgy Principles. Third ed, 20 Park Plaza, Boston, MA: PWS.
43. A. Becerra, M. Pekguleryuz, J. Mater. Res, 2008. 23: pp. 3379.

44. J. Hirsch, K. Lücke, Acta Metall., 1988. 36(11): pp. 2863-2882.
45. K. Hirai, H. Somekawa, Y. Takigawa, K. Higashi, Scr. Mater., 2007. 56(3): pp. 237-240.
46. M. Suzuki, T. Kimura, J. Koike, K. Maruyama, Scr. Mater. 2003. 48(8): pp. 997-1002.
47. H. E. Friedrich, B. L. Mordike, Magnesium technology : metallurgy, design data, applications 2006: Berlin ; New York : Springer, c2006.
48. B. Engl, , Light Metal Age, 2005. 63(5) ,pp. 14-19.
49. W. Borbige, D. D Liang, Magnesium Alloy Sheet and Its Production. 2006, US2006231173: USA.
50. I.-H. Jung, W. Bang, I. J. Kim, , H. I.Sung, , W. J.Park,; D. Choo, , S. Ahn, , in: R. S. Beals (Ed.) Magnesium Technology. 2007 TMS Orlando, FL, USA pp. 85-88.
51. K. Schwerdtefeger, , ISIJ International, 1998. 38 (8), pp. 852-861.
52. H. Bessemer, Eng. Min. J., 1891: pp. 473-474.
53. Bessemer, H. 1865: USA49053.
54. R. Cook, P. G. Grocock, P. M. Thomas, D. V. Edmonds, J. D. Hunt, J. Mater. Process. Technol., 1995. 55(2): pp. 76-84.
55. Y. Nakaura, A. Watanabe, K. Ohori, Mater. Trans., 2006. 47(7): pp. 1743-1749.
56. T. Haga, K. Tkahashi, M. Ikawaand, H. Watari, J. Mater. Process. Technol., 2004. 153-154: pp. 42-47.
57. H. Watari, T. Haga, R. Paisern, N. Koga, K. Davey, Key Eng. Mater. 2007. 345-346(1): pp. 165-168.
58. T. Haga, , H. Watari, S. Kumai, J. Ach. Mater. Manuf. Eng. 2006. 15(1-2): pp. 186-192.
59. S. S. Park, J. G.Lee, H. C. Lee, N. J. Kim, , in A.A. Luo(Ed.) Magnesium Technology 2004 TMS, USA, pp. 107-112.
60. H. Watari, , T. Haga, , N. Koga, , K. Davey, , J. Mater. Process. Technol., 2007. 192-193:p p. 300-305.
61. D. Liang, , C. B. Cowley, JOM, 2004. 56(5): pp. 26-28.
62. S.-r. Wang, M. Wang, S. b. Kang, J. h. Cho, Trans. NONFERR METAL SOC, 2010. 20(5): pp. 763-768.

63. H. Chen, S. B. Kang, , H. Yu, H. W. Kim, G. Min, Mater. Sci. Eng., A, 2008. 492(1-2): pp. 317-326.
64. Y. Wang, S. B. Kang, J. Cho, J. Alloys Compd., 2011. 509(3): pp. 704-711.
65. G. Bae, J. Bae, D. H. Kang, H. Lee, N. Kim, Met. Mater. Int. 2009. 15(1): pp. 1-5.
66. C. Yang, , P. Ding, , D. Zhang, , F. Pan, , Mater. Sci. Forum. 2005. pp. 427-430.
67. Y. Nakaura, K. Ohori, Mater. Sci. Forum. 2005. pp. 419-426.
68. S. S. Park, G. T. Bae, J. G. Lee, D. H., Kang, K. S. Shin, N. J. Kim, , Mater. Sci. Forum, 2007, 539-543, pp. 119-126.
69. S. S. Park, D. H. Kang, , G. T. Bae, N. J. Kim, Mater. Sci. Forum, 2005. 488-489: pp. 431-434.
70. K. H. Kim, B. C. Suh, J. H. Bae, M. S. Shim, S. Kim, N. J. Kim, Scr. Mater. 2010, 63(7): pp. 716-720.
71. S. S. Park, G. T. Bae, D. H. Kang, I. H.Jung, K. S. Shin, N. J. Kim, Scr. Mater., 2007. 57(9): pp. 793-796.
72. R. Kawalla, M. Oswald, C. Schmidt, M. Ullmann, H.-P. Vogt, N. D. Cuong, , in (Ed.), Magnesium Technology,TMS 2008, USA, pp. 177-182.
73. T. Al-Samman, G. Gottstein, Scr. Mater. 2008. 59(7): pp.760-763.
74. L. Shang, I. H. Jung, S. Yue, R. Verma, E. Essadiqi, J. Alloys Compd., 2010. 492(1-2): pp. 173-183.
75. L. Koubichek, Metallurgy of Non-Ferrous metals, I. V. O. Z. Vedeny, (Ed.), 1959. pp. 153-157.
76. M. O. Pekgüleryüz, M. M. Avedesian, DGM, B. L. Mordike, F. Hehman, (Eds.) Germany, 1992, pp. 213-220.
77. C. A. Aliravci, J. E. Gruzleski, F. C. Dimayuga, Am. Foundry Soc. Trans., 1992: pp. 92-115.
78. M. O. Pekgüleryüz, A. Luo, P. Vermette, M. M. Avedesian, Proc. 50th Ann. World Magnesium Conf., Washington, D.C., 1993: pp. 20-27.

CHAPTER 3

MICROSTRUCTURE AND TEXTURE STUDIES ON TWIN-ROLL CAST AZ31 MAGNESIUM ALLOY

In this Chapter, studies on the microstructure and texture of twin-roll cast AZ31 alloy are presented. The chapter is comprised of three sections; each section is a published journal manuscript. The first section (3.1 Effect of Cooling Rate on the Microstructure of AZ31 Magnesium Alloy) details experiments determining the relationship between cooling rate (an important parameter governing the microstructure development in twin roll cast Mg sheet) and the microstructure of AZ31 alloy. Here, a relationship between secondary dendrite arm spacing, λ, and the cooling rate, CR was determined as $\lambda = 85.15\ (CR)^{-0.42}$. It was noted that the dendrite arm spacing exerts important effects on the mechanical properties and subsequent workability of the sheet. Section 3.2 (Alleviation of Basal Texture in Twin-Roll Cast Mg-3Al-1Zn Alloy) reports on an important contribution of the thesis: the effective use of a post-annealing treatment to alter the basal texture of TRC AZ31. Section 3.3 (Microstructure and Texture Studies on Twin-Roll Cast AZ31 (Mg-3wt%Al-1wt%Zn) Alloy and the Effect of Thermomechanical Processing) details microstructural and texture studies of the (i) as-received, (ii) rolled, (iii) rolled-annealed, and (iv) post-annealed TRC AZ31 and discusses the mechanism of texture alteration during the post- annealing treatment at 420 ^{o}C.

3.1 Effect of Cooling Rate on the Microstructure of AZ31 Magnesium Alloy*

* This section has been published: **Masoumi, M.**, Pekguleryuz, M., "Effect of Cooling Rate on the Microstructure of AZ31 Magnesium Alloy" Transactions of the American Foundry Society 2009, Vol. 117, pp. 617-626.

The influence of cooling rate (CR) on the casting structure of AZ31 magnesium alloy has been investigated using different moulds to obtain slow to moderate cooling rates. The results show that grain size and secondary dendrite arm spacing (SDAS) reduces as the cooling rate increases. SDAS, λ, was related to cooling rate as $\lambda = 85.15(CR)^{-0.42}$ where λ is in μm and CR is cooling rate in ^{o}C/s. It was observed that the fraction of secondary phases increases and the secondary phase particles become finer with an increase in cooling rate.

3.1.1 Introduction

Magnesium is the lightest structural metal with a density of 1.74 g/cm^3; 35% lighter than Al and over 400% lighter than iron [1]. Automotive applications of magnesium alloys have received significant attention for the purpose of vehicle weight reduction and high pressure die-casting (HPDC) alloys are already used in automotive components [2, 3]. Currently there is an interest in the using gravity casting and wrought alloys in automotive powertrain and body applications. The interest in twin-roll cast magnesium for sheet applications is growing; however, the cast structure and how this influences the deformation behaviour of magnesium alloys are not well-understood.

It is well known that the cooling rate (solidification process) has a great influence on the microstructure and the mechanical properties of alloys. Even though, this effect is more pronounced when casting is the final product, wrought products can also be affected by the as-cast structure. In wrought alloys, the solidification structure and the related defects, once created, are difficult to eliminate and influence the deformation structures. Therefore, control of the solidification process often becomes vital in product quality [4].

Dendrite arm spacing and grain size measurements are the most common methods used to study solidification structures [5]. An increase in solidification rate results in a

reduction in dendrite arm spacing, grain size, and an improvement in mechanical properties. Ductility and tensile strength are the properties that are influenced the most by CR [5].

A dendritic structure is usually observed in the conventional solidification conditions of casting alloys. The core segment of the dendrite structure which grows approximately in the heat-extraction direction is called primary dendrite arm; the spikes perpendicular to the primary dendrite arm are secondary dendrites arms (SDAS) [5]. It is known that dendritic growth is strongly crystallographic. The primary arms are oriented parallel to specific crystallographic directions close to the direction of heat-extraction. For example, in FCC metals and alloys, these are the <001> directions [6]. Dendrite morphology remains largely unchanged over a wide range of solidification rates; however, the dendrites become finer as the rate of heat extraction increases. One exception to this rule is that at very high cooling rates, when primary arm spacing becomes very small, secondary arms may be absent [5]. In general the dendrite arm spacing could be related to CR, as:

$$\lambda = a\,(CR)^{-n} \qquad \text{eq. (1)}$$

where the exponent n is the range of 1/3 to ½ for secondary spacings and generally very close to ½ for primary spacings [5].

Research conducted by Lin *et al.* [7] on the solidification structures of magnesium alloys has shown that that as the CR increases, the quantity of the solid-solution phase increases and the fraction of secondary phase, $Mg_{17}Al_{12}$, decreases. A single solid solution phase was obtained by using liquid nitrogen as a coolant. Dube *et al* [8] studied the microstructure of as-cast AZ91 under a range of cooling rates from 10^{-1} to 10^{6} Ks^{-1}. They obtained an equiaxed structure and found that the measured dendritic cell-size decreases exponentially with increasing cooling rates. Yang *et al.* [9] studied the effect of CR on the microstructure of ZK60, in range of 0.2 to 100 K/s, and showed that as the CR increases the grain size, secondary dendrite arm spacing, and the primary dendrite-arm spacing sharply decrease.

AZ31 (3wt.%Al-1wt.%Zn-0.3wt.%Mn) alloy is the most common commercial magnesium wrought alloy. Mg wrought alloys have in general limited formability due to

hexagonal close-packed structure and exhibit preferred orientation (texture). Recent interest in twin-roll-cast AZ31 has led to investigations on the possible links between the cast structure of AZ31 and the down-stream performance of the sheet. It is postulated that solidification structure may exert an influence on the formability and mechanical properties of alloy. The influence of the solidification conditions on the microstructure of AZ31 has not been studied in a systematic manner. The objective of this study is to investigate the effect of CR on the cast structure of AZ31.

3.1.2 Experimental Procedure

Melting of AZ31B, supplied by Timminco, was carried out in a 20 KW, 5 KHZ Norax Canada induction furnace, using a graphite crucible. A protective gas mixture of sulphur hexafluoride, SF_6, in a carrier gas of carbon dioxide, CO_2, was used to prevent melt oxidation. The temperature of the melt was closely monitored via a K-type (chromel-alumel) thermocouple. About 0.400 kg melt was prepared for each casting and the melt was poured from a casting temperature of 740 ^oC (1364F).

Thermal analysis setup consisted of an Omega 0.8 mm ungrounded type K (chromel-alumel) thermocouple inserted into the melt with stainless steel sheathing connected to a Grant Squirrel SQ2020 data acquisition system. The thermocouple was positioned halfway between the center and the side of the mould. Different cylindrical moulds were used (i.e. sand cup with a diameter and height of 30 mm and 50 mm, thin wall steel die with a diameter and height of 50mm and 25mm, graphite cup with a diameter and height of 30mm and 60mm, steel thick wall die with a diameter and height of 25 mm and 120 mm and copper die with a diameter and height of 40 mm and 17 mm) to obtain different cooling rates. To slow down the cooling rate, FibreFrax was used to insulate the mould (i.e. sand cup) or the melt was allowed to cool down inside the furnace (i.e. thin wall steel die). Fig. 3.1 shows the induction furnace and different mould which were used for this study.

In order to determine the cooling rate, the temperature range between 500-550 ^oC was considered. Hence, in the CR equation :

$$CR = \frac{Ts - Tf}{\Delta t} \qquad \text{Eq. (2)}$$

T_s and T_f are taken as 550 ^oC and 500 ^oC, respectively, and Δt is the elapsed time between Ts and T_f.

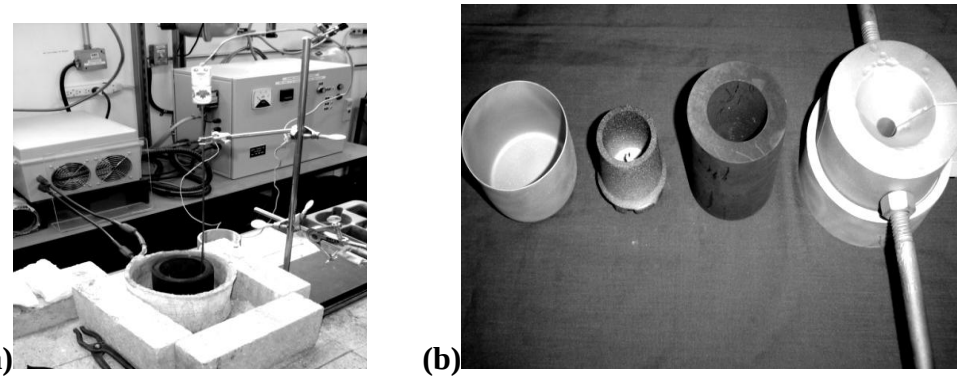

(a) **(b)**

Fig. 3.1 (a) Induction furnace (b) Moulds used in thermal analysis.

Metallographic samples were taken from a location close to the thermocouple tip. Samples were cold mounted and grounded on 240, 320, 400, 600 and 1200 grit SiC paper and then polished with 6μm, 3μm and 1μm diamond paste. The sample surface was cleaned using an ultrasonic bath prior to etching. The specimens were chemically etched with acetic-picral (10 ml acetic acid, 4.2 g picric acid, 10 ml H_2O, 70 ml ethanol (95%)) for optical microscopy. Etching was performed by immersing the sample for 3-5 seconds and then washing the surface with running water and ethanol and dried using a drier. A Clemex optical image analyzer, Epiphot 200, system and a Hitachi S-3000 variable pressure scanning electron microscope (VP-SEM) with a maximum resolution of 100 nm in a backscattered mode/1μm in X-Ray diffraction mapping mode were used for microstructural characterization. The grain sizes of samples were measured by image analysis according to ASTM E112-96 [10]. SDAS was measured using the mean-intercept method. The microhardness of matrix was determined, using a microhardness tester (Model: CM-100AT), in the as-polished/etched condition. The microhardness measurements were made using a pyramidal diamond indenter having a face angle of 136° and a 10-g indenting load with a dwell time of 15 s.

3.1.3 Results and Discussion

Fig. 3.2 shows typical cooling curve of samples cast in sand cup and graphite cup. The cooling rates in sand cup, thin wall steel die, graphite cup, steel thick wall die and copper die were measured as 0.55 ^{o}C/s, 2.05 ^{o}C/s, 9.3 ^{o}C/s, 16.8 ^{o}C/s and 38 ^{o}C/s, respectively.

Fig. 3.3 presents the optical microstructures of the AZ31 alloy with different cooling rates. The alloy solidified in the sand cup (Fig. 3.3.a) shows very coarse equiaxed grains. The samples cast in steel thin-wall die, graphite cup, steel thick-wall die also show an equiaxed grain structure but finer than that of the sand cup. The copper die gives the highest CR of about 38 ^{o}C/s; the directional heat transfer produces a columnar-grain structure with grains growing from the edge towards the center while the central region of coupon exhibits an equiaxed grain structure, due to segregation and constitutional undercooling.

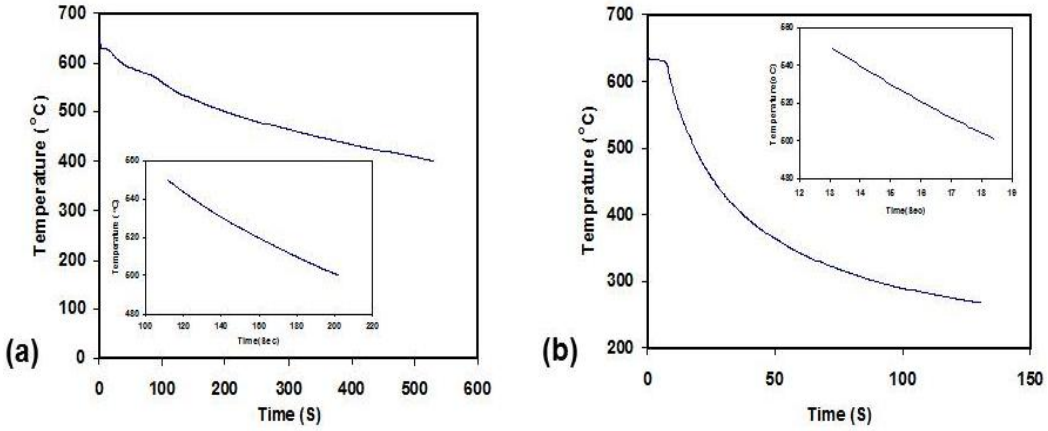

Fig. 3.2 Cooling rate curves of solidifying AZ31B: (a) sand cup (b) graphite cup.

SDAS measurement showed that secondary dendrite arm spacing reduced from 91 μm in sand cup to 15.4 μm in copper die as the CR increased from 0.55 to 38 ^{o}C/s. The relationship between cooling rate and the SDAS (Fig. 3.4.a) was determined to be as:

$$\lambda = 85.15(CR)^{-0.42} \qquad \text{Eq. (3)}$$

where λ is the SDAS in μm and CR is cooling rate in oC/s. This equation is in line with the equation determined for AZ91 by Dube *et al.* [8] and the general equation given by Fleming [5].

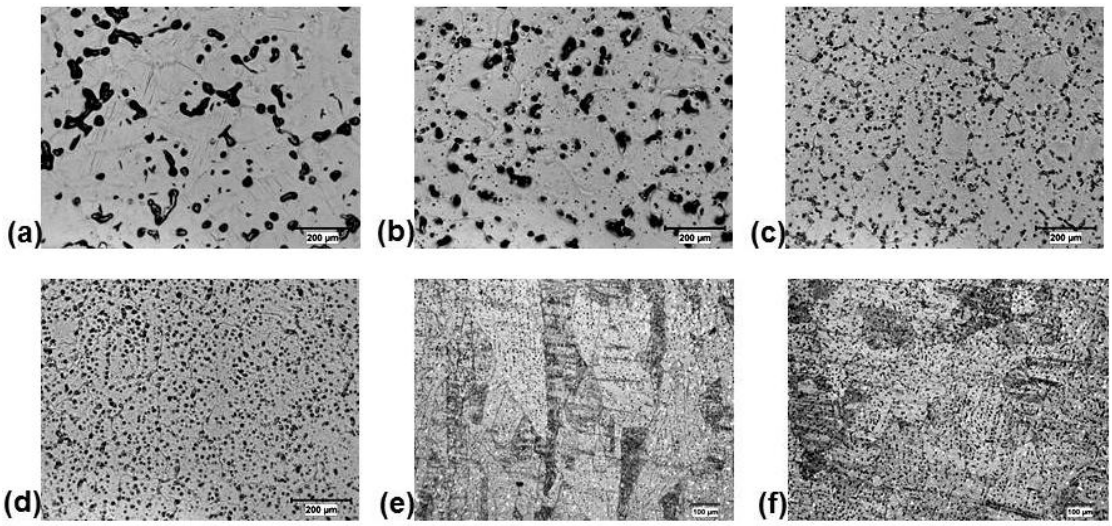

Fig. 3.3 As-cast microstructure of AZ31 cast in (a) sand mould (b) steel thin- wall die (c) graphite mould (d) steel thick wall die (e) copper die, edge (f) copper die, mid-thickness.

The grain size of AZ31 was determined by image analysis, shows that the grain size decreases with increasing CR (Fig. 3.4.b). The grain size, D, decreases from 413 to 195 μm with an increase of CR from 0.55 to 16.8 ^{o}C/s (due to presence of both columnar and equiaxed grains in samples cast in the copper die, the grain size of this sample was not measured). The relationship between cooling rate and the grain size (Fig. 3.4.b) was determined to be:

$$D = 373.6\ (CR)^{-0.228} \qquad \text{Eq. (4)}$$

where D is the grain size in μm and CR is cooling rate in ^{o}C/s.

As seen from the optical micrographs (Fig. 3.3), the secondary phase particles become finer and the density of secondary-phase particles in matrix increases with increasing CR. The average of particles size varies from 6.9 μm to 1.6 μm as the cooling rate increases from 0.55 ^{o}C/s to 38 ^{o}C/s (Fig. 3.5).

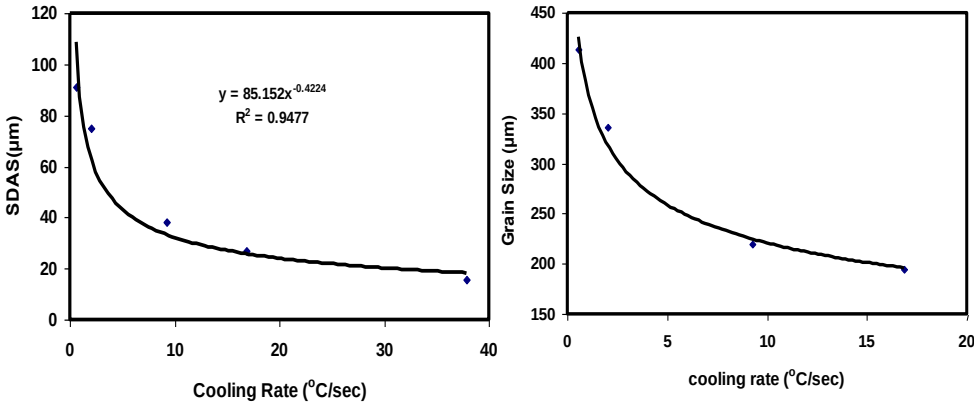

(a) (b)

Fig. 3.4 Effect of cooling rate on (a) grain size and (b) SDAS of AZ31B alloy.

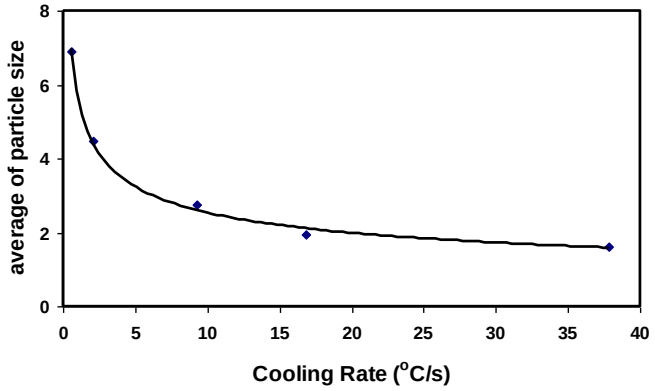

Fig. 3.5 The effect of cooling rate on the average size of secondary phases of AZ31 alloy.

In an effort to quantitatively determine the role of CR on the formation of secondary phases, the area fraction of secondary phases, f_{sp}, in AZ31 alloy under different CR was determined by image analysis. Fig. 3.6 shows that as CR increases, the f_{sp} increases from 2.9% to 9.7%. The phenomenon of an increase in f_{sp} with an increase in CR is attributed to Scheil non-equilibrium freezing which lowers the solute in the solid-solution phase and increases the amount of the secondary phases. At low CR (close to equilibrium) the back diffusion in the solid occurs and, as a result, the eutectic-phase fraction decreases. At much higher CR, the rejection of solute atoms from solid into the interface between the solid and liquid phases reduces and the eutectic transformation is

restrained so that a supersaturated single-phase solid solution forms. Sarreal *et al.* [11] studied the effect of CR on the second phase content of Al-Cu and Al-Si alloys solidified in the CR in the range of 0.06 to 10^5 K/s. They found that increasing the CR to 180 $^oK/s$ increases the amount of second phase. However, above this CR, the secondary phase content decreased with increasing cooling rate [11]. Their results were in good agreement with those obtained by Dutta [12] and Lin [7]. By considering the cooling rate range, the results obtained in this study agree with the results obtained (in the same cooling rate range) by Sarreal [11] and Dutta [12]. Furthermore, the semi-quantitative EDS analysis (on the matrix close to the secondary phases) indicates that the cooling rate increase from 0.55 to 38 $^oC/s$ corresponds to decrease in weight percentage of Al and Zn in solid-solution from 3.6 and 1.1 to 2.3 and 0.6, respectively. However, for the same increase in CR, the weight percentage of Mn in α-Al solid solution decreases from 0.54 to 0.18.

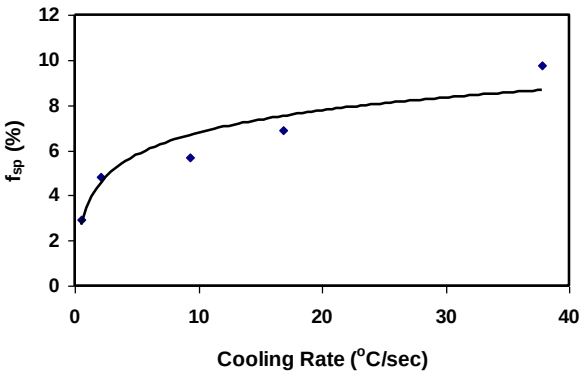

Fig. 3.6 The effect of cooling rate on the area fraction of secondary phases (f_{sp}) of AZ31 alloy.

In line with the observations above, the microhardness measurements of the aluminum solid-solution matrix show that as the cooling rate increases from 0.55 to 38 $^oC/s$, the hardness of matrix decreases from 55.5 to 48.5 HV, which is attributed to presence of lower amount of solute in the matrix, which reduces the solid-solution strengthening effect.

SEM micrographs and EDS analysis of AZ31 cast in copper die and sand cup are shown in Figs. 3.7-3.14. EDS spectra for both the copper die and the sand cup samples

confirms that, the matrix is α-Mg, and particles are Mg-Al-Zn phase (mostly likely $(Al,Zn)_{49}Mg_{32}$ [13]), and Al-Mn (it could be a mixture of $Al_{11}Mn_4$, Al_8Mn_5, Al_9Mn_{11} and β-Mn(Al) [14]) intermetallics. α-Mg in the sand cup consists of Mg-Al-Zn solid solution, however, in the copper die it consists of Mg-Al-Zn-Mn solid solution.

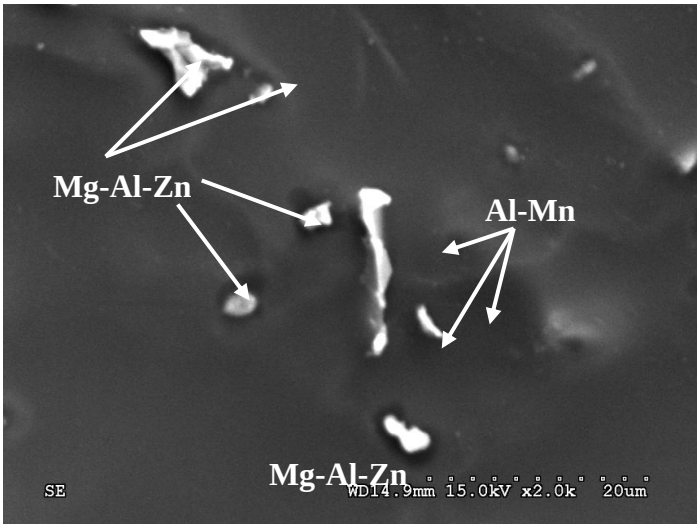

Fig. 3.7 SEM micrographs showing microstructure of AZ31 cast in copper die.

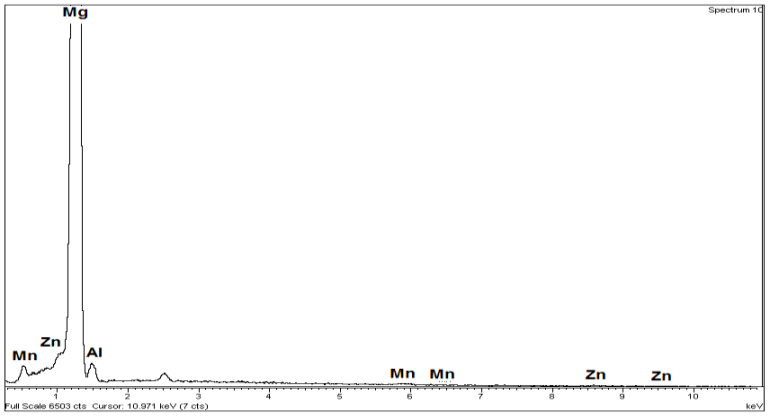

Fig. 3.8 EDS spectrum from the matrix in Fig. 7.

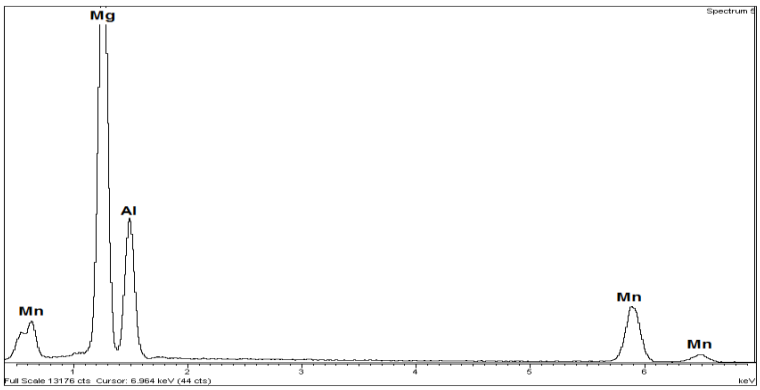

Fig. 3.9 EDS spectrum from the Al-Mn particles in Fig. 7.

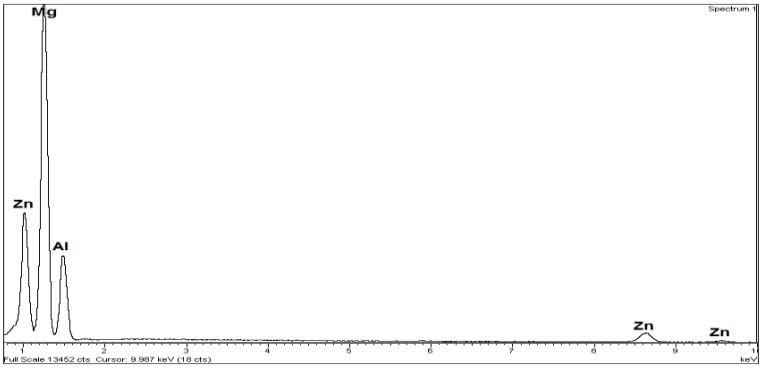

Fig. 3.10 EDS spectrum from the Mg-Al-Zn particles in Fig. 7.

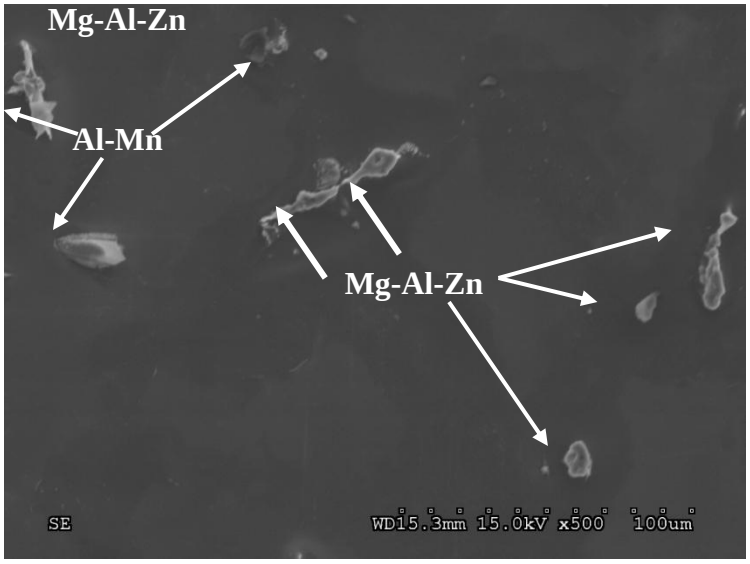

Fig. 3.11 SEM micrographs showing microstructure of AZ31 cast in sand cup.

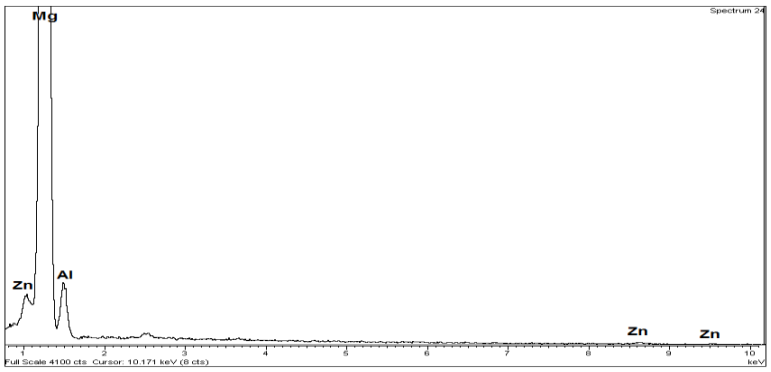

Fig. 3.12 EDS spectrum from the matrix in Fig. 11.

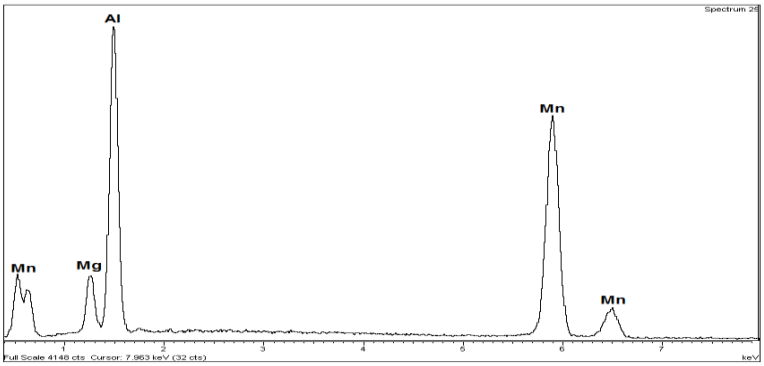

Fig. 3.13 EDS spectrum from the Al-Mn particles in Fig. 11.

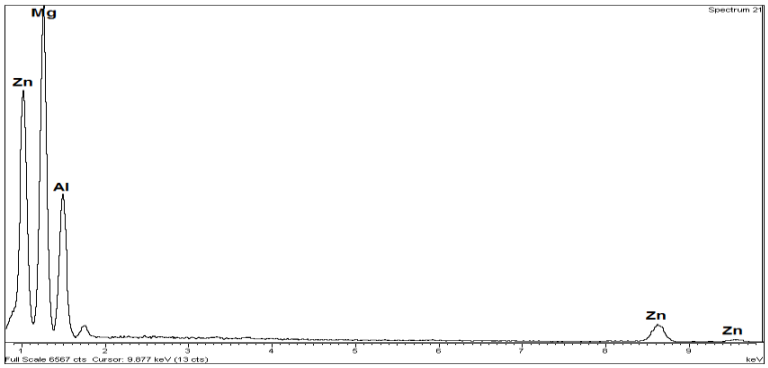

Fig. 3.14 EDS spectrum from the Mg-Al-Zn phases in Fig. 11.

The results are summarized in Table 3.1. As a general observation, it can be noted that as the cooling rate increases from 0.55 to 38 ^{o}C/s, the SDAS (λ) and the Grain size

(D) decrease which are in line with the previous observations in metallic alloy systems [5-9]. Also as CR increases to 38^{o}C/s, the fraction of the secondary phases (f_{sp}) increases and the α-Mg matrix hardness decreases in agreement with Scheil mode of solidification. However, the individual fractions of the second phases (i.e. Mg-Al-Zn versus Al-Mn) have not been determined. EDS shows that Mn is seen in the α-Mg at high CR; this implies that the increase in secondary phases is predominately due to the increase in Mg-Al-Zn intermetallics. It is likely that as Al is preferentially tied into the Mg-Al-Zn phase Mn is incorporated into the α-Mg as a solute rather than into the Al-Mn intermetallics. Mn is usually not associated any strengthening effect in Mg [15], so the Mn solute enrichment of the matrix does not compensate for the decrease in Al and Zn as is reflected in the microhardness measurements.

These results show that there is a trade-off of strengthening mechanisms: As CR increases; solute hardening is decreased in favour of second-phase hardening and grain size hardening. The implications for down-stream processing are more difficult to assess. Increased amount of precipitates that are refined can be beneficial for uniform deformation and recrystallization. On the other hand, the mixed mode of grain structure may exert an opposite influence.

Table 3.1 Comparison of AZ31 solidified in sand cup and copper mould.

R, ^{o}C/s	DAS, λ, μm	Grain Size, D μm	Pct. Second phase, $f_{sp,}$ %	Size of the secondary phases, $d_{sp,}$ μm	α-Mg Matrix microhardness HV	Phases
0.55	1	413	3	7	55.5	α-Mg (Mg, Al, Zn) Mg-Al-Zn intermetallics Al-Mn intermetallics
38	4	<200*	10	1.6	48.5	α-Mg (Mg, Al, Zn, Mn) Mg-Al-Zn intermetallics Al-Mn intermetallics

* estimated but not measured due to mixed columnar/equiaxed grain structure.

3.1.4 Conclusions

1. As the cooling rate increases from 0.55 to 38 ^{o}C/s, the grain sizes of Mg alloy AZ31 decreases. A relationship was found between cooling rate (CR) and grain size as $D= 373.6 (CR)^{-0.228}$;
2. The grain structure tends to be more dendritic and the secondary arm spacing SDAS becomes fine with increasing cooling rate as $\lambda = 85.15 (CR)^{-0.42}$;
3. As the cooling rate increases, the fraction area of secondary phases increases; this is attributed to non-equilibrium Scheil solidification;
4. SEM results reveal that the microstructure of AZ31 alloy consists of the primary α-Mg, Mg-Al-Zn and Mn-Al intermetallics and that the α-Mg contains Mn; and
5. The size of the second phases decrease from 6.9 to 1.6 μm with increasing cooling rate.

3.1.4 References

1. M. M. Avedesian, H. Baker, Magnesium and Magnesium Alloys 1999: ASM International, Materials Park, OH, 44073-0002, USA.
2. T. Kaneko, M. Suzuki, Mater. Sci. Forum, 2003 419-422(Part 1): pp. 67-72.
3. B. Engl, Light Metal Age, 2005. 63(5): pp. 14-19.
4. W. Kurz, D. J. Fisher, Fundamentals of Solidification. 1986, Trans Tech Publications Ltd. Pp. 245.
5. M. C. Flemings, Solidification Processing. 1974, New York, London and Sydney.: McGraw-Hill Book Co.
6. G. J. Davies, Solidification and Casting. 1973, New York, Halsted Press.
7. L. F. Yang, K-Q Qiu, L-J Chen, Z. Liu, Trans. Nonferrous Met. Soc. China, Dec. 2006. 16(Special 3): pp. 1698-1702.
8. D. Dube, A. Couture, Y. Carbonneau, M. Fiset, R. Angers, R. Tremblay, Int. J. Cast Met. Res., 1998, 11(3): pp. 139-144.
9. C. Yang, D. Zhang, P. Ding, J. Peng, X. Chen, Mater. Sci. Forum, 2005, 488-489: pp. 295-298.
10. Standard Test Methods Determining Average Grain Size 2000, ASTM E112-96.

11. J. A. Sarreal, G. J. Abbaschian, Metall. Trans. A., Nov. 1986. 17A(11): pp. 2063-2073.
12. B. Dutta, M. Rettenmayr, J. Mater. Sci. Technol., Dec. 2002. 18(12): pp. 1428-1434.
13. Metallography and Microstructures ed. Vander Voort G. F. Vol. 9. 2004: Materials Park, OH: ASM International,.
14. Cao, P., StJohn, D. H., Qian, M., Materials Science Forum, 2005. 488-489: pp. 139-142.
15. Emley, E. F., Principles of Magnesium Technology. 1966, London: Pergamon Press.

3.2 Alleviation of Basal Texture in Twin-Roll Cast Mg-3Al-1Zn Alloy *

*This section has been published: **M. Masoumi,** F. Zarandi, M. Pekguleryuz, "Alleviation of Basal Texture in Mg-3Al-1Zn" Scripta Materialia, *v*olume 62, Issue 11, June 2010, Pages 823-826.

Twin-roll cast (TRC) AZ31 alloy (Mg-3wt.%Al-1wt.%Zn) was subjected to annealing heat treatment at 420 ^{o}C which resulted in an important change in the original strong basal texture. It was observed that the unique TRC structure which is a combination of both cast and deformed structures, leads to this texture alteration upon annealing. The change in crystallographic orientation is attributed to the particle-stimulated nucleation of new grains with random orientations.

3.2.1 Introduction

The application of magnesium (Mg) in automotive bodies for weight reduction purposes is challenged by the relatively high cost of Mg sheet [1]. Twin-roll casting (TRC) produces cast and warm (or hot) rolled sheet with thicknesses less than six millimetres [2] in one process step and can considerably reduce the cost [3]. AZ31 (with nominal composition Mg-3wt.%Al-1wt.%Zn) is, currently, the most common Mg sheet alloy and, therefore, the prime candidate to be produced by TRC. The cold-rolled microstructure of AZ31 is known to contain extensive twinning [4]. Hot-rolled AZ31 and AZ31-H24 tend to have non-uniform (bimodal) grain structures [4, 5]. Rolling orients the {0001} basal planes approximately parallel to the sheet surface (which is known as the "basal texture"), with the $[10\bar{1}0]$ axis in the rolling direction (RD) [5-10]. Hot rolled AZ31 shows a perfect basal fibre texture; while warm-rolled sheet exhibits an egg-shaped distribution of {0001} planes in orientation pole figures [5-10]. A gradient of basal texture intensity from the surface to the mid-thickness of sheet has been reported in asymmetric hot rolling [5]. Commercially available AZ31 sheet is produced through several hot, warm, and cold rolling stages and the sheet retains a strong basal texture in all subsequent heat-treatments [11]. Since the basal texture lowers sheet formability (stamping, bending), considerable

effort is currently being directed to weaken the basal texture or obtain a random texture in Mg sheet [12]. Non-basal or weak textures have been reported in alloys based on rare-earth elements (Mg-RE alloys) [12-15] and in Mg alloys with low levels of Li [16]. However, non-basal textures have never been reported for AZ31. This paper discusses the alleviation of basal texture in AZ31 via annealing heat treatment of the TRC sheet. For comparison, a similar treatment is also studied in a commercial AZ31-H24 sheet.

3.2.2 Experimental Procedure

A TRC AZ31 (Mg-2.96wt.%Al-0.87wt.%Zn-0.36wt.%Mn) sheet with a thickness of 6mm was utilized in this study and it will be referred to as 'as-received' material, hereafter. The specimens cut from the as-received sheet were subjected to annealing heat treatment at 420 ^{o}C for one hour. Specimens for microstructural examination were taken from the sheet thickness; i.e. the plane of rolling and sheet normal directions (RD-ND), and were prepared by conventional grinding and polishing and etched with acetic-picral. The microstructure was studied via optical microscopy.

The overall texture was evaluated by x-ray diffraction (XRD) using a Siemens D-500 diffractometer. Incomplete pole figures of $\{0001\}$, $\{10\bar{1}0\}$, and $\{10\bar{1}1\}$ were recorded, and the orientation distribution function (ODF) was constructed using TexTools, a texture analysis software. Recalculated pole figures were then derived from the ODFs. Pole figures of {0001} planes were constructed and compared to determine the effect of the treatment applied to the material. XRD specimens were ground successively to remove approximately 10% of the sheet thickness, polished with 1 μm diamond and then chemically polished in 10% nital solution for 120 seconds to eliminate any residual strain on the surface. Grain orientation was studied via electron-back scattered diffraction (EBSD) using a Hitachi S-3000 SEM at 20 kV and 70^{o} tilt angle. EBSD specimens, after polishing with 1 μm diamond slurry, were further polished with 0.05 μm colloidal silica and etched in a solution of 10 ml HNO_3, 30 ml acetic acid, 40 ml H_2O, and 120 ml ethanol for 10 seconds.

3.2.3 Results and Discussion

The microstructure and texture of the commercial AZ31-H24 sheet in both the as-received and annealed conditions are shown in Figs. 3.15a&b. The grain structure in both cases is non-uniform and twins are prominent in the as-received AZ31-H24. They both exhibit strong basal texture (Fig. 3.15c&d).

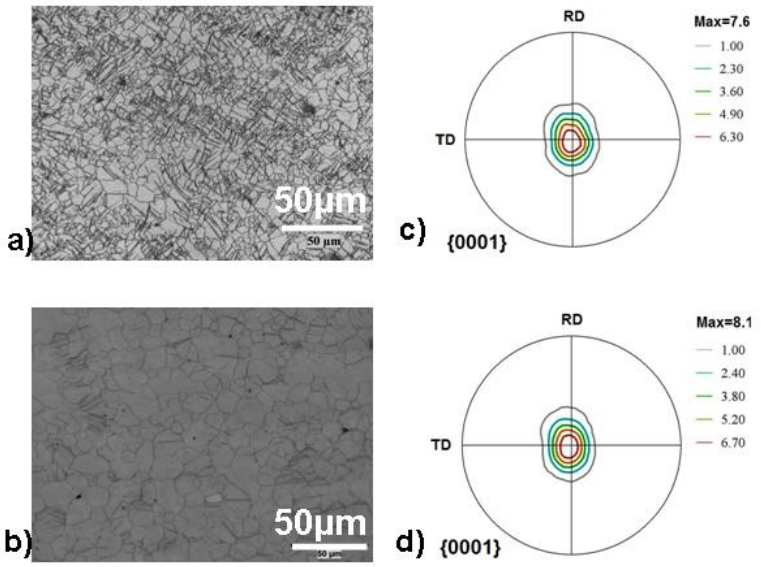

Fig. 3.15 Thickness microstructures (RD-ND plane) of commercial AZ31-H24 sheet; (a)before and (b) after annealing heat treatment at 420^{o}C for one hour. (c) and (d) {0001} pole figures corresponding to (a) and (b), respectively. RD and TD are the sheet rolling and transverse directions, respectively.

The as-received TRC sheet has a dendritic structure with coarse grains in the thickness (RD-ND plane) (Fig. 3.16a&b). Due to the high cooling rate and directional heat-transfer in the TRC process, columnar grains have grown against the heat-extraction direction where the solidifying material was in contact with the water-cooled casting rolls. In addition to the large grains, equiaxed grains (Fig. 3.16b) with an average size of 16μm are observed in the mid-thickness. SEM/EDS analysis of the TRC sheet detected Al, Zn, and Mn elements in the α-Mg matrix. Additionally, two different types of second phases were detected: (i) Mg, Al, and Zn, presumably $(Al,Zn)_{49}Mg_{32}$ phase [17], and (ii)Al-Mn

precipitates which are likely mixtures of $Al_{11}Mn_4$, Al_8Mn_5, Al_9Mn_{11} and β-Mn(Al) intermetallics [18]. The pole figures of the as-received TRC AZ31 (Fig. 3.16c) shows that most of the crystals are orientated with their basal {0001} planes parallel to the sheet surface (basal poles perpendicular to RD). The EBSD map of the plane of rolling and tranverse directions (RD-TD) (Fig. 3.16d) also agrees with the XRD pole figures and further shows that the large grains are mostly in basal orientation. There are also certain areas with non-basal orientation.

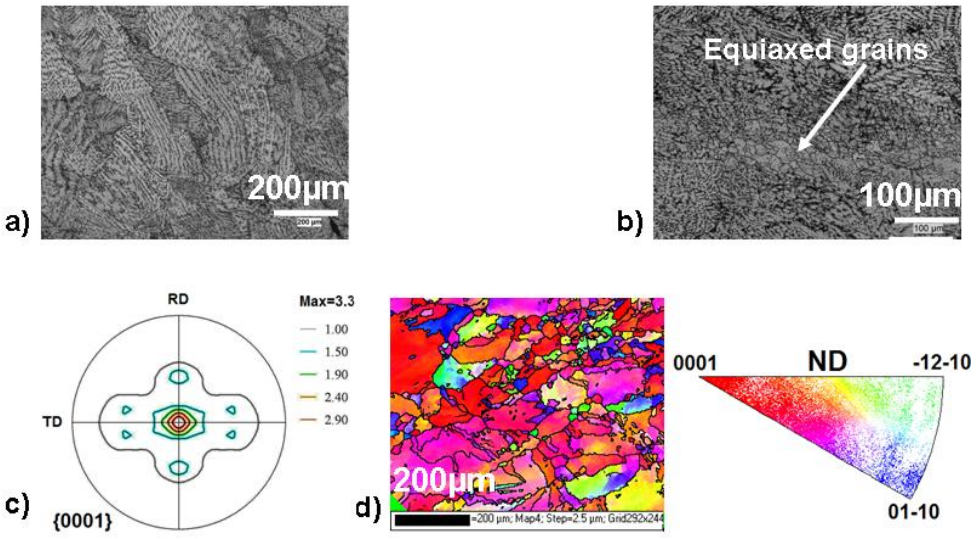

Fig. 3.16 RD-ND microstructure of the as-received TRC AZ31; (a) edge (b) mid-thickness. (c) {0001} pole figure and (d) EBSD map from RD-TD plane of the as-received TRC AZ31. ND is the sheet normal direction.

Figs. 3.17a&b show the effect of annealing heat treatment at 420 ^oC for an hour on the microstructure of the as-received TRC AZ31. Fine recrystallized grains are observed after the annealing heat treatment, indicating that the as-received TRC material had undergone plastic deformation before exiting the roll gap below 420 ^oC where no significant recrystallization was possible for the amount of strain accumulated. Nevertheless, the deformation temperature was high enough to prevent twin formation, as evidenced by the microstructures shown in Fig. 3.16. The large grains in Figs. 17a&b can be the remnants of large as-cast grains and the smaller ones are the recrystallized grains that exhibited grain growth during one hour heat treatment at 420 ^oC. Importantly,

annealing significantly changed the texture of the as-received TRC material, Fig. 3.17c. A certain degree of basal planes reorientation away from the sheet surface is observed, when compared to the as-received TRC pole figures (Fig. 3.16c). This is attributed to the recrystallization and nucleation of new grains at orientation angles different from the parent grains. The results are also supported by the EBSD analysis (Fig. 3.17d) which evidently shows that the majority of small grains have their basal poles away from the sheet ND (note that the cluster of reddish spots in the inverse pole figure is predominantly attributed to the two large grains covering about 35% of the analyzed surface (Fig. 3.17d)). Such texture has never been reported for AZ31 sheet produced by the conventional rolling process consisting of several rolling passes and intermediate annealing steps. The conventionally produced sheet has a strong basal texture which does not change by any annealing heat treatment (Figs. 3.15c&d).

It is known that, of the two mechanisms of recrystallization, grain-boundary bulging and sub-grain coalescence, the latter is expected to result in texture alteration [11]. Sub-grain formation occurs in regions of high dislocation density, such as twin boundaries or particle/matrix interfaces. Twins are not present in the TRC AZ31 strcture, however, comparing the microstructures in Figs. 3.15&3.17, it appears that the density of the second phases in the TRC AZ31 is much higher than that in the conventinal AZ31. It is to be noted that the TRC solidification process is the main factor leading to the higher volume fraction of second-phase particles. Non-equilibrium solidification in the TRC condition (cooling rate of ~10^2 K/s) follows the Scheil solidification model in which the back diffusion in the solid is limited and the solid-solubility limit is reduced. Consequently, the amount of second-phase particles increases as a result of the decrease in the matrix solid-solubility limit [19-21]. Second phases are common nucleation sites for new grains in pre-strained materials, i.e. particle-stimulated nucleation (PSN) of recrytallization. The deformation zones around the particles are of particular interest as they are the source of PSN and can have a significant influence on the recrystallized grain size and texture [11]. It is known that upon deformation via dislocation glide, if the particles do not deform or are not cut by dislocations, there is a local dislocation pile-up or looping at the particle/matrix interface which would lead to local bending of the crystal

due to uneven distribution of tensile and compressive strain fields [22]. Upon annealing, the dislocation pile-ups eventually lead to cell and sub-grain formation via recovery and, with the five degrees of freedom of sub-grain boundaries (tilt, twist and rotation), sub-grains coalesce to form nuclei for recrystallized grains [22]. Since such recrystallization is not due to grain-boundary bulging, which results in recrystallized grain orientations closely associated with the parent grains, the grain nuclei which form near the particles through sub-grain coalescence can take varying orientations leading to texture randomization.

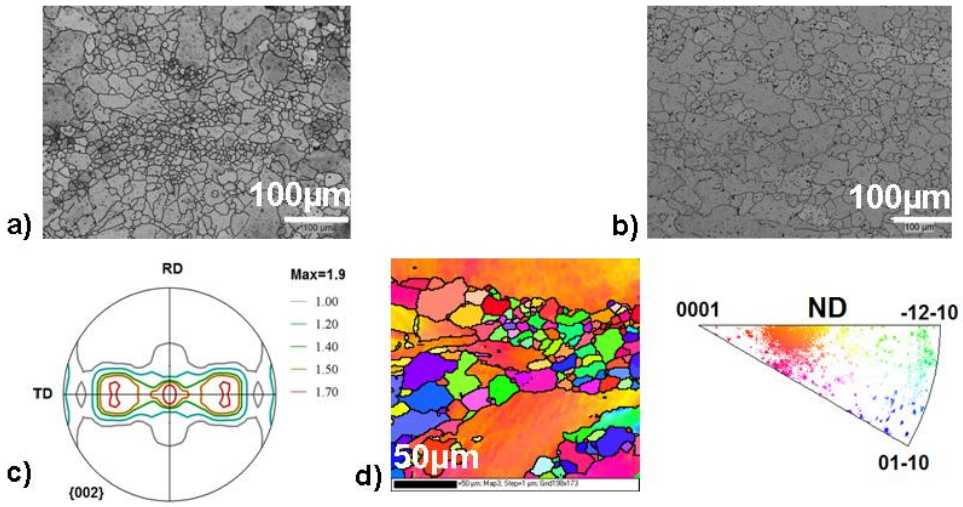

Fig. 3.17 Microstructures of the heat treated (one hour at 420 ^{o}C) TRC AZ31 in (a) edge and (b) mid-thickness. (c) {0001} pole figure of the heat treated TRC AZ31. (d) EBSD map of the RD-ND plane.

In order to verify the hypothesis that texture alteration in the TRC AZ31 could be due to the higher fraction of second phases, two new AZ31 alloys castings were produced; (i) a 4mm thick AZ31 plate cast in a vertical copper die at a cooling rate close to that observed during the TRC process and (ii) a cylinder with a diameter of 30 mm cast in a graphite die at a cooling rate close to that of the direct-chill (DC) ingot casting, i.e. 9.5 ^{o}C/s (the DC ingot is used in the conventional process of Mg sheet production) [23-24]. These are referred to as 'simulated TRC AZ31' and 'simulated DC AZ31," respectively. Samples from both castings were cold rolled ~15% with a 0.06 mm reduction per pass

and then annealed at 420 ^{o}C for 1 hour. The as-cast microstructures and {0001} pole figures of the cold rolled and the annealed specimens are shown in Fig. 3.18. The volume fraction and average particle size of the second-phase in the simulated TRC AZ31 were measured to be 0.12 and 1 μm, respectively, whereas, they are respectively 0.06 and 3 μm in the simulated DC AZ31. Figs. 3.18b&c indicate that the annealing does not change the basal texture which developed during the cold rolling of the simulated DC AZ31. On the other hand, the basal texture of the cold-rolled simulated TRC AZ31 was evidently changed by the annealing to a new arrangement of {0001} planes in which some of the basal planes are reoriented towards the TD, Figs. 3.18e&f. Consequently, it is concluded that the texture alteration in the heat treated TRC sheet can be attributed to the non-equilibrium solidification yielding a larger fraction of second phases which, in turn, enhances the PSN.

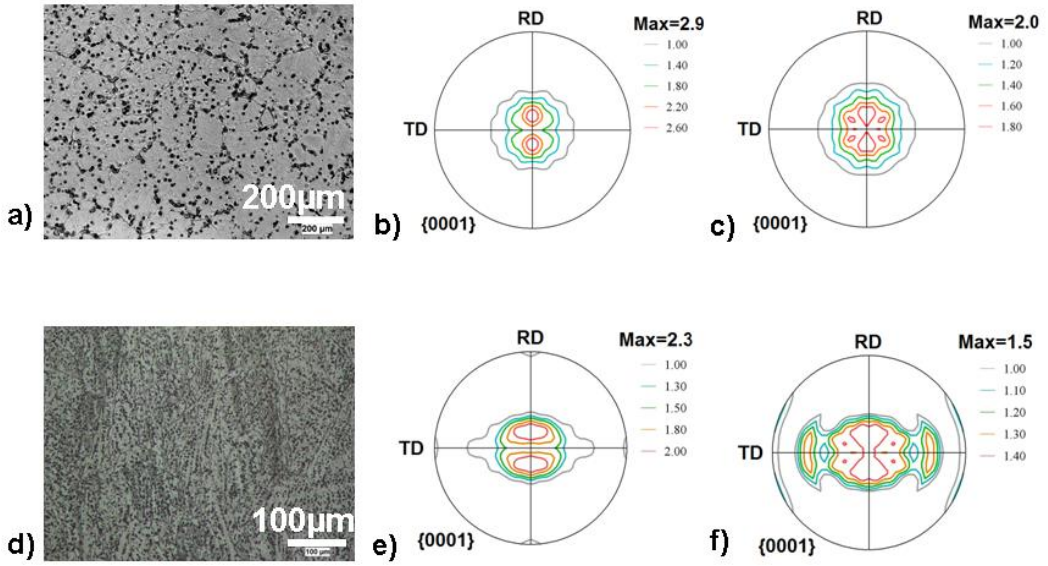

Fig. 3.18 Simulated DC AZ31: (a) as-cast microstructure, (b) cold-rolled {0001} pole figure, and (c) annealed {0001} pole figure. Simulated TRC AZ31: (d) as-cast thickness (RD-ND) microstructure, (e) cold-rolled {0001} pole figure, and (f) annealed {0001} pole figure.

Such alternation in the texture of Mg sheet is very important during the fabrication of sheet into automotive body components, especially those that can be

manufactured directly from the TRC AZ31 sheet and which require moderate temperature formability. Furthermore, an adequate formability and weakened texture is important in minimizing the number of subsequent rolling/annealing steps. Therefore, the weaker basal texture in the TRC AZ31 sheet obtained by the annealing treatment is a significant advance towards achieving low-cost Mg sheet with better formability which is attractive to the automotive industry.

3.2.4 References

1. I. H. Jung, W. Bang, I. J. Kim, H. I. Sung, W. J. Park, D. Choo, S. Ahn, Magnesium Technology, R. Beals, A. Luo, N.R. Neelameggham, M.O. Pekguleryuz, Eds, TMS, Warrendale, PA, 2007, pp. 85-88.
2. C. Yang, P. Ding, D. Zhang, F. Pan, Mater. Sci. Forum, 2005, pp. 427-430.
3. H. Watari, T. Haga, N. Koga, K. Davey, J. Mater. Process. Technol., 2007, 192-193, pp. 300-305.
4. D. Li, Q. Wang, W. Ding, Mater. Sci. Forum. , 2007. 546-549(1), pp. 311-314.
5. S. H. Kim, B. S. You, C. D. Yim, Y. M. Seo, Mater. Letters, 2005. 59, pp. 3876 – 3880.
6. A. Jager, P. Lukac, V. Gartnerova, J. Haloda, M. Dopita, Mat. Sci. Eng. A, 2006, 432, pp. 20–25.
7. F. B. Kaiser, D. Letzig, K. U. Kainer, A. Sfyczynski, C. Hartig, Adv.Eng. Mater., 2003. 5(12): pp. 891-896.
8. M. R. Barnett, M. D. Navea, C. J. Bettlesb, Mater. Sci. Eng. A, 2004, 386, pp. 205–211.
9. H. T. Jeong, T. K. H., J.Mater. Process. Technol., 2007, 187–188, pp. 559–561.
10. F. B. Kaiser, D. Letzig, J. Bohlen, A. Styczynski, C. Hartig, K. U. Kainer, Mater. Sci. Forum, 2003. 419-422 (Part1), pp. 315-320.
11. F. J. Humphreys, M. Hatherly, 2 ed. 2004: Great Britain by Galliard Ltd., UK.
12. R. K. Mishra, A. K. Gupta, P. R. Rao, A. K. Sachdev, A. M. Kumar and A. A. Luo, Script. Mater., 2008, 59(5), pp. 562-565.

13. J. Bohlen, M. R. Nurnberg, J. W. Senn, D. Letzig, S. R. Agnew, Acta Mater., 2007, 55(6), pp.2101-2112.
14. N. Stanford, M. Barnett, Script. Mater., 2008. 58(3), pp. 179-182.
15. L. W. F. Mackenzie, M. O. Pekguleryuz, Script. Mater., 2008, 59(6), pp. 665-668.
16. L.W.F. Mackenzie, M. Pekguleryuz, Mat. Sci. Eng A, vol. 480(1-2), 2008, pp. 189-197.
17. "Metallography and Microstructures," ed. Vander Voort G. F. Vol. 9. 2004: Materials Park, OH: ASM International
18. P. Cao, D. H. StJohn, M. Qian, Mater. Sci. Forum, 2005. 488-489:p p. 139-142.
19. J. A. Sarreal, G. J. Abbaschian, Metall. Trans. A., Nov. 1986. 17A(11): pp. 2063-2073.
20. M. Masoumi, M. Pekguleryuz, Trans. AFS, 2009. 117: pp. 617-626
21. B. Dutta, , M. Rettenmayr, Mat. Sci. and Tech. (UK). , Dec. 2002. 18(12): pp. 1428-1434
22. R. E. Reed-Hill, R. Abbaschian, Third ed., 20 Park Plaza, Boston, MA: PWS.
23. S. S., Park, , J. G., Lee, , H. C., Lee, , N. J. Kim, , Magnesium Technology, A. Luo, ed, TMS, Charlotte, NC, 2004. pp. 107-112.
24. Y. Nakaura, K. Ohori, Mater. Sci. Forum, 2005. pp. 419-426.

3.3 Microstructure and Texture Studies on Twin-Roll Cast AZ31 (Mg-3wt%Al-1wt%Zn) Alloy and the Effect of Thermomechanical Processing*

*This section has been published**: M. Masoumi,** F. Zarandi, M. Pekguleryuz, "Microstructure and Texture Studies on Twin-Roll Cast AZ31 (Mg-3wt%Al-1wt%Zn) Alloy and the Effect of Thermomechanical Processing" Mat. Sci. Eng. A, Vol. 528, no 3, 25 Jan. 2011, pp. 1268-1279.

The microstructure and texture of the twin-roll cast (TRC) AZ31 (Mg-3wt.%Al-1wt.%Zn) sheet, with a thickness of 6mm, have been investigated. The TRC AZ31 exhibits a dendritic microstructure with columnar and equiaxed grains. These contain Al-Mn and Mg-Al-Zn second-phase particles that are approximately 1μm in size. This heterogeneous structure is attributed to the effect of the cooling rate, which varies from 325 ^{o}C/s on the surface to ~150 ^{o}C/s in the mid-thickness of the sheet. No surface segregation, but a certain degree of macrosegregation is observed in the mid-thickness which persists after annealing and rolling. Recrystallization at 420 ^{o}C leads to a bimodal grain-size distribution, while a fine-grain structure is obtained after rolling and annealing. The TRC AZ31 sheet exhibits basal textures in the (i) as-received, (ii) rolled and (iii) rolled-annealed conditions. However, post-annealing of the TRC AZ31 at 420 ^{o}C produces a relatively random texture that has not been previously observed in the conventional AZ31 sheet. The texture randomization is attributed to the particle-stimulated nucleation of new grains in the TRC structure. The preliminary evaluation of mechanical properties indicates that such annealing treatment slightly increases the ultimate tensile strength (UTS), but significantly improves elongation.

3.3.1 Introduction and Background

Automotive applications of Mg alloys have received significant attention for vehicle weight-reduction. To date, the application of Mg alloys in cars has been mostly limited to die-cast parts, such as steering-wheel cores, engine-head covers, disk wheels, brake-pedal brackets, instrument panel, seat frames, transmission cases and engine block [1-4]. The use of Mg in the automotive body has a great potential for allowing further weight

reduction. Recently, the interest in the use of Mg for automotive-body applications has highlighted the importance of a cost-effective Mg sheet [5-7]. Mg sheet production by means of the conventional process, which comprises direct-chill (DC) casting of an ingot and its subsequent hot and cold-rolling steps, is relatively costly [5]. However, the cost can be reduced via near-net shape casting processes such as thin slab casting, single-belt casting and twin-roll casting (TRC) [8]. The TRC produces the thinnest as-cast sheet (with thickness less than 6 mm) [9] and is the most economical process, with investment costs that are 1/3 to 1/4 of the conventional Mg sheet production process [10-12].

The AZ31 (Mg-3wt.%Al-1wt.%Zn), the most common Mg sheet alloy, is currently produced by hot rolling of the DC cast ingot. The hot-rolled sheet, designated as AZ31-H24, exhibits a non-uniform grain size [13-16], while the sheet rolled at lower temperatures is prone to extensive twining [14]. Rolling orients the {0001} basal planes of the hexagonal closed packed (HCP) Mg crystals parallel to the sheet surface with the $[10\bar{1}0]$ axis in the rolling direction [13, 15-19], leading to a preferred orientation known as basal texture. Hot rolling produces a perfect basal texture, while the warm-rolled sheet exhibits an egg-shaped distribution of {0001} planes in the pole figure [13, 15-19]. A gradient of basal texture intensities from the surface to the center of the sheet has been reported in the asymmetrically hot-rolled sheet [13]. All these characteristics adversely affect formability and, as a consequence, considerably limit the variety of automotive body parts which can be made from Mg sheet [20].

Despite the interest in TRC AZ31, which is available on a limited scale globally, very little information exists on its microstructure and texture. The TRC that combines casting and *in situ* warm rolling produces a unique combination of cast and deformed structure. The structure of the TRC AZ31 sheet consists of a chilled-zone close to the sheet surface, followed by columnar-grains formed as a result of directional solidification [5, 21-25]. Equiaxed grains observed in the central region of the TRC sheet can be attributed to constitutional undercooling. Kawala *et al.* [26] have reported a texture gradient from the central region to the near-surface layers of the TRC sheet. Since strain is accumulated in the columnar grains during the *in situ* rolling of the TRC process, Park

et al. [21] have observed that subsequent annealing transforms the large columnar grains into fine equiaxed grains. A reduction in the centerline segregation has been also reported as a result of annealing [5]. Fine equiaxed grains with an average size of 6 μm are produced via TRC followed by warm rolling and annealing [5, 21-22, 24, 27]. Recently, the present authors have observed texture alteration upon post-annealing of the TRC sheet [25]. This phenomena warrants further study.

This paper studies the effects of annealing and thermomechanical processing on the microstructure and texture of the TRC AZ31 sheet produced on a commercial scale. This is part of a larger investigation which aims at optimizing the thermomechanical processing of TRC AZ31 for automotive applications and at developing alternative Mg alloys for the TRC process [28-29].

3.3.2 Experimental Procedure

A TRC AZ31 sheet with a thickness of 6mm and chemical composition of Mg-2.96wt.%Al-0.87wt.%Zn-0.36wt.%Mn was investigated. For comparison, a commercial AZ31-H24 sheet produced by DC casting and hot rolling was also included in the study. Specimens from both materials were heat-treated at 420 ^{o}C for 1 hour and the resulting microstructures and textures were compared. Subsequently, a laboratory-scale Stanat rolling mill was used to reduce the thickness of the heat-treated TRC sheet to 1.4 mm through seven rolling passes, with equal reduction of about 0.65 mm in each pass. The total reduction ratio was 0.75. The samples were preheated for 15 minutes at 400 ^{o}C before the first rolling pass and for 5 minutes before the subsequent passes. The specimen was finally annealed at 400 ^{o}C for 5 minutes after the last rolling pass.

In order to determine the unique effects of the TRC process (fast cooling combined with warm rolling) on the texture of TRC AZ31, a permanent-mould cast AZ31 plate was produced in the laboratory. This casting is referred to as ‘quasi-TRC plate,’ hereafter ‘quasi’ (since no rolling deformation was involved). The AZ31B alloy (supplied by Timminco, now Applied Magnesium) was melted in a graphite crucible using a NORAX induction furnace under a gas mixture of sulphur hexafluoride (SF_6) and carbon dioxide (CO_2). A plate with a thickness of 4 mm was cast at 720 ^{o}C into a vertical copper die and

at a cooling rate close to that experienced during the TRC process, i.e., ~185 ^{o}C/s [21, 23, 27].

Specimens for microstructural examination were taken from the thickness (the plane of rolling and sheet normal directions (RD-ND)), in the cases of TRC AZ31 and commercial AZ31-H24. They were prepared by grinding on SiC abrasive papers, polished with diamond paste and etched in acetic-picral. The microstructure was studied via optical and scanning electron microscopy (SEM). Secondary dendrite arm spacing (SDAS) was measured using the mean-intercept method. X-ray elemental distribution was obtained in a JEOL 8900 electron probe micro-analysis (EPMA) SEM with a resolution of 70 nm. The substructure was studied in a Philips CM200 transmission electron microscope (TEM) at 200 kV. The TEM samples were jet-polished, using a solution of 5% perchloric acid, 35% butanol and 60% ethanol.

Mechanical properties were evaluated via tensile testing (ASTM B557) at an ambient temperature, using specimens of 25mm×6mm×6mm (gage length×width×thickness). The tensile specimens were machined from the TRC sheet in both the rolling and transverse directions. The tensile tests were performed at Westmorland Labs at an initial strain rate of 5×10^{-3} s^{-1}. The offset yield strength (YS), ultimate tensile strength (UTS), elongation to failure (E_f), and n-value were determined based on the average of three tests.

The overall crystallographic orientation was evaluated via x-ray diffraction (XRD), using a Siemens D-500 x-ray diffractometer. Incomplete pole figures of {0001}, $\{10\bar{1}0\}$ and $\{10\bar{1}1\}$ were recorded, and the orientation distribution function (ODF) was constructed using TextTools texture-analysis software. Recalculated pole figures were derived from the ODFs. The XRD specimens were ground successively to remove almost 10% of the sheet thickness and then polished with 1 μm diamond slurry. They were then chemically polished in 10% nital solution for 120 seconds to eliminate any residual stress on the surface. The grain orientation was also studied using the electron back scattered diffraction (EBSD) method in a SEM at a 20 kV accelerating voltage and a 70^{o} tilt angle. After being polished with 1 μm diamond slurry, the EBSD specimens were further

polished using 0.05 μm colloidal-silica, and were etched in a solution of 10 ml HNO_3, 30 ml acetic acid, 40 ml H_2O and 120 ml ethanol for about 10 seconds.

3.3.3 Results and Discussion

3.3.3.1 Microstructure and texture of commercial AZ31-H24 sheet

The microstructure of the as-received AZ31-H24 sheet contains numerous twins (Fig. 3.19a). The texture is strongly basal, with the basal planes inclined toward the sheet surface (Fig. 3.19b). Such preferred orientation develops in Mg during plastic deformation because the slip occurs mainly on the basal planes, leading to their alignment parallel to the metal flow direction [30]. New recrystallized grains are observed after annealing at 420 ^{o}C (Fig. 3.19c). However, the strong basal texture still persists, as evidenced by the pole figure in Fig. 3.19d, which indicates that the mechanisms of recrystallization in the AZ31-H24 are likely to be grain-boundary (GB) bulging and/or twin-induced recrystallization. It is known that the GB bulging mechanism results in annealing textures that are quite similar to the deformation texture. Galiyev *et al.* [31], who studied twin-induced recrystallization, showed that high dislocation density near twin boundaries restructures into low energy dislocation structures and nucleates fine recrystallized grains through progressive lattice rotation. These new grains are limited to the twin areas and do not extend into the matrix, so that the final texture is not significantly affected [32].

3.3.3.2 TRC AZ31

Grain structure

The TRC AZ31 sheet in the as-received condition has a dendritic structure (Fig. 3.20). Due to the high cooling rate and directional heat transfer, large columnar grains have grown against the heat extraction direction where the solidifying material has been in contact with the cold casting rolls. In contrast to the results found by Nakaura *et al.* [22], no bleeding was observed below the sheet surface. Equiaxed grains (Fig. 3.20b), with an average grain size of 16 μm, are also observed in the mid-thickness. The formation of such equiaxed grains can be attributed to the constitutional undercooling that causes a

transition from columnar- to equiaxed-grains during solidification [33]. On the other hand, very small grains are present along certain grain boundaries, both near the edge and the mid-thickness of the sheet (Fig. 3.21). These are likely dynamically recrystallized grains that have formed as a result of warm rolling during twin roll casting. Due to the rapid cooling rate associated with the TRC process, these grains have remained small since there was very limited time for grain growth.

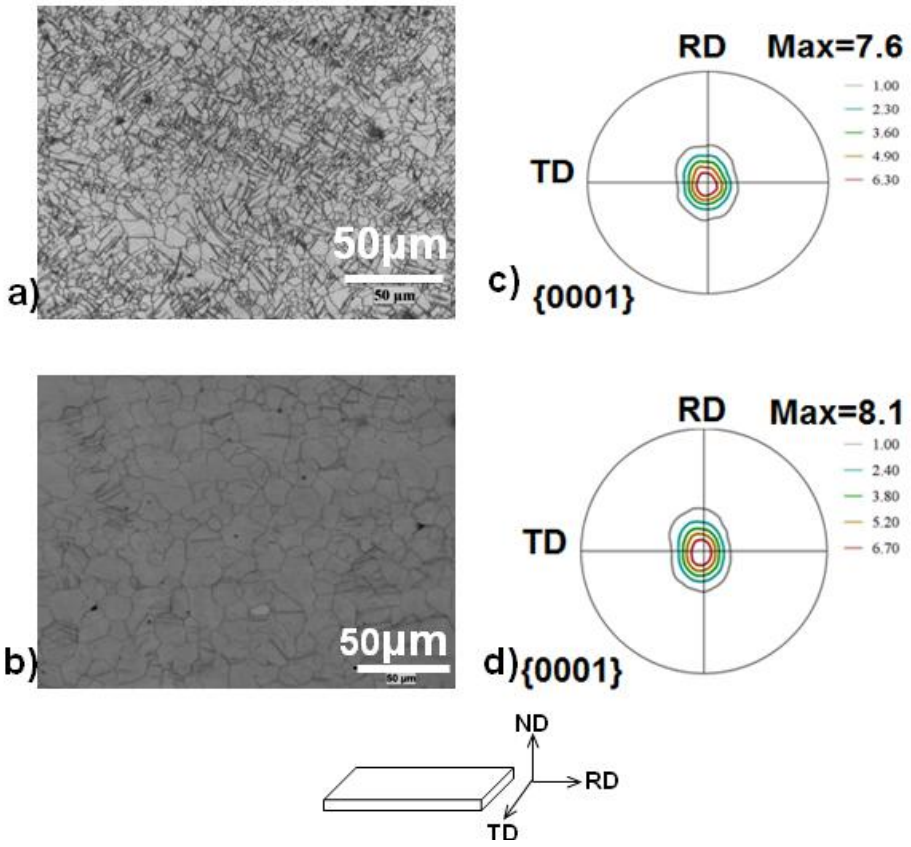

Fig. 3.19:Thickness microstructures (RD-ND plane) of commercial AZ31-H24 sheet; (a)before and (b) after annealing heat treatment at 420^{o}C for one hour. (c) and (d) {0001} pole figures corresponding to (a) and (b), respectively. RD and TD are the sheet rolling and transverse directions, respectively.

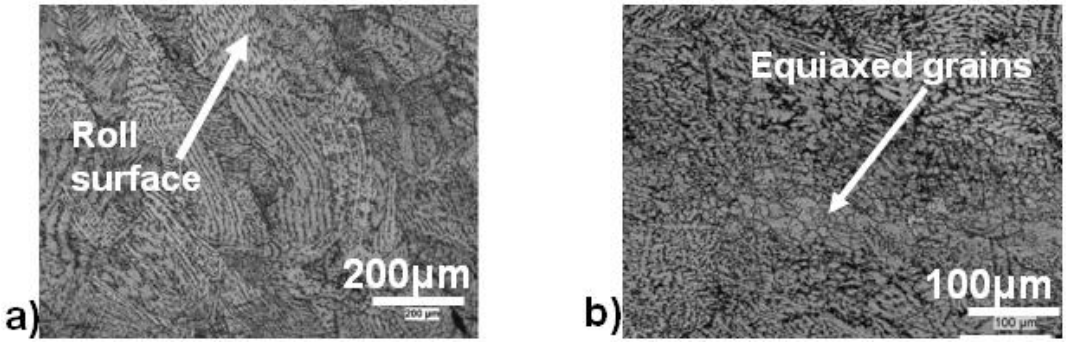

Fig. 3.20 Thickness (RD-ND) microstructure of the as-received TRC sheet; (a) edge region exhibiting the columnar grains grown almost normal to the sheet surface, and (b)mid-thickness showing the dendritic structure with equiaxed grains in the middle.

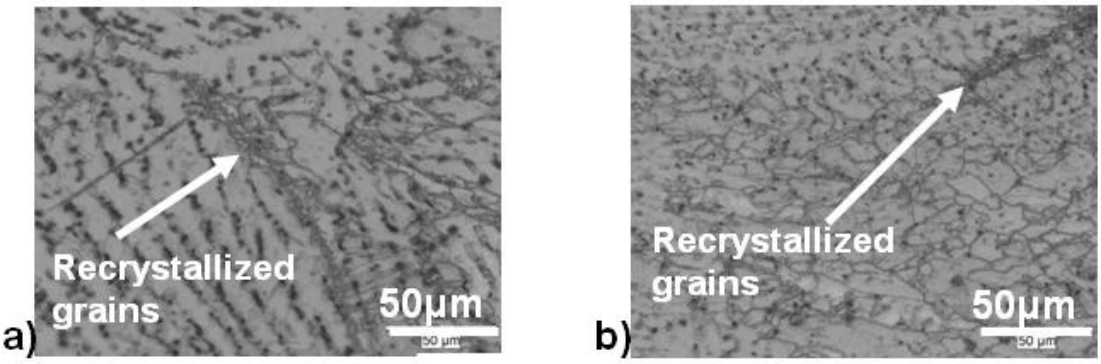

Fig. 3.21 Small equiaxed grains in the as-received TRC AZ31 sheet; (a) edge,(b) mid-thickness.

Microstructure and the effect of cooling rate

The solidification rate has a great influence on the microstructure and hence on the mechanical properties of alloys. Even though this effect is more pronounced when casting is the final product, wrought products can also be affected by the original as-cast structure. In wrought alloys, the solidification structure and the related defects are difficult to eliminate once they have been created. They also influence the deformation structures. Therefore, the control of the solidification process often becomes vitally important in terms of product quality [34]. Dendrite arm spacing measurement is one of the most common methods used to study solidification structures [33]. An increase in the solidification rate results in a reduction in the dendrite arm spacing and in an

improvement in the mechanical properties. The ductility and the tensile strength are the properties that are most influenced by the cooling rate [33].

The cooling rate (CR) experienced in the TRC AZ31 sheet was estimated by measuring SDAS and by using the equation $SDAS\ (\mu m) = 85.15(CR)^{-0.42}$ [35]. The average SDAS values in the as-received TRC sheet are 7.5 μm and 10.3 μm, near the edge and in the mid-thickness, respectively. Accordingly, the respective cooling rates are determined as 325 ^{o}C/s and 152 ^{o}C/s. SDAS values of 3-6.5 μm have been previously reported for the TRC AZ31 sheet. Cooling rates of 556-130 ^{o}C/s have been determined for these SDAS values using an equation developed for the AZ91 (Mg-9wt%Al-1wt%Zn) alloy [21, 23, 27]. These SDAS values are significantly smaller and the cooling rates are much higher than those commonly seen in DC casting (SDAS of 34 μm and cooling rate of 10 ^{o}C/s [21-22, 27]).

The SEM micrographs of the as-received TRC AZ31 sheet show fine second-phase particles dispersed evenly in the matrix (Fig. 3.22a). However, it is also noted that a surface layer of about 150-200 μm in the sheet is impoverished in second phases (Fig. 3.22b). These features can be explained via the effects of cooling rate. It is known that at a very low CR (close to the equilibrium condition), the solute can diffuse from the liquid/solid interface back into the solid phase and that the amount of the eutectic phases is close to the equilibrium fraction (f_{sp}) obtained by the lever rule. On the other hand, at rapid solidification rates (>200 ^{o}C/s), the eutectic transformation is restricted; "solute engulfing" produces a supersaturated single-phase solid solution (α-Mg) and f_{sp} is thus much reduced. Between these two conditions, the Scheil non-equilibrium solidification mode prevails, where back-diffusion of the solute into the solid is limited (formation of an "undersaturated" solid-solution); solute rejection into the liquid is high, leading to a higher amount of second phase than that of equilibrium condition [35-36]. The TRC AZ31 in the as-received condition exhibits a dual-mode of non-equilibrium freezing: (i) rapid solidification at the surface (to a depth of 200 μm), which results in second-phase depletion, and (ii) Scheil solidification in the majority of the sheet thickness, resulting in f_{sp} that is larger than the equilibrium amount. The area fraction of the second phases, f_{sp},

is 0.12 in the TRC AZ31 sheet, compared to 0.06 usually observed in a DC cast ingot [25].

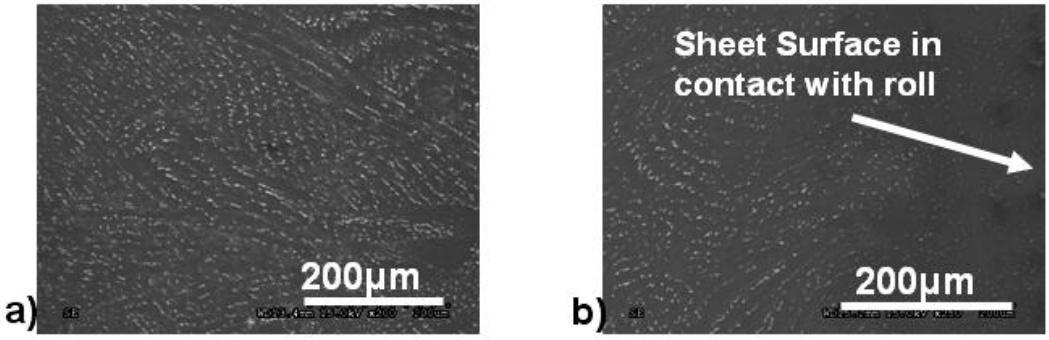

Fig. 3.22 Distribution of second phases in the as-received TRC AZ31 sheet; (a) away from the sheet surface and (b) close to the sheet surface.

The average size of second-phase particles in the as-received TRC AZ31 is 1 μm, compared to 2.75 μm in the DC casting [25]. The EDS analysis of the TRC sheet indicates that the α-Mg matrix comprises Mg, Al, Zn, and Mn elements (Fig. 3.23). Two types of second phases are observed: the one composed of Mg, Al, and Zn is presumably the $(Al,Zn)_{49}Mg_{32}$ phase [37], and the other type, which is composed of Al and Mn, could be a mixture of $Al_{11}Mn_4$, Al_8Mn_5, Al_9Mn_{11} and β-Mn(Al) intermetallics [38]. The EPMA analysis of the region close to the sheet surface did not reveal any segregation, i.e., no inverse segregation was observed in this TRC sheet. However, some centerline segregation, rich in Al and Zn and with a distribution of relatively coarse Al-Mn intermetallics, was present (Fig. 3.24). This result is in agreement with the observations made by Nukaura *et al.* [22-23]. Park *et al.* [21], on the other hand, did not report any noticeable macrosegregation through the thickness of TRC AZ31. The mid-thickness segregation can be attributed to non-equilibrium solidification as well as to the rolling deformation. The latter could also contribute to such segregation through backward squeezing of the solute-rich liquid metal towards the liquid metal sump. The TEM results show that dislocation accumulation exists around the second phases in the as-received TRC AZ31 (Fig. 3.25a). Moreover, nanosize particles evenly distributed in the matrix were observed (Fig. 3.25b). These particles could not be analyzed via EDS. They could

be Mn-Al particles that formed in the liquid metal [39] and that did not have enough time to grow, due to the high cooling rate of twin-roll-casting.

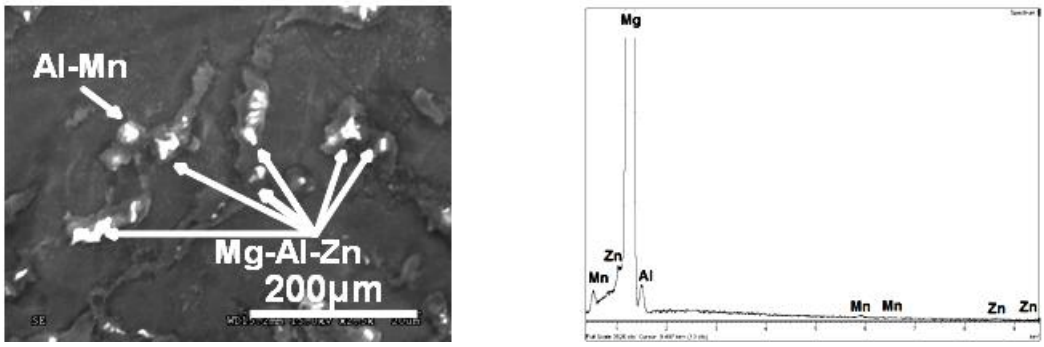

Fig. 3.23 SEM micrograph showing the second phase particles and EDS spectrum of the matrix in the as-received TRC AZ31 sheet.

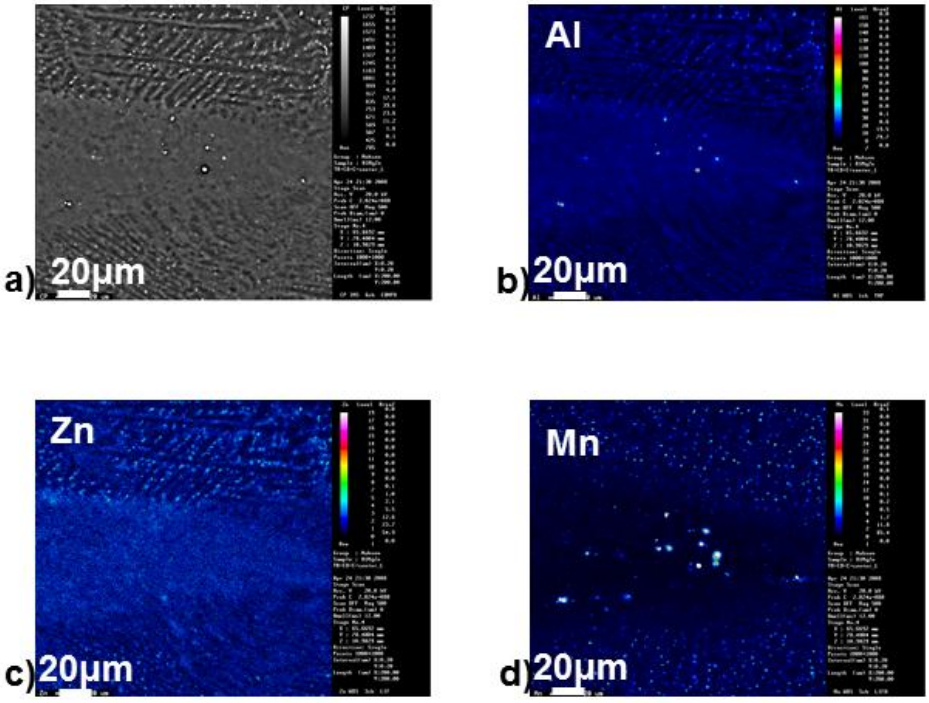

Figure 3.24 (a) Centerline segregation in the as-received TRC AZ31 and EPMA micrographs of (b) Al, (c) Zn, and (d) Mn (The region with higher element percentage appears brighter).

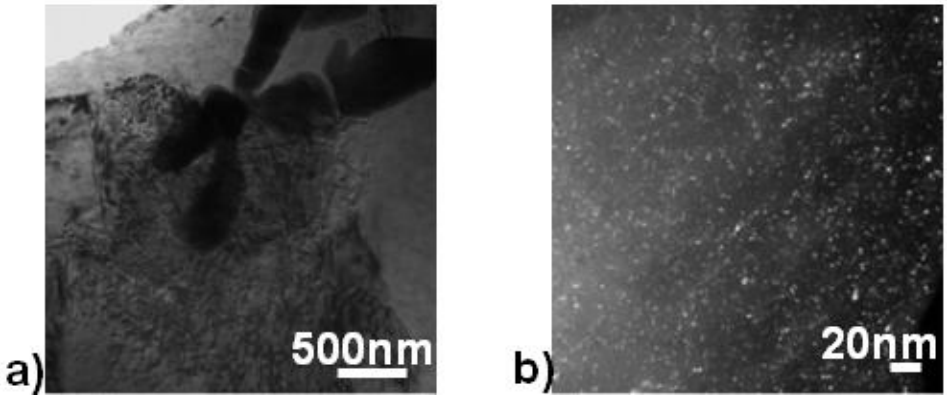

Fig. 3.25 TEM observations on the as–received TRC AZ31 sheet (a) dislocation pile-up around the second phase particles (b) nano-size particles.

Texture

Fig. 3.26a shows the XRD pole figures obtained from the surface (RD-TD plane) of the as-received TRC AZ31. The majority of the grains are orientated with their basal planes {0001} nearly parallel to the sheet surface (basal texture). This is similar to the texture of the commercial AZ31-H24 sheet, where a strong basal texture prevails on the sheet surface. A similar basal texture is observed in the mid-thickness of the TRC AZ31 (Fig. 3.26b). As is known, in HCP Mg, the basal <a> dislocation constitutes the most active slip system and its operation during rolling deformation rapidly orients the basal planes parallel to the sheet surface.

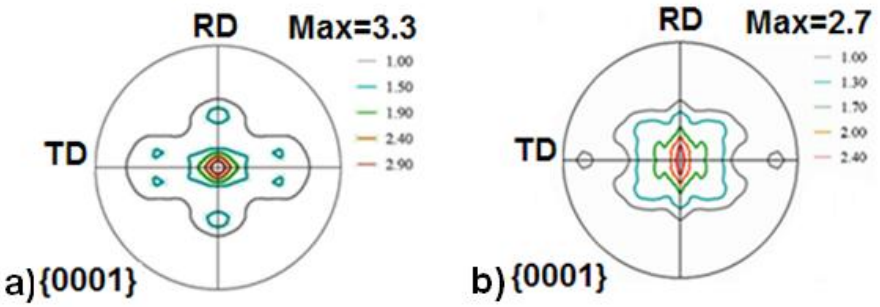

Fig. 3.26 Pole figure from the as-received TRC AZ31 sheet; (a) surface, (b) mid-thickness.

The basal texture observed in the as-received TRC AZ31 sheet can either be a deformation texture (due to the rolling associated with the TRC process) or a casting texture (due to the directional growth of columnar grains). In order to verify this, the microstructure and texture of the quasi-TRC plate (cast at the TRC cooling rate but with no rolling deformation) were studied. The quasi-TRC AZ31 (thickness plane) comprises columnar grains grown against the die surface (Fig. 3.27a), which are similar to those of the as-received TRC AZ31 (Fig. 3.20). The SDAS is ~9.5 μm, which corresponds to the range of the cooling rates experienced in the TRC process. In contrast to the TRC AZ31, the quasi-TRC plate has the prismatic planes $\{1\bar{1}00\}$, and not the basal planes {0001} inclined towards the plate surface, as illustrated in the pole figures in Fig. 3.27b. Since no rolling deformation was associated with the production of the quasi-TRC plate, it is inferred that the development of basal texture in the as-received TRC AZ31 is a result of the *in situ* rolling deformation applied by the casting rolls.

The EBSD observations (Fig. 3.28) concur with the XRD results and further indicate that the large grains are mostly in the basal orientation, while the smaller grains tend to have random orientation in the as-received TRC AZ31. Fig. 3.29 shows that there are also fine grains close to the sheet surface that possess a random orientation. Jung *et al.* [5] characterized these small grains as chill (cast) grains. Although this may seem reasonable since they formed near the edge, the fact that they have a random orientation suggests otherwise. If they were chilled grains, they would have basal orientation as a result of rolling deformation following the solidification. But, their random orientation indicates that they are new recrystallized grains. Similarly, the fine equiaxed grains in the mid-thickness exhibit a random texture (Fig. 3.30). Since these grains are formed in the last stage of solidification (in a region of segregation and constitutional undercooling), they undergo much less deformation, if any, than those close to the sheet surface during the TRC process. Hence, they are unlikely to be a result of recrystallization. This is also in line with the macro-texture analysis, which indicates that the texture intensity in the mid-thickness of the sheet is lower than that close to the sheet surface.

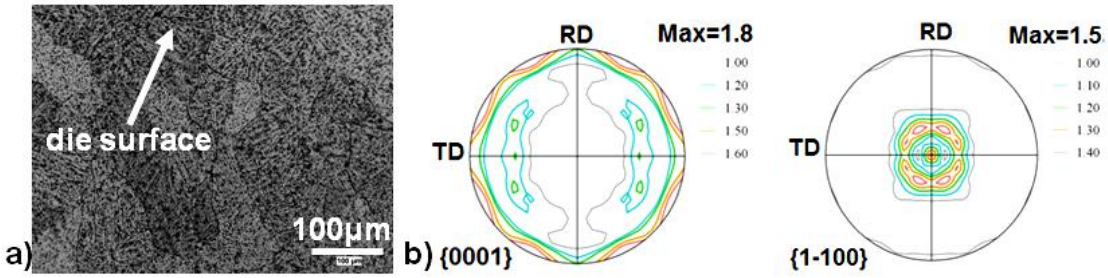

Figure 3.27 The Quasi-TRC plate; a) thickness microstructure, b) surface texture (heat transfer axis is parallel to ND in this figure and RD-TD plane is the plate surface).

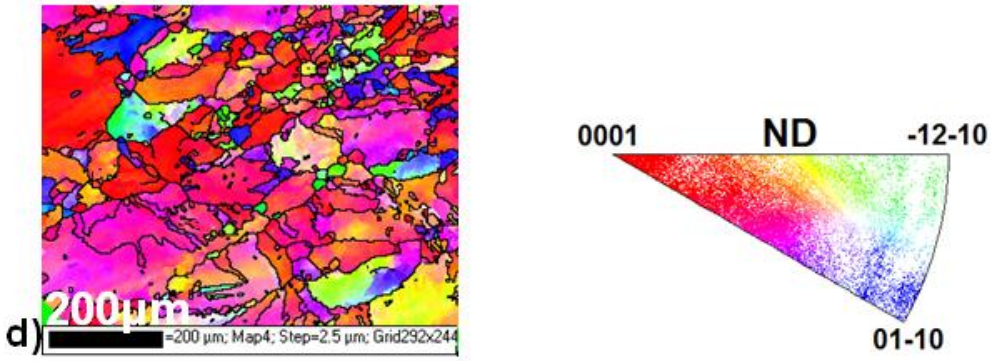

Fig. 3.28 EBSD map from the RD-TD plane of the as-received TRC AZ31 sheet.

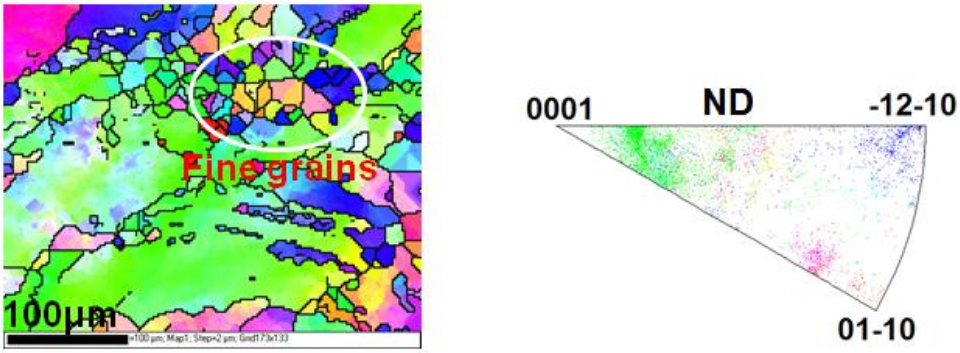

Fig. 3.29 EBSD map from the RD-ND plane of the as-received TRC AZ31 sheet (close to the edge).

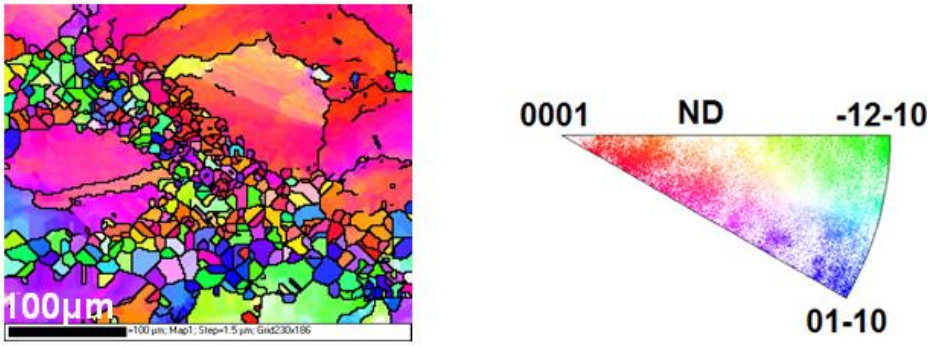

Fig. 3.30 EBSD map from the RD-ND plane of the as-received TRC AZ31 sheet (mid-thickness).

3.3.3.3 Thermomechanically Treated TRC AZ31

Three types of thermo-mechanical treatment were applied to the as-received TRC AZ31: (i) annealing at different times (from 3 minutes to 1 hour) and temperatures (from 350 ^{o}C to 420 ^{o}C), (ii) hot-rolling at 400 ^{o}C and (iii) rolling at 400 ^{o}C with a subsequent anneal at 400 ^{o}C. These temperatures were selected because they are typical of the industrial hot-rolling practice [40].

Annealed TRC AZ31

Because of the combined cast/rolled structure of twin-roll casting, annealing has an important effect on the microstructure of the as-received TRC AZ31: annealing for one hour at 420 ^{o}C produces a recrystallized structure (Fig. 3.31). Given that the kinetics of recrystallization in Mg are fast, the absence of such a recrystallized structure in the as-received TRC suggests that the sheet exited the roll gap at a temperature below 420 ^{o}C. At this temperature, no significant recrystallization was possible in a short time for the amount of strain accumulated. However, the deformation temperature was apparently high enough to prevent extensive twining, as evidenced by the microstructures shown in Fig. 3.20. The very large grains seen in Fig. 3.31 are the remnants of large as-cast grains and the smaller ones are the recrystallized grains. The material also homogenized simultaneously and the dendritic coring was eliminated. Nevertheless, the EPMA indicated that the centerline macrosegregation was still present.

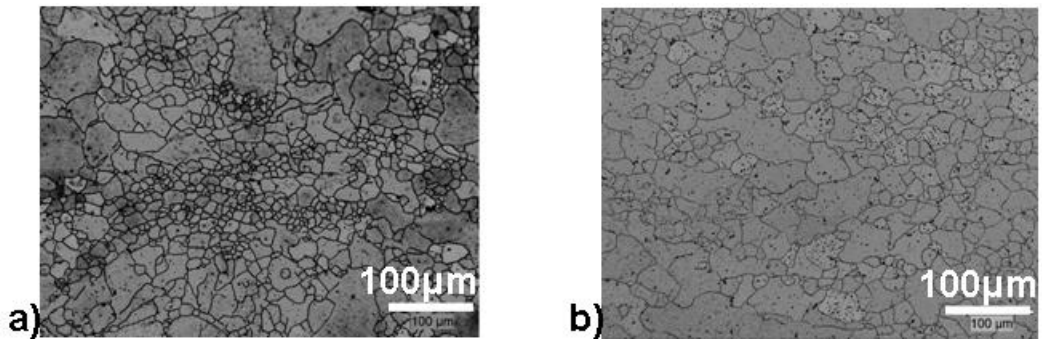

Fig. 3.31 The thickness microstructure of the TRC AZ31 sheet after 1 hr at 420 ^{o}C; (a) edge and (b) mid-thickness.

Most importantly, the recrystallized TRC sheet exhibits a texture alteration: Fig. 3.32a (compared to Fig. 3.26) shows that some of the basal planes are reoriented away from the sheet surface (with a split in the basal poles towards TD) as a result of annealing. The basal pole splitting due to annealing has not been previously observed in AZ31 sheet. A similar treatment applied to the commercial AZ31-H24 sheet produces a recrystallized structure nearly identical to that seen in the annealed TRC AZ31 but with no texture change (Fig. 3.19d). The EBSD (Fig. 3.32b) shows that the small recrystallized grains exhibit orientations different from the large parent grains; they have various orientations with their basal poles deviating from the sheet normal direction (ND). Note that the cluster of reddish spots in the inverse pole figure is predominantly attributed to the two large grains covering about one third of the analyzed surface (Fig. 3.32b).

In order to study the evolution of the microstructure and texture during annealing, the as-received TRC AZ31 sheet was annealed for different times and at different temperatures. The microstructures and textures analyses after annealing for 3, 5 and 20 minutes at 420 ^{o}C (Figs. 3.33) show that the recrystallization starts at an early stage with the nucleation of very fine grains that grow with time, while the amount of second phases decreases as the microstructure approaches its equilibrium state. It is observed that the change in texture begins at early stages of annealing, which confirms that the nucleation and growth of new grains are responsible for texture alteration.

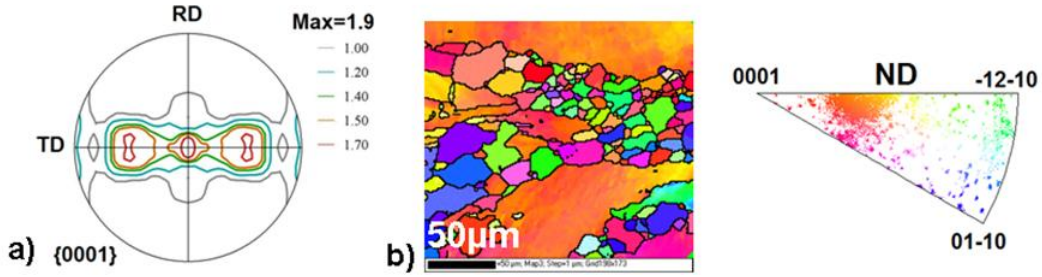

Fig. 3.32 TRC AZ31 sheet after 1 hr at 420°C; (a) surface pole figure and (b) EBSD map on the RD-ND plane.

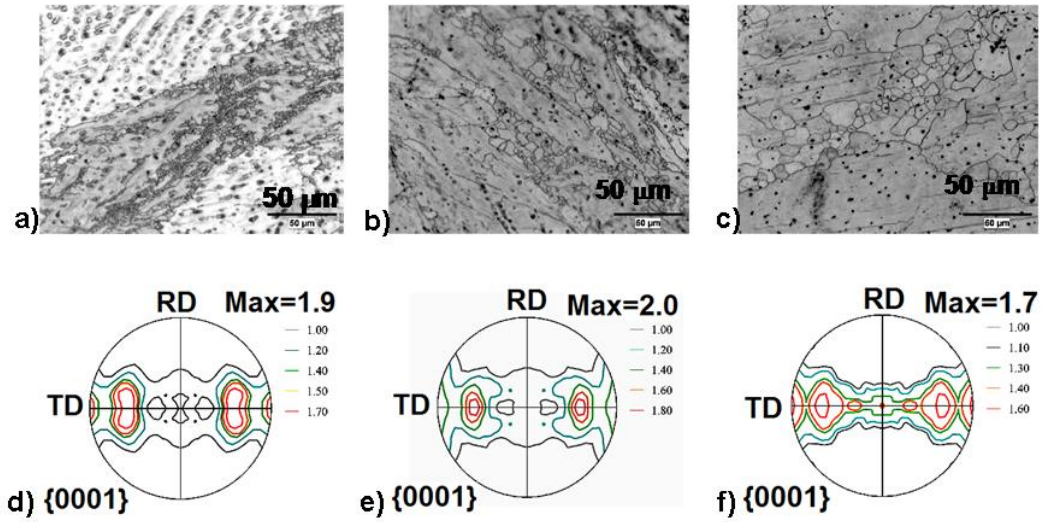

Fig. 3.33 (a-c) Microstructures and (d-f) corresponding surface texture pole figures of the as-received TRC AZ31 sheet annealed at 420 °C for 3, 5 and 20 min, respectively.

The effect of annealing temperature is also interesting. Annealing at 350 °C for one hour results in a minor degree of recrystallization due to the lower temperature; recrystallized grains are observed around certain large grains, but in general the recrystallization is quite localized and its extent is limited (Fig. 3.34). Moreover, most of the second phases have dissolved in the matrix. The resultant texture is nearly identical to that of the as-received TRC sheet (Fig. 3.26a). It is observed that the amount of recrystallized grains increases with the increases in temperature. The texture alteration starts at 375 °C and progresses further at 400 °C, wherein the texture becomes almost

similar to the one obtained at the 420 ^{o}C anneal. These observations again suggest that recrystallization is indeed responsible for the texture alteration.

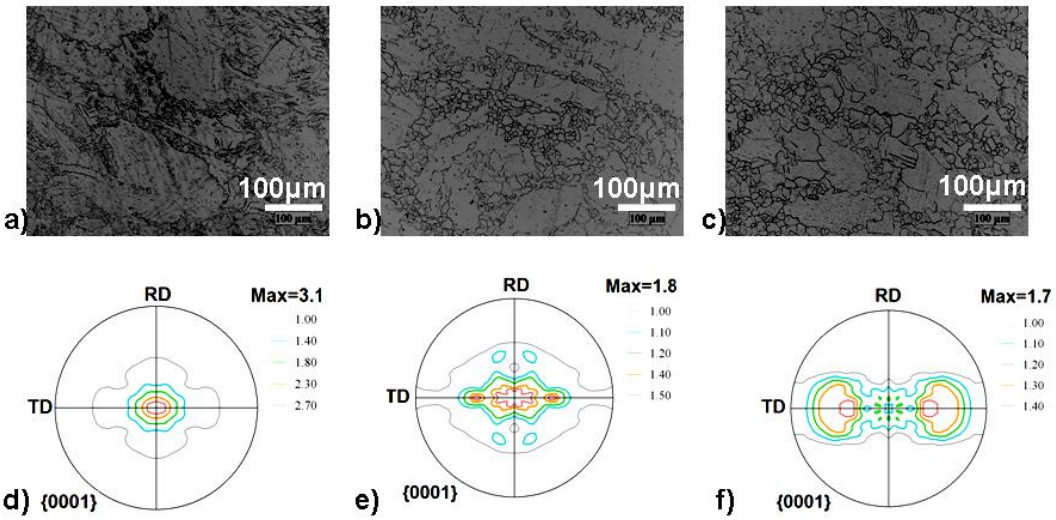

Fig. 3.34 (a-c) Microstructures and (d-f) corresponding surface texture pole figures of the as-received TRC AZ31 annealed for one hour at 350 ^{o}C, 375^{o}C and 400^{o}C, respectively.

The Mechanism of Texture Alteration

Different mechanisms have been proposed as explanations for texture weakening in magnesium alloys [30, 41-43], but the latter is usually attributed to the coalescence of sub-grains formed at the particle/matrix interfaces [30, 42] or at twin boundaries [32]. When texture alteration is assisted by particles, the mechanism is known as particle-stimulated nucleation (PSN) [44]. The TRC AZ31 microstructure does not possess a high incidence of twins but does possess a higher amount of second-phase particles (much higher than the DC-cast AZ31). It is well known that gliding dislocations do not shear non-coherent precipitates. As a result, dislocation pile-up or looping at the particle/matrix interface occurs. The polarity of the tension-compression strain fields of these dislocations leads to the local bending of the crystal at the precipitate/matrix interface. The local strain (and bending) is relieved via the formation of cell and sub-grain formation upon annealing. The sub-grains that form during the recovery stage coalesce

through rotation according to the five-degrees of freedom of low-angle boundaries (tilt, twist, rotation) and nucleate into new grains with substantially different orientations than the parent grain, thereby leading to texture weakening [45]. This recrystallization mechanism is different from the grain-boundary bulging mechanism that results in recrystallized grain orientations closely associated with those of the parent grains. The TEM observations (Figs. 3.25) confirm that dislocation accumulation does exist around the second phases in the as-received TRC AZ31, providing further evidence that PSN is the underlying mechanism of recrystallization that leads to significant change in the texture of annealed TRC AZ31.

The present authors have previously shown [25] that an AZ31 plate solidified slowly (simulating the DC casting cooling rate) develops a basal texture after cold rolling that persists after subsequent annealing. On the other hand, they have also observed [25] that an AZ31 casting solidified at a significantly higher cooling rate develops a basal texture after cold rolling, which does, however, alter after annealing at 420 ^{o}C. This reaffirms the conclusion that the texture alteration in the TRC AZ31 sheet during annealing is related to non-equilibrium solidification that yields a larger fraction of second phases and consequently leads to texture alteration via PSN.

To verify the interaction of particles with recrystallized grains, an EBSD analysis was performed on a sample annealed for 5 min., i.e., a duration that is not sufficiently long to dissolve the second phases in the matrix (Figs. 3.35a&b). Fig 3.35b is the magnified view of the area inside the white square in Fig. 3.35a. In these two figures, the high angle boundaries (>15^{o}) and low angle boundaries (>3^{o}) are delineated with black and white lines, respectively. It is noted that the large grains contain a deformation sub-structure consisting of low-angle boundaries (LAG). The small grains (inside the white square) have little or no deformation sub-structure typical of strain-free recrystallized grains. In this region, most of the small grains are associated with the second-phase particles (some of them are shown in white circle). It can also be clearly observed that the recrystallized grains that are associated with the precipitates exhibit a random texture. Some of the recrystallized grains are adjacent to high angle boundaries and are likely to have nucleated through the grain boundary bulging mechanism. These grains have

orientations very similar to those of the parent grains. It can be concluded that the nucleation of new grains in the annealed TRC AZ31 was associated with grain boundaries and second phase particles, and that the latter leads to texture alteration.

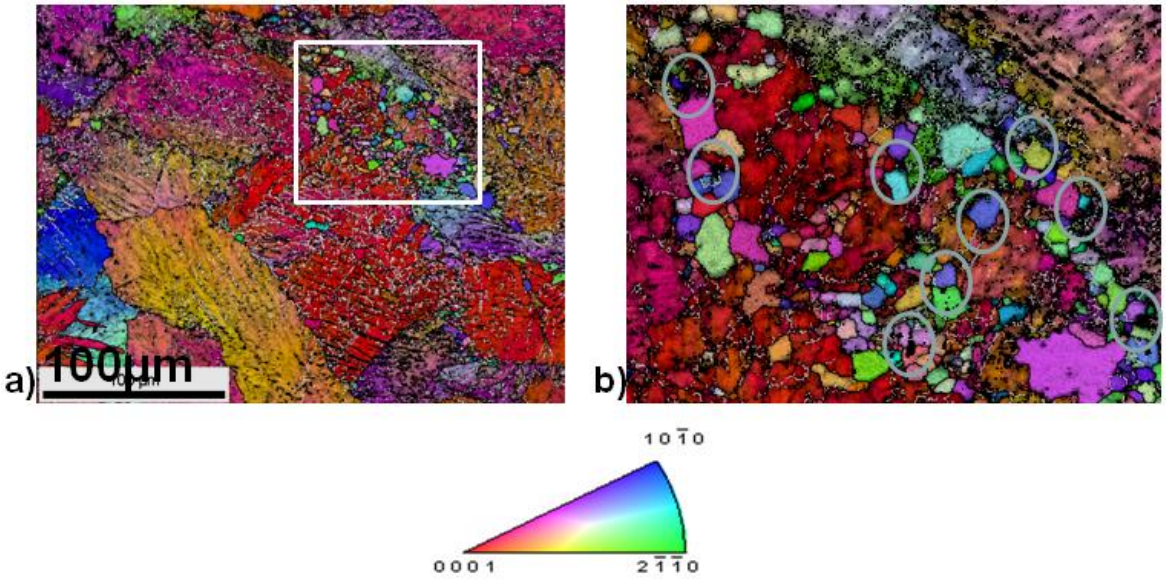

Fig. 3.35 TRC AZ31 sheet after annealing for 5min at 420 ^{o}C; (a) EBSD map on the RD-ND plane, (b) Magnified area in the white square.

Hot-Rolled TRC AZ31

The microstructure of the TRC AZ31 sheet successively rolled at 400 ^{o}C (Fig. 3.36a) exhibits a partially recrystallized structure and shear bands (narrow regions of intense shear that occur at an angle of about 35^{o} to the rolling plane and parallel to the transverse direction [44]). It has been shown that heavily deformed shear bands are preferential nucleation sites for recrystallization and can lead to random textures in some materials [46]. However, it seems that such random texture makes the bands more susceptible to shear deformation, especially via basal slip, and that the grains within shear bands soon gain a basal orientation (basal planes parallel to the sheet surface) upon further rolling. This is illustrated by the {0001} pole figure in Fig. 3.36b.

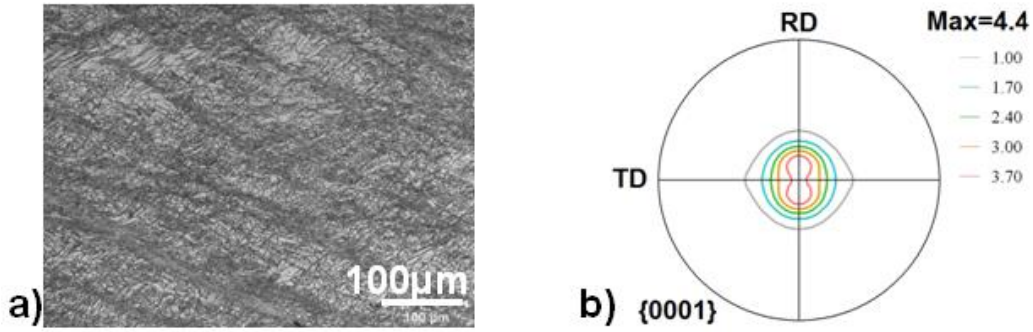

Fig. 3.36 (a) Thickness microstructure and (b) surface texture of the TRC sheet rolled at 400 ^{o}C.

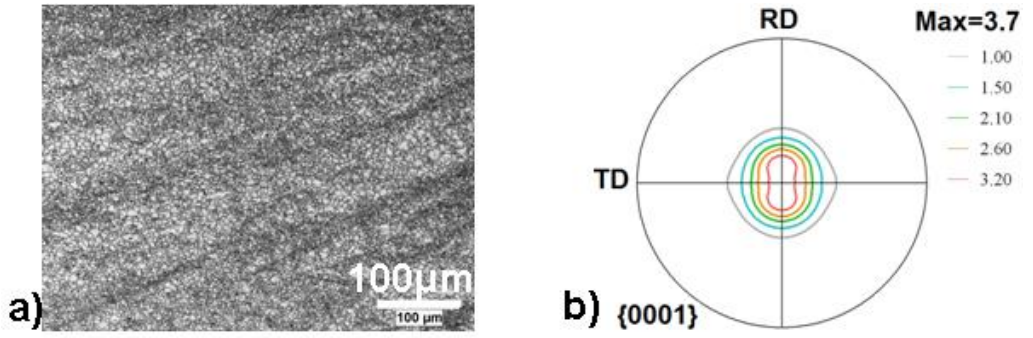

Fig. 3.37 (a) Thickness microstructure and (b) surface texture of the TRC sheet rolled and annealed at 400 ^{o}C.

Rolled and Annealed TRC AZ31

Fig. 3.37a shows that the TRC AZ31 sample that has been rolled and then annealed at 400 ^{o}C for 5 minutes also exhibits a recrystallized structure with characteristic shear bands. The texture (Fig. 3.37b) is similar to the rolled texture shown in Fig. 3.36b. The PSN mechanism of recrystallization is unlikely to occur in this sample since most of the second phases have dissolved in the matrix due to annealing at 420 ^{o}C followed by rolling at 400 ^{o}C. As a result, any subsequent rolling and heat treatment would not have a substantial effect on the texture. The EPMA results show that the centerline macrosegregation still persists after several heating and rolling cycles; this suggests that the TRC parameters must be selected appropriately to minimize the formation of this defect (Fig. 3.38). However, the EBSD analysis (Fig. 3.39) shows that the texture of grains in the centerline-segregation zone is almost identical to the texture of the grains

outside the segregation zone (note that the segregation area appears slightly darker than the rest of the matrix). In other words, the elemental segregation does not have a significant effect on the overall texture of the sheet.

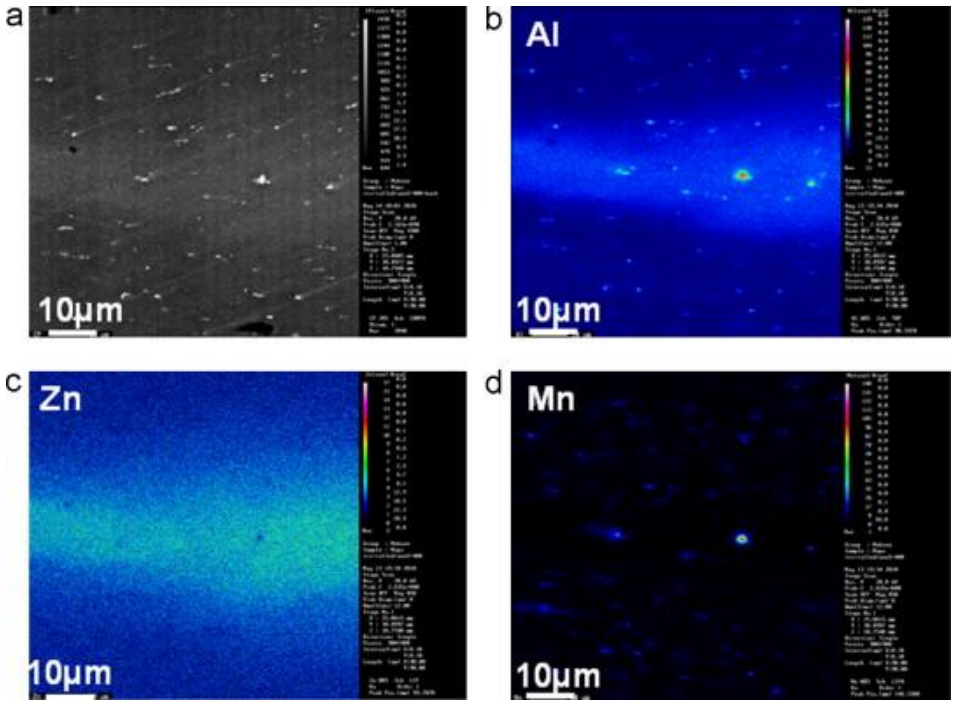

Fig. 3.38 (a) Centerline segregation in the rolled-annealed TRC AZ31 and the EPMA micrographs of (b) Al, (c) Zn, and (d) Mn (the region with higher element percentage appears brighter).

3.3.3.4 The Tensile Properties of TRC AZ31

Typical true stress-strain curves from tensile tests are shown in Fig. 3.40 for the rolling and transverse directions of the TRC AZ31 in the as-received and annealed (1 hr at 420 ^{o}C) conditions. The tensile properties are summarized in Table 3.2. For both conditions, the ultimate tensile strength (UTS) and the elongation in the TD direction are higher than in the RD direction. It is noted that the elongation and the UTS of the TRC AZ31 improve significantly following the annealing treatment at 420 ^{o}C: the elongation in the RD and TD directions show 180% and 65% improvement, respectively, over the as-received condition (Table 3.2), and the improvement in the UTS is 10% in both the RD

and TD directions. Such improvement in elongation could be attributed to basal pole rotation away from the sheet normal direction and to the formation of fine recrystallized grains. Accordingly, the weaker basal texture resulting from annealing facilitates the slip, especially the basal slip which is the most active mechanism. In addition, the material yields at lower stresses. This explains the lower yield strengths in the annealed material (Table 3.2). However, there could also conceiveably be some contribution of the dissolution of second phases in the matrix, which aids dislocation glide.

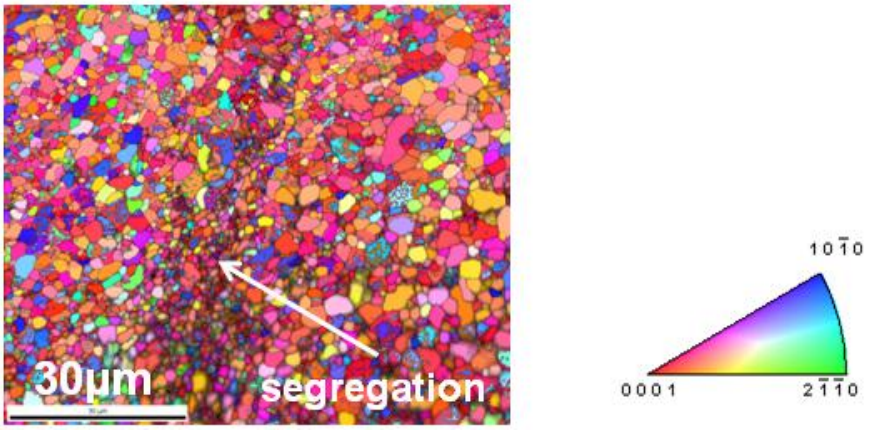

Fig. 3.39 map from the RD-ND plane of the rolled-annealed TRC AZ31 sheet (mid-thickness).

The strain-hardening exponent (*n*-value), which is a measure of the degree of work hardening at a given strain, correlates with the capacity of the material to be stretch-formed uniformly without localized plasticity (necking and tearing). High *n* means that the metal strengthens while deforming and hence exhibits uniform deformation during stretching. Since the work-hardening exponent is not constant over the entire stress–strain curve, *n* was calculated over the strain interval from 0.01 to fracture, which shows a near-linear relationship between ln(δ) and ln(ε). The results also indicate that the *n*-value of the TRC AZ31 increases both in RD and TD by annealing. Also, a recent study shows that a TRC Mg sheet with a higher *n* value does indeed exhibit improved stretch formability at room temperature [47]. Hence, it can be concluded that the weakened texture leads to improved formability in the AZ31 sheet. The higher UTS is also

attributable to the weaker texture and to the high *n*, which delay the localization of deformation and necking.

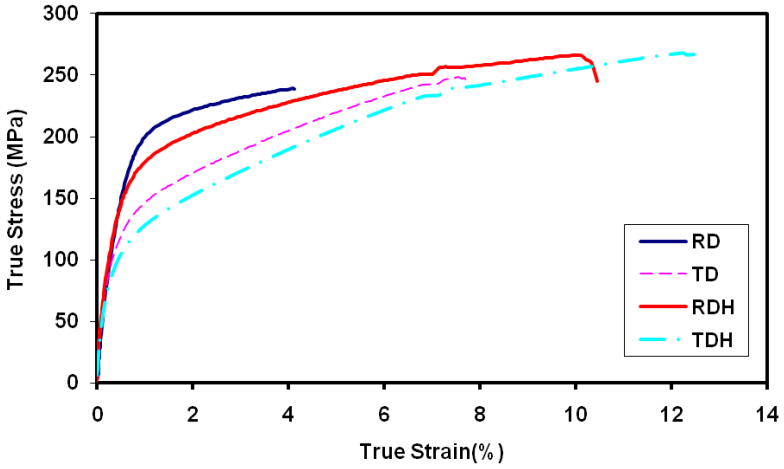

Figure 3.40 Tensile flow curves of the as-received TRC AZ31 (RD and TD) and the annealed (one hour at 420 ^{o}C) TRC AZ31 (RDH and TDH). RD and TD are rolling and transverse directions.

Table 3.2 Tensile Properties of TRC AZ31 in Rolling and Transverse Directions (RD, TD)

Sample	0.2YS% (MPa)	UTS (MPa)	Elongation, %	n Value
TRC AZ31/ RD	153	230	4.0	0.117
TRC AZ31/TD	109	242	7	0.261
Annealed TRC AZ31/ RDH	141	254	11	0.180
Annealed TRC AZ31/TDH	96	264	12	0.318

The main purpose of the TRC Mg sheet is cost reduction, namely through the elimination of the hot rolling steps employed in the conventional Mg sheet production. The TRC process can produce a cast and warm-rolled sheet in one step. It is conceivable that TRC sheets may not need to be rolled further for certain sheet components. Especially for components that are to be formed at low temperatures, adequate formability (bending, stamping) of the TRC sheet would be very important. This property

is mainly controlled by the extent of the basal texture in the sheet, since the basal texture strongly limits the sheet formability [20]. This has been the shortcoming of the commercial AZ31-H24 sheet, in which the basal texture is readily developed during the early stages of hot rolling and persists over the entire life of the sheet. There have been several attempts to alleviate the basal texture by alloying, e.g., by the addition of rare earth elements [28-29, 41]. Nevertheless, due to its optimum strength and cost, AZ31 remains the most common alloy for sheet production. In this respect, the annealing treatment investigated in this study, with its ability to alleviate the basal texture in the TRC AZ31 sheet, is highly significant. The texture alteration of AZ31 obtained by annealing of TRC AZ31 is a significant step toward achieving a low-cost magnesium sheet with improved formability.

3.3.5 Conclusions

This study has investigated the microstructure and texture of the AZ31 sheet produced by various methods, as well as the subsequent annealing textures. Table 3.3 summarizes the results.

1. The as-cast TRC AZ31 sheet is mainly characterized by large dendritic columnar grains; however, small grains are also seen near the edge and the mid-thickness of the sheet. Centerline segregation of Al, Zn and Mn is also observed.
2. The cooling rate near the sheet edge (surface) is at rapid solidification rates (325 ^{o}C/s), while the mid-thickness has solidified in Scheil solidification mode (150 ^{o}C/s). As a result, the surface is depleted of the second phases due to the solute supersaturation, while the amount of second phases in the mid-thickness is higher than the equilibrium amount.
3. The basal texture prevails in the as-received TRC sheet due to the rolling deformation applied during the TRC process. It seems that the large grains that are predominant in the structure are the main contributors to the overall basal texture in the sheet, even though the small grains have a random texture.
4. Annealing at 420 ^{o}C alleviates the basal texture in the TRC AZ31 sheet, thereby improving the ductility and the strain-hardening response (n-value).

Table 3.3 The Microstructure and Texture of AZ31 in Various Conditions.

Condition	Microstructure	Texture
TRC (as-received)	• Mixture of dendritic columnar & equiaxed grains • SDAS: 7.5 μm at the edge (CR~ 325 ^{o}C/s) and 10 μm at the mid-thickness (CR~150 ^{o}C) • f_{sp} ~12vol% • $(Al,Zn)_{49}Mg_{32}$ and Al-Mn intermetallics • Centerline macrosegregation	Basal
Plate permanent-mould cast at the cooling rate of TRC (no warm deformation)	• Dendritic microstructure • Mixture of columnar & equiaxed grains	Prismatic
Simulated DC ingot	• Equiaxed dendritic grains • SDAS ~ 35 μm • f_{sp} ~6vol%	-
Annealed TRC (420^{o}C)	Mixture of coarse and fine equiaxed grains	Relatively random
Rolled TRC	Presence of shear bands, recrystallized	Basal
Rolled + annealed TRC	Fine equiaxed-grains	Basal

3.3.6 References

1. T. Kaneko, M. Suzuki, , Mater. Sci. Forum, 2003, 419-422, pp. 67-72.
2. B. Engl, , Light Metal Age, 2005. 63(5), pp. 14-19.
3. E. Baril, P. Labelle, M.O. Pekguleryuz, J. Metals (JOM-US), 2003. 55(11): pp. 34-39.
4. M. O. Pekguleryuz, A. A. Kaya, Adv. Eng. Mater., 2003. 5(12):p p. 866-878.
5. I.-H. Jung, W. Bang, I. J. Kim, , H. I.Sung, , W. J.Park,; D. Choo, , S. Ahn, , in: R. S. Beals (Ed.) Magnesium Technology. 2007 TMS Orlando, FL, USA pp. 85-88.
6. E. J. Vinarcik, Light Metal Age., 2004. 62(3-4):p p. 56-57.
7. E. Doege, , K. Droder, , J. Mater. Process. Technol., 2001. 115: pp. 14–19
8. K. Schwerdtefeger, , ISIJ International, 1998. 38 (8), pp. 852-861.
9. C. Yang, , P. Ding, , D. Zhang, , F. Pan, , Mater. Sci. Forum. 2005. pp. 427-430.

10. D. R., Herling, J. A. Carpenter, P. S. Sklad,in FY2005 Progress Report for Automotive Lightweighting Materials. 2005, US department of Energy.
11. H. Watari, , T. Haga, , N. Koga, , K. Davey, , J. Mater. Process. Technol., 2007. 192-193: pp. 300-305.
12. D. Liang, , C. B. Cowley, JOM, 2004. 56(5): pp. 26-28.
13. S.-H. Kim , B.-S. You, C. D. Yim, Y.-M. Seo, Mater. Lett. 2005. 59: pp. 3876 – 3880.
14. D. Li,., Q. Wang, , W. Ding, , Mater. Sci. Forum. , 2007. 546-549(1): pp. 311-314.
15. F. Kaiser, J. Bohlen, D. Letzig, K.-U. Kainer, A. Sfyczynski, C. Hartig, Adv. Eng. Mater., 2003. 5(12): pp. 891-896.
16. A. Jager, P. Lukac, V. Gartnerova, J. Haloda, M. Dopita, Mater. Sci. and Eng. A 2006. 432: pp. 20–25.
17. M. R. Barnett, M. D. Navea, C. J. Bettlesb, Mater. Sci. Eng. A 2004. 386: pp. 205–211.
18. H. T. Jeong, T. K. Ha, J. Mater. Process. Technol. 2007. 187–188:p p. 559–561.
19. F. Kaiser, D. Letzig, J. Bohlen, A. Styczynski, Ch. Hartig, , K. U. Kainer, Mater. Sci. Forum, 2003. 419-422: p. 315-320.
20. E. Yukutake, J. Kaneko M. Sugamata, , J. Jpn Soc. Technol. Plast. 2003. 44: pp. 276-280.
21. S. S. Park, J. G.Lee, H. C. Lee, N. J. Kim, , in A.A. Luo(Ed.) Magnesium Technology 2004 TMS, USA, pp. 107-112.
22. Y. Nakaura, K. Ohori, Mater. Sci. Forum. 2005. pp. 419-426.
23. Y. Nakaura, A. Watanabe, K. Ohori, Mater. Trans., 2006. 47(7): pp. 1743-1749.
24. S. S., Park, D. H. Kang, , G. T. Bae, N. J. Kim, Mater. Sci. Forum, 2005. 488-489: pp. 431-434.
25. M. Masoumi, F. Zarandi, M. Pekguleryuz, Scr. Mater., 2010, 62 (2010), pp. 823–826
26. R. Kawalla, M. Oswald, C. Schmidt, M. Ullmann, H.-P. Vogt, N. D. Cuong, , in (Ed.), Magnesium Technology,TMS 2008, USA, pp. 177-182.
27. S.S., Park, G.T., Bae, J.G., Lee, D.H., Kang, K.S., Shin, N. J. Kim, , Mater. Sci. Forum, 2007, 539-543, pp. 119-126.
28. L.W.F. Mackenzie, M. O. Pekguleryuz, Scr. Mater., 2008. 59(6): pp. 665-668.

29. L.W.F. Mackenzie, M. Pekguleryuz, Mater. Sci. Eng. A, 2008. 480(1-2): pp. 189-197.
30. E. A. Ball, P. B. Prangnell, Scr. Mater., 1994. 31(2): pp. 111-116.
31. A. Galiyev, R. Kaibyshev, G. Gottstein, Acta Mater., 2001. 49(7): pp. 1199-1207.
32. É. Martin, L. Jiang, S. Godet, J. J. Jonas, Int. J. Mater. Res., 2009. 04: pp. 576-583.
33. M.C. Flemings, Solidification Processing. 1974, New York, London and Sydney.: McGraw-Hill Book Co.
34. W. Kurz, D J Fisher, Fundamentals of Solidification. 1986, Trans Tech Publications Ltd. Pp. 245.
35. M. Masoumi, M. Pekguleryuz, Trans. Am. Foundry Soc. 2009. 117: pp. 617-626.
36. J.A. Sarreal, G. J. Abbaschian, Metall. Trans. A., Nov. 1986. 17A(11): pp. 2063-2073.
37. Metallography and Microstructures ed. G. F. Vander Voort Vol. 9. 2004: Materials Park, OH: ASM International,.
38. P. Cao, D. H. StJohn, M. Qian, Mater. Sci. Forum, 2005. 488-489: pp. 139-142.
39. G.V. Raynor, The Physical Metallurgy of Magnesium and its Alloys. 1959, New York: Pergamon Press.
40. W. Borbige, D. D Liang, Magnesium Alloy Sheet and Its Production. 2006, US2006231173: USA.
41. J. Bohlen, M. R. Nürnberg, J. W. Senn, Letzig, D., S. R. Agnew, Acta Mater., 2007. 55(6): pp. 2101-2112.
42. L. W. F. MacKenzie, B. Davis, F. J. Humphreys, G. W. Lorimer, Mater. Sci.Technol., 2007. 23(10): pp. 1173-1180.
43. J. W. Senn, S. R. Agnew, Proceedings of Magnesium Technology in the Global Age, L.W.F. MacKenzie ,M.O. Pekguleryuz (Eds.). 2006: Montreal, Canada. pp. 115.
44. F. J.Humphreys, M. Hatherly, Recrystallization and Related Annealing Phenomena. 2 ed. 2004: Great Britain by Galliard Ltd., UK, .
45. R. E. Reed-Hill, R.Abbaschian, Physical Metallurgy Principles. Third ed, 20 Park Plaza, Boston, MA: PWS.
46. H. Paul, J. H. Driver, Z. Jasienski, Acta Mater., 2002. 50(4): pp. 815-830.
47. D. H. Kang, D.W. Kim, S. Kim, G. T. Bae, K. H. Kim, and N. J. Kim, Scr. Mater., 2009. 61(7): pp. 768-77

CHAPTER 4

EFFECTS OF ALLOYING ADDITIONS ON THE TEXTURE OF MAGNESIUM SHEET ALLOYS

This chapter which is comprised of three journal papers, the effects ofCe and Sr addition on Mg-1wt.%Mn sheet alloy and the effect of addition Sr addition on the Mg-1wt.%Zn alloy are determined. Section 4.1 (*The influence of Ce on the Microstructure and Rolling Texture of Mg-1wt.%Mn alloy*) attributed the texture weakening of Mg-1%Mn sheet alloy by Ce, to the solid solubility of Ce in Mg. This paper has been published in Materials Science and Engineering A. Sections 4.2 and 4.3 present work that was carried out determining the effect of Sr additions to Mg-1wt.%Mn and Mg-1wt.%Zn alloys. It was found that Sr weakened the rolled and annealed textures of both alloys and the underlying texture weakening mechanisms were determined to be due to particle stimulated nucleation (PSN) of recrytsallized grains at the Sr containing particles. Both studies have been submitted for publication: 4.2 (*Effect of Sr on the Microstructure and Texture of Rolled Mg-Mn-Based Alloys*) to Scripta Materialia and 4.3 (*The influence of Sr on the Microstructure and Texture Evolution of Rolled Mg-1%Zn Alloy) to* Materials Science and Engineering A.

4.1 The influence of Ce on the Microstructure and Rolling Texture of Mg-1%Mn Alloy *

*This section has been published: **M. Masoumi,** M. Hoseini, M. Pekguleryuz, "The Influence of Ce on the Microstructure and Rolling Texture of Mg-1%Mn alloy" Mat. Sci. Eng. A Vol. 528, no 7-8, 2011, pp. 3122-3129.

In this study, the microstructures and textures of rolled and rolled-annealed Mg-1wt.%Mn-based alloys containing different levels of Ce (from 0.05 to 1.0wt.%) were examined. The Ce addition refined the as-cast and rolled-annealed grain structure of Mg-1wt.%Mn alloy. Moreover, the overall texture intensity of basal pole was weakened for rolled as well as rolled-annealed Mg-Mn-Ce alloys compared to the Mg-1wt.%Mn (M1) alloy. The texture weakening was attributed to the solid solubility of Ce in Mg rather than particle stimulated nucleation (PSN) or *c/a* ratio alteration.

4.1.1 Introduction

Automotive applications of magnesium alloys have received significant attention for the purpose of vehicle weight-reduction. To date, the application of magnesium alloys in cars has been limited to die-cast parts, such as steering-wheel cores, engine-head covers, brake-pedal brackets, instrument panels, seat frames, transmission cases and engine block [1-4]. The use of magnesium in automotive body structure has great potential for further weight reduction [5]. Currently, AZ31 (Mg-3wt.%Al-1wt.%Zn) is the most common Mg *sheet alloy* commercially produced by hot rolling of direct-chill (DC) cast ingot. The hot-rolled sheet, commonly designated as AZ31-H24, exhibits non-uniform grain sizes [6, 7]. Additionally, rolling orients the {0002} basal planes of the Mg hexagonal closed packed (HCP) crystal structure parallel to the sheet surface having the $[10\bar{1}0]$ diagonal axis parallel to the rolling direction [6-9]. This phenomena is related to low critical resolved shear stress (CRSS) of basal slip in Mg which facilitates the activation of basal slip during deformation [10]. It is generally known that cubic metals with body-centered and face-centered cubic structures (BCC & FCC) are more formable than HCP metals such as

magnesium since they can provide at least five independent slip systems required by von Mises criterion for formability. HCP Mg has only two independent slip systems at room temperature, therefore additional slip systems need to be activated to maintain integrity of the grain boundary. Koike *et al.* [11] studied the deformation behaviour of fine-grained (7μm) AZ31 samples fabricated by ECAP process. They determined that <*c* + *a*> pyramidal slip and <*a*> prism slip activation occurred at a plastic anisotropy of 2.5 and 2.2 instead of 10-100 as expected from single crystal data [12]. Prismatic <*a*> and pyramidal <*c* + *a*> slip system can provide two and five additional slip systems [12]. Therefore, if the difference in CRSS of these slip systems can be further reduced to activate non basal slip, the Von Mises-Taylor criterion can be satisfied.

The presence of basal texture adversely affects formability and as a consequence considerably limits the variety of components which can be manufactured from Mg sheet. The possibility to enhance the magnesium alloys formability by modifying the texture has been verified [13]. Considerable effort is currently being conducted to weaken the basal texture or attain random texture in rolled magnesium sheet [14, 15]. Recently, it has been shown that twin-roll-cast (TRC) AZ31 sheet can develop weaker textures upon annealing due to the presence of a metastable cast/deformed structure of TRC [15, 16]. Non-basal or weak textures have been reported in Mg-RE (RE: rare earth elements) alloys [14, 17-20] and in Mg alloys with low levels of Li [21]. Although the principal effect of the RE elements on the texture development during rolling and following annealing is well established, the mechanisms liable for these alterations in texture are still under investigation.

Mg-Mn alloys have been used as sheet material due to good rolling behaviour, weldability and corrosion resistance combined with a medium strength [22]. This alloy has usually a coarse grain structure and few insoluble Mn particles [22]. Mg-Mn sheet alloys were developed with a relatively high manganese content (1.0 to 2.0wt.%) [23, 24]. In this alloys a peritectic reaction results in the formation of Mg solid solution (α-Mg) and α-Mn. This paper reports on the effects of Ce on the microstructure and the texture

of Mg-Mn alloy. This is part of a larger investigation, which aims at developing alternative Mg alloys for sheet and twin-roll casting process [19, 21].

4.1.2 Experimental Procedure

Pure Mg (99.5wt.%, supplied by MEL), Mg-7wt.% Mn master alloy (supplied by KB Alloys) and pure Ce (99.9wt.%, supplied by Hefa Rare Earth Canada Co. Ltd) were used to prepare the desired alloys. The melting of pure Mg was carried out in a 20 KW, 5 kHZ Norax Canada induction furnace, using a graphite crucible. A protective gas mixture of sulphur hexafluoride, SF_6, in a carrier gas of carbon dioxide, CO_2, was used to prevent melt oxidation. The temperature of the melt was monitored via a K-type (chromel-alumel) thermocouple. About 0.550 kg melt was prepared for each casting and the melt was poured from a casting temperature of 720 ^oC. A 125mm×100mm×6mm plate of each alloy was cast into a tool steel mould preheated at 400 ^oC. The chemical analysis of the alloy samples taken from the as-cast plates is in table 4.1. The alloy compositions are, hereafter, given in wt.% unless otherwise specified. The casting plates were homogenized in a SPX Blue M electric furnace for 8h at 450 ^oC. Plate specimens (40mm×40mm) with a thickness of 6 mm were machined from the annealed material.

Table 4.1 Alloy Compositions

Alloy	**Alloy Symbol**	**Mn (wt.%)**	**Ce (wt.%)**
Mg-1Mn	M1	1.08	<0.001
Mg-1Mn-0.05Ce	ME10(0.05Ce)	1.05	0.06
Mg-1Mn-0.1Ce	ME10(0.1Ce)	1.15	0.10
Mg-1Mn-0.2Ce	ME10(0.2Ce)	0.97	0.20
Mg-1Mn-0.5Ce	ME11(0.5Ce)	1.11	0.50
Mg-1Mn-1.0Ce	ME11(1.0Ce)	1.04	0.94

The thickness of homogenized plate samples were reduced to 1.4 mm thickness through seven rolling passes, with equal reduction of about 0.65 mm in each pass, using a

laboratory-scale Stanat rolling mill. The rolling process started with an initial reduction of ~10% and the final reduction was ~30% resulting in a total reduction of 75%. The rolling specimen was preheated at 400 ^{o}C for 15 minutes before the first rolling pass and for 5 minutes before each subsequent pass. The rolled sheet samples were subsequently annealed at 450 ^{o}C for 15 minutes after the last rolling pass.

Specimens for microstructural examination were taken from the thickness; i.e. the plane of rolling and sheet normal directions (RD-ND). The specimens were prepared by grinding on SiC paper and polished with diamond paste followed by etching in acetic-picral or 5% nital. The microstructure was studied via optical and scanning electron microscopy (SEM). X-ray elemental distribution was obtained in a JEOL 8900 electron probe micro-analyzer (EPMA) having a resolution of 70 nm.

The overall crystallographic orientation was evaluated via x-ray diffraction (XRD) using a Siemens D-500 x-ray diffractometer. The specimens were ground successively to remove almost 10% of the sheet thickness and then polished with 1 μm diamond slurry. In order to eliminate the residual stresses of the surface, the specimens were chemically polished in 10% nital solution for 60 seconds. Raw pole figures of {0002}, $\{10\bar{1}0\}$ and $\{10\bar{1}1\}$ were recorded, and the orientation distribution function (ODF) was calculated using TexTools texture analysis software. Recalculated pole figures were derived from the ODFs. The grain orientation was also studied using the electron back scattered diffraction (EBSD) method in a Phillips SEM at 20 kV accelerating voltage and 70^{o} tilt angle. The EBSD samples were polished with 1 μm diamond slurry followed by electropolishing at 20 V using a 10% nital solution cooled to 0 ^{o}C. Macrohardness was measured using a Vickers tester under 3-g indenting load with a dwell time of 10 s.

4.1.3 Results and Discussion

4.1.3.1 As-cast Microstructures

M1 Alloy

Fig. 4.1 presents the microstructure of M1 alloy. A mixture of equiaxed, and columnar grains, can be seen (Fig. 4.1a) at the edge of plate (width range 70-260 μm in width and 150-400 μm in length). However, underneath the surface, very coarse and long columnar grains can be observed (200-500 μm in width and 1000- 3000 μm in length), which almost extend from the surface to the mid-thickness of the plate (Fig. 4.1b).

The SEM/EDS analyses of M1 alloy are shown in Fig. 4.1c&d. The results reveal that the matrix is α-Mg (Mg-Mn solid solution), and the precipitates are Mn-Si phases which could be $MnSi_4$, Mn_9Si_2, or Mn_6Si [25].

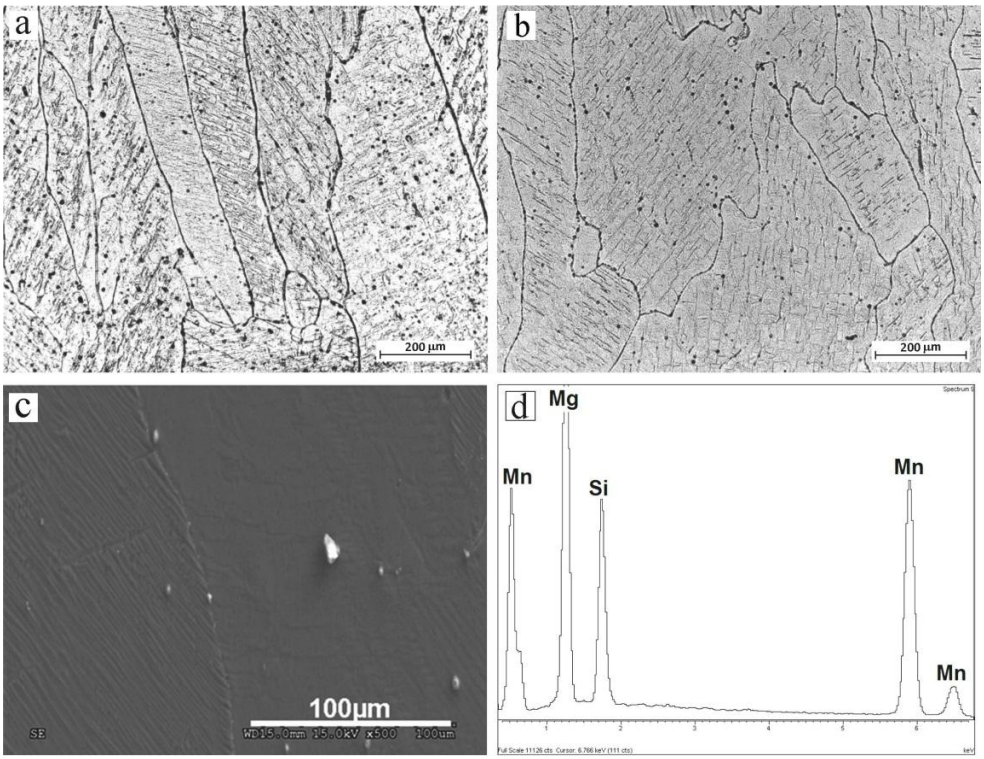

Fig. 4.1 As-cast microstructure of M1 (a) edge (b) mid-thickness. (c) SEM micrograph showing the secondary phases in M1 (d) EDS spectrum from the Mg-Mn-Ce-Si particles.

ME Alloys

The as-cast grains structure of M1 alloy significantly refines by addition of cerium (Figs. 4.2 & 4.3). A mixture of columnar, equiaxed and semi equiaxed grains can be observed

in the area just beneath the surface of all ME alloys. However, a mixture of relatively fine equiaxed grains and coarse columnar grains can be seen in the mid-thickness of the specimens. However, the grains are much finer than the coarse columnar grains in the M1specimen. In general as the Ce content increases, the grains structure gets finer both at the edge and mid-thickness of plate. Table 4.2 shows the grain size ranges at edge and mid-thickness of M1, ME10(0.05) and ME10(0.1) alloys . The finer grain size of ME alloy compared to that of M1 can be attributed to an increase in growth restriction factor by addition of Ce. It has been shown that Grain size has indirect proportion to the growth restriction factor [26, 27].

Plate-like second phases can be observed both in the matrix and in grain boundaries of the ME alloys. The SEM and EDS analysis of ME11 (0.5Ce), at the edge and the mid-thickness of plate, are shown in Figs. 4.4. The results reveal that at the edge of plate, the α-Mg matrix is Mg-Mn solid solution, and the particles are Mg-Ce presumed ($Mg_{12}Ce$) [28] and Mg-Ce-Mn presumed ($(Mg, Mn)_{12}Ce$) [28] phases. As it is observed, the grain boundaries contain Mg-Ce(Mn) particles and the intra-granular particles are Mg-Ce. At the plate mid-thickness, the α-Mg matrix is Mg-Mn solid solution, however the second phase particles are Mg-Ce and Mg-Ce-(Mn,Si) phases. The Mg-Ce plate-like particles are formed close to grain boundaries, and the round shaped Mg-Ce-Mn-Si particles are both in grain boundary and in matrix (Fig 4.4c). The formation of particle containing Si could be due to segregation of Si that its concentration increase as the solidification front moves toward plate mid-thickness. When Si build up reaches a critical concentration, the particle containing Si could be formed**.** The area fraction of secondary phases, f_{sp}, in ME alloys was determined by image analysis; as Ce increases from 0 to 1.0wt.%, the f_{sp} increases from 1.5% to 7.3%.

Hardness measurements show that with Ce increasing from 0 to 1.0wt.%, the hardness increases from 31.8 to 37.2 HV. This could be attributed to finer grain size (Hall-Petch relation) and the increase in the amount of second phases.

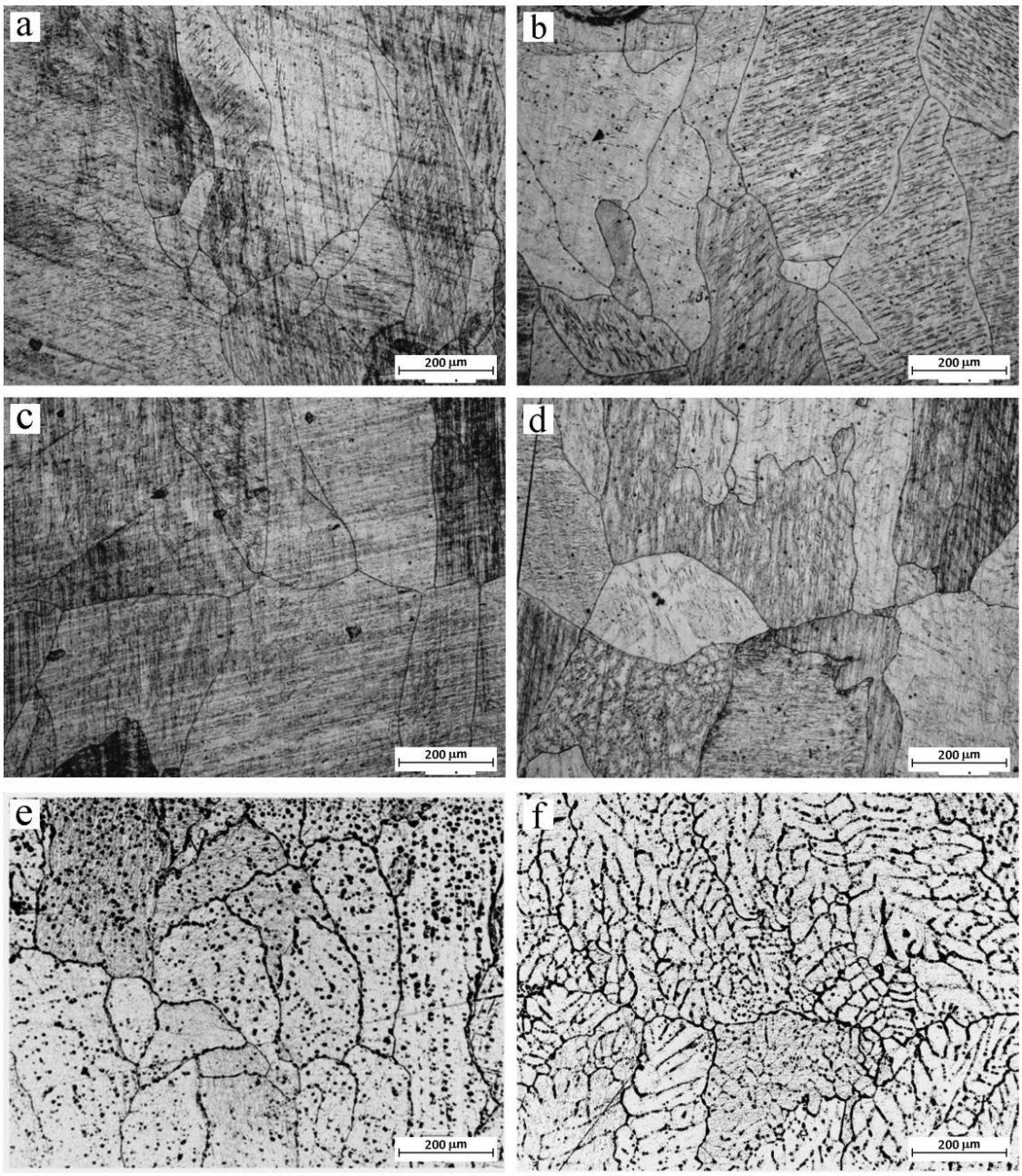

Fig. 4.2 As-cast microstructures of ME10 alloys (a) Edge and (b) mid-thickness of ME10(0.05Ce). (c) Edge (d) mid-thickness of ME10(0.1Ce). (e) Edge (f) mid- thickness of ME10(0.2Ce).

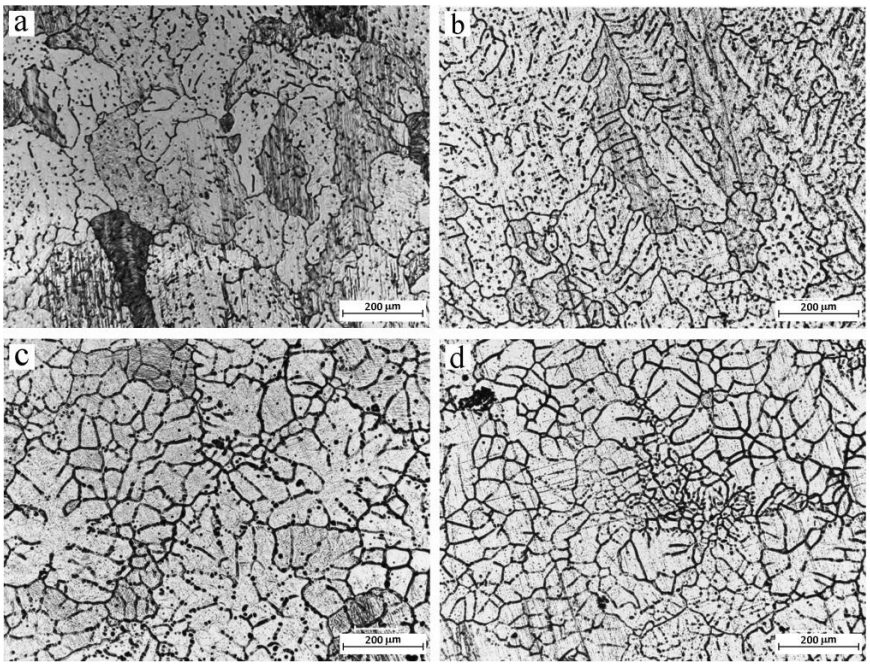

Fig. 4.3 Microstructures of as-cast ME11 alloys (a) Edge and (b) mid-thickness of ME11(0.5Ce). (c) Edge and (d) mid-thickness of ME11(1.0Ce).

Table 4.2 Grain Size of M1 and ME Alloys

alloys	Grain size range				effective grain size
	edge		center		
	Width (μm)	Length (μm)	Width (μm)	Length (μm)	
M1	70 to 260	150 to 400	200 to 500	1000 to 3000	465
ME10(0.05Ce)	70 to 250	130 to 350	180 to 470	880 to 3000	410
ME10(0.1Ce)	60 to 230	100 to 310	160 to 410	750 to 1600	325

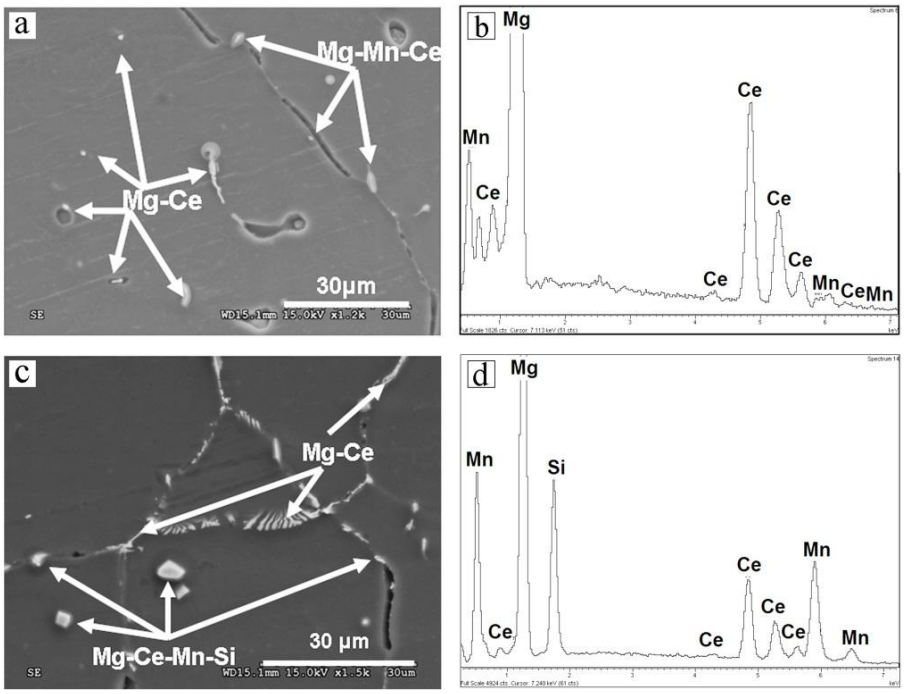

Fig. 4.4 SEM micrographs showing the second phases: (a) ME11(0.5Ce) at the edge and (b) the EDS spectrum of the Mg-Mn-Ce particles. (c) ME11(0.5Ce in the) mid-thickness and (d) the EDS spectrum of the Mg- Mn-Ce-Si particles.

4.1.3.2 Microstructures of rolled and rolled-annealed alloys

The optical micrography of deformed (rolled, forged) Mg-Mn and Mg-Mn-Ce alloys is difficult due to their poor response to etching [29]. Despite of the many etchants that were tried, the as-rolled microstructures of the alloys could not be revealed via optical microscopy. Instead, the EBSD technique was applied to study the microstructure of some selected specimens in the rolled condition (Fig. 4.5). All samples, despite having deformed structures are also partially recrystallized following the rolling at 400 ^{o}C. Shear bands and also some twins can be observed in ME alloys**.**

The optical micrographs of the M1 and ME alloys after annealing at 450 ^{o}C for 15mins are shown in Figs. 4.6a-f. A pretty uniform recrystallized grain structure is observed in all ME samples. In the alloys with high level of Ce (ME11 alloys), during rolling coarse second-phase particles of the cast structure are broken up into smaller

fragmented particles, which are aligned parallel to the rolling axis (materials flow). The grain size of the rolled-annealed ME alloys have decreased slightly from ~13 to ~10 μm with an increase in the Ce content (from 0 to 1wt.%). It can be assumed that the second phase particles may have had a minor influence on grain growth during hot rolling and consecutive annealing.

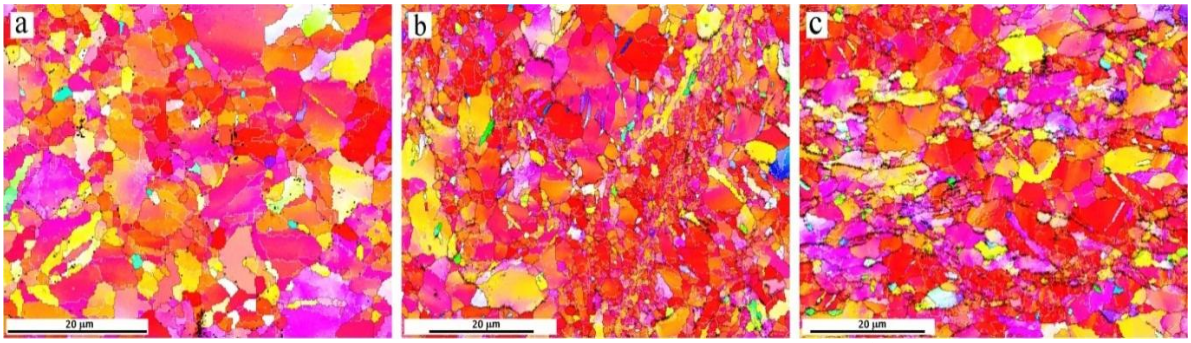

Fig. 4.5 EBSD maps from the RD-ND plane of the as-rolled at 400 ^{o}C: (a) M1 alloy (b) ME11(0.05Ce) and (c) ME10(0.1Ce).

4.1.3.3 Texture of rolled and rolled-annealed alloys

The texture of the alloys following rolling at 400 ^{o}C is presented in Fig. 4.7. In all alloys, the basal planes are aligned parallel to the sheet surface (basal texture). However, M1 alloy has the strongest basal texture, having the intensity of more than 8 times random in the basal pole figure (Fig. 4.7b). ME alloys also have a basal texture, but cerium additions produce a texture weakening effect, as indicated by the lower peak intensities (Figs. 4.7c-g). At 0.05 and 0.1wt.%Ce, the texture intensity reduces to about one half and one-third of M1. This obviously reveals that addition of very minor elements to M1 based alloys can drastically weaken the strength of the basal texture. However, it seems that the addition of more than 0.1% Ce, have no further significant effect on the texture intensity. It is also noted that, with increasing Ce, the angular distribution of basal poles is broadened in both the rolling direction (RD) and transverse direction (TD). The texture contour broadens from 33◦ in M1 alloy towards 44◦ with increasing Ce. Once again, Ce > 0.1%wt. has no further influence on the angular distribution of the basal poles. The textures of the annealed samples are presented in Fig. 4.8. Annealing at 450 °C for 15

minutes has a minor effect on the texture of the alloys, the maximum intensity decreases but the general features of pole figure do not alter.

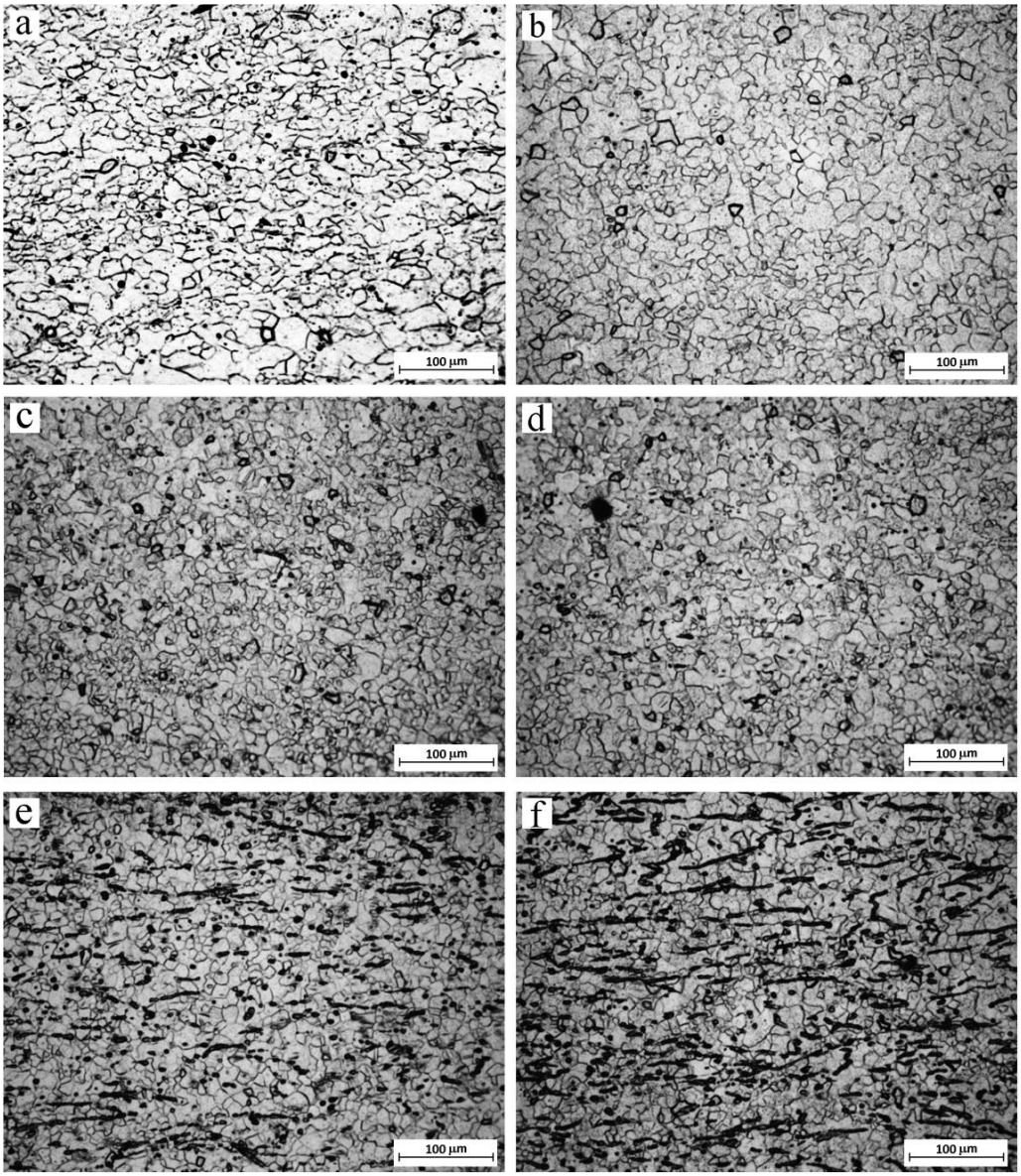

Fig. 4.6 Microstructures of the alloys in the rolled-annealedcondition (a) M1, (b) ME10(0.05Ce), (c) ME10(0.1Ce), (d) ME10(0.2Ce), (e) ME11(0.5Ce) and (f) ME11(1.0Ce).

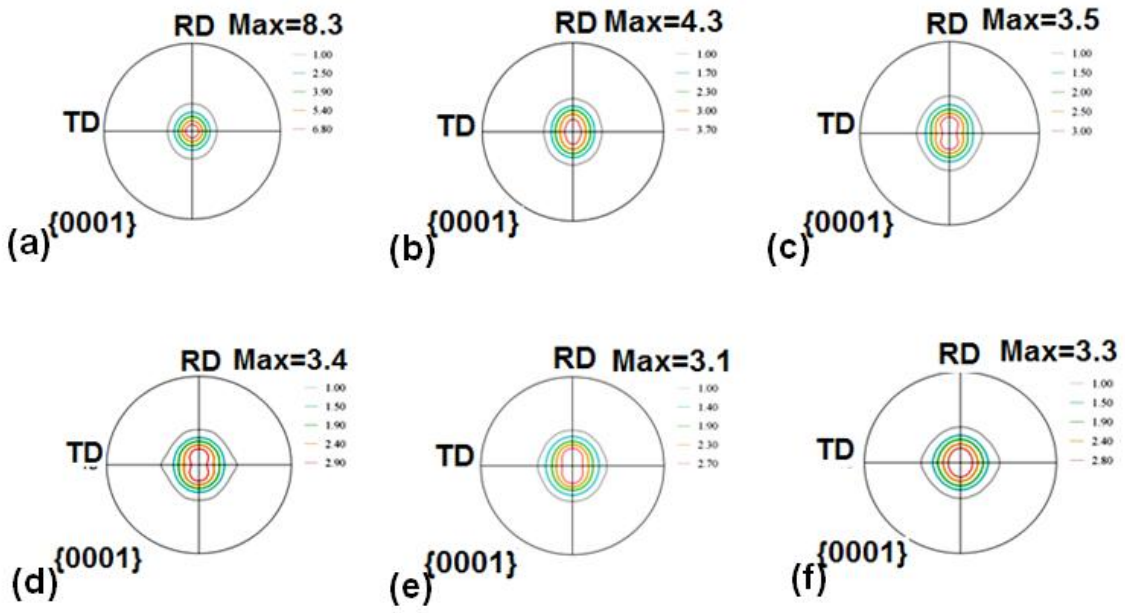

Fig. 4.7 Surface texture pole figures of alloys rolled at 400 ^{o}C: (a) M1, (b ME10(0.05Ce) (c) ME10(0.1Ce), (d) ME10(0.2Ce), (e) ME11(0.5Ce) and (f) ME11(1.0Ce).

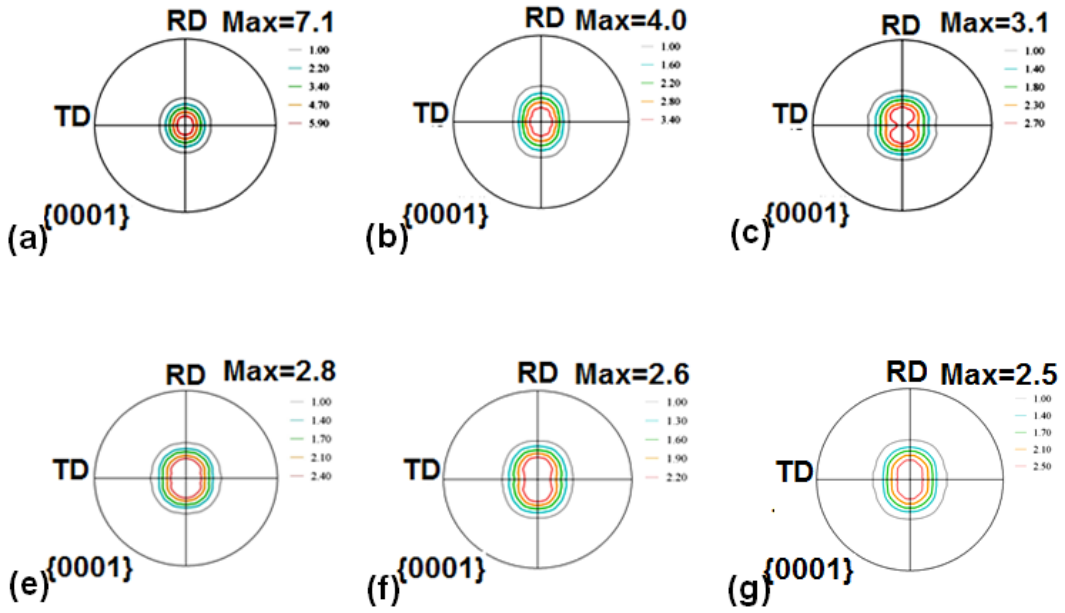

Fig. 4.8 Surface texture pole figures of alloys rolled and annealed at 450 ^{o}C: (a) M1, (b) ME10(0.05Ce), (c) ME10(0.1Ce), (d) ME10(0.2Ce), (e) ME11(0.5Ce) and (f) ME11(1.0Ce).

In order to better quantify the basal pole spread in texture, the percentage of basal planes as a function of the angle of deviation from the sheet normal direction (ND) were plotted (Fig. 4.9). As shown, the addition of Ce reorients the basal planes away from the sheet ND as compared with M1. In other words, the percentage of basal planes that have an orientation away from ND increases.

4.1.3.4 The Mechanism of Texture Evolution in ME Alloys

Texture weakening (randomization) is usualy attributed to the coalescece of sub-grains formed at the particle/matrix interfaces [20, 30] known as particle-stimulated nucleation (PSN) [31]. However, in this study, despite the existence of second phase particles and stringers in the matrix, there seems to be no correlation between the amount of second phases (which increases with increasing Ce) and the texture weakening. The low levels of Ce (0.05wt.% and 0.1wt.%) with only a small amount of second phase produces a significant drop in texture strength. The decrease in the maximum intensity is small in ME10 (0.2Ce) and ME11 alloys despite the significant increase in the amounts of second phases. It can be concluded that in current condition the second phase particles do not lead to PSN in Mg-Mn-Ce alloys.

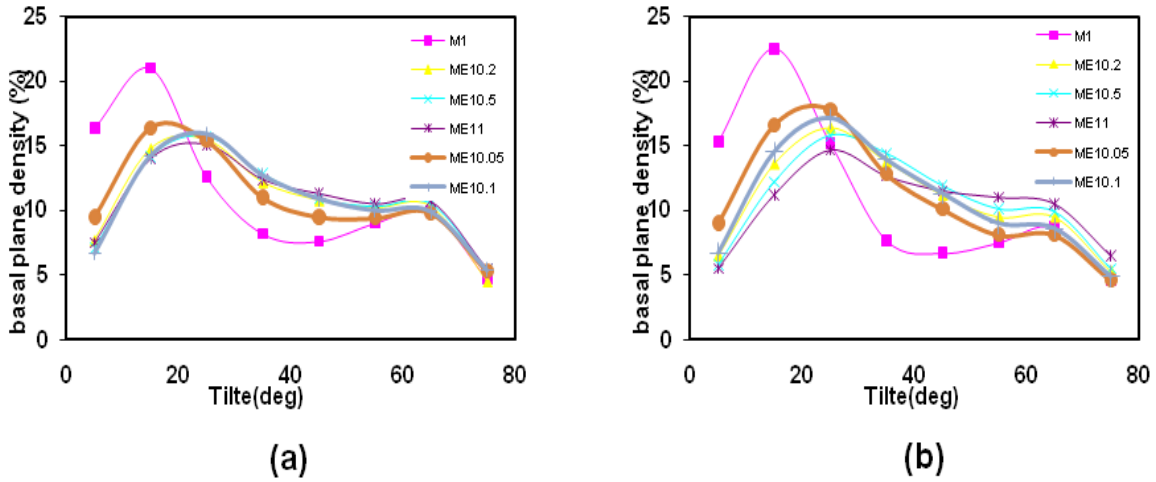

Fig. 4.9 Density of basal planes versus deviation angle from sheet normal direction (a) as-rolled (b) annealed.

A previous study related the texture weakening of cold-rolled Mg-Ce alloy to the formation of shear bands in the deformed structure [8]. This was linked to material within a shear band inclined from the basal pole. It has been also shown that heavily deformed shear bands are preferential nucleation sites for recrystallization of new grains having different orientations which can result in more random textures in some materials [32-34. Mackenzie and Pekguleryuz [19] observed higher density of shear bands in Mg-Zn containing Ce compared to Mg-Zn alloy. However, no link between texture weakening and the high density of shear bands was found. On the other hand, in Mg, such a random texture within the shear bands makes them more prone to slip deformation, especially via basal slip. Consequently, the grains within shear bands would soon gain a basal orientation (basal planes parallel to the sheet surface) upon further rolling. It is true that further deformation may also produce new shear bands where the recrystallized grains within the newly formed shear bands contribute to the final random texture. However, the volume fraction of newly generated shear band would not be to that extent that can explain the significant texture weakening which is observed in this study.

As was mentioned, the minimum texture intensity is achieved when the Ce amount reaches to 0.1wt.%, and the addition of more Ce does not have any more considerable effect on the texture. On the other hand, the solubility of Ce in Mg at rolling temperature of 400 ^{o}C, which applied in this study, is about 0.08wt.% [35]. Therefore it can be concluded that texture weakening is connected with the solid solubility of the Ce in Mg.

In HCP metals, the *c/a* ratio affects the difference in the critical resolved shear stress between basal slip and non-basal slips. The reduction of *c/a* can enhance the activity of the non-basal slips [23]. The *c/a* ratio of 1.624, as in Mg, results in low critical resolved shear stress on the basal plane favouring the basal slip. Ti on the other hand with a much lower *c/a* ratio (1.58) than Mg, has a high basal CRSS but low prismatic CRSS [23]. It has been reported that the addition of Ce to Mg [36-38] and Mg-Mn alloy [38] slightly reduces the *c/a* ratio (<0.001). However this slight reduction of *c/a* is not enough to activate non-basal slip [39].

The stacking fault energy is another factor which could affect the texture development during deformation. The stacking fault energy determines the extent to which unit dislocations dissociate into partial dislocations [31]. Solute atoms preferentially segregate to the stacking faults contained in extended dislocations. As the amount of the solute within the stacking fault increases, it lowers the stacking-fault energy and increases the separation of the partial dislocations [40]. A relationship between rolling textures of FCC materials with their stacking fault energy has been shown [41], i.e. Hirsch *et al.* showed that the addition of 5% and 37% zinc to copper alters the rolling texture which was related to stacking fault energy reduction of pure copper [41]. Alloying elements could change the stacking fault energy of Mg [42, 43], however, proper investigation of stacking fault energy in Mg is difficult [44]. Texture modeling and TEM studies indicate that Li and Y increases the glide of <*c* + *a*> dislocations on pyramidal planes in HCP α-Mg, where the role of Li and Y was attributed to the stability of partial dislocations of <*c* + *a*> [45]. The activation of different slip systems in Mg and Ti has been related to stacking fault energy [46]. Slip occurs preferentially on basal plane in Mg, but prismatic slip is preferred in Ti. For Mg the stacking fault energies in the basal plane is lower than in the prismatic plane, while in Ti the prismatic stacking fault energy is lower than the basal one [46]**.** As shown in Fig. 4.9, by addition of Ce to M1 alloy, the volume fraction of grains having the basal orientation decreases. This suggests that not only the basal slip, but also more non-basal slips were activated during the deformation of the ME alloys. Activation of the prismatic <*a*> slip in addition to the basal <*a*> slip has been also reported in the Mg–Ce alloy [44]. Therefore, it can be suggested that Ce addition affect the stacking fault energy of Mg and reduces the anisotropy of CRSS for different slip systems. As a result, other slip systems along with basal slip have been activated. More work is required to prove this hypothesis and to determine the effect of Ce on stacking fault energy of Mg.

4.1.4 Conclusions

This study has investigated the microstructure and texture of Mg-Mn-Ce in as-cast and rolled and annealed coditions.

1. As-cast M1 and ME alloy is characterized mainly by large columnar grains; however, the grains refine significantly by addition on Ce.
2. All alloys partially recrystallized during rolling. Shear bands and twins are observed in rolled structure.
3. Alloying had a minor effect on annealing grain size, suggesting that the second phase particles have a minor effect on grain growth.
4. The basal texture prevails in rolled and annealed sheet; however the addition of Ce significantly reduces the texture intensity.
5. Texture weaken was related to solid solubility of Ce in Mg.

4.1.5 References

1. T. Kaneko, M. Suzuki, , Mater. Sci. Forum, 2003, 419-422, pp. 67-72.
2. B. Engl, , Light Metal Age, 2005. 63(5) 14-19.
3. E. Baril, P. Labelle, M.O. Pekguleryuz, J. Metals (JOM-US), 2003. 55(11): pp. 34-39.
4. M. O. Pekguleryuz, A. A. Kaya, Adv. Eng. Mater., 2003. 5(12): pp. 866-878.
5. I.-H. Jung, W. Bang, I. J. Kim, , H. I.Sung, , W. J.Park,; D. Choo, , S. Ahn, , in: R. S. Beals (Ed.) Magnesium Technology. 2007 TMS Orlando, FL, USA, pp. 85-88.
6. F. Kaiser, J. Bohlen, D. Letzig, K.-U. Kainer, A. Sfyczynski, C. Hartig, Adv. Eng. Mater., 2003. 5(12): pp. 891-896.
7. A. Jager, P. Lukac, V. Gartnerova, J. Haloda, M. Dopita, Mater. Sci. and Eng. A 2006. 432: pp. 20–25.
8. M. R. Barnett, M. D. Navea, C. J. Bettlesb, Mater. Sci. Eng. A 2004. 386: pp. 205–211.
9. H. T. Jeong, T. K. Ha, J. Mater. Process. Technol. 2007. 187–188: pp. 559–561.
10. M.Yoo, Metall. Mater. Trans. A, 1981. 12(3): pp. 409-418.
11. J. Koike, T. Kobayashi, T. Mukai, H. Watanabe, M. Suzuki, K. Maruyama, K. Higashi, Acta Materialia, 2003. 51(7): pp. 2055-2065.
12. M. M. Avedesian, H. Baker, , Magnesium and Magnesium Alloys 1999: ASM International, Materials Park, OH 44073-0002, USA, . pp. 314.

13. E. Yukutake, J. Kaneko M. Sugamata, , J. Jpn Soc. Technol. Plast. 2003. 44: pp. 276-280.
14. J. Bohlen, M. R. Nürnberg, J. W. Senn, Letzig, D., S. R. Agnew, Acta Mater., 2007. 55(6): pp. 2101-2112.
15. M. Masoumi, F. Zarandi, M. Pekguleryuz, Scr. Mater., 2010, 62 (2010) pp. 823–826
16. M. Masoumi, F. Zarandi, M. Pekguleryuz, Mater. Sci. and Eng. A, 2010, corrected proof doi:10.1016/j.msea.2010.10.003
17. R. K. Mishra, A. K. Gupta, P. R. Rao, A. K. Sachdev, A. M. Kumar, A. A. Scr. Mater., 2008. 59(5): pp. 562-565.
18. N. Stanford, M. Barnett, Scr. Mater., 2008. 58(3): pp. 179-182.
19. L.W.F. Mackenzie, M. O. Pekguleryuz, Scr. Mater., 2008. 59(6): pp. 665-668.
20. E. A. Ball, P. B. Prangnell, Scr. Mater., 1994. 31(2): pp. 111-116.
21. L.W.F. Mackenzie, M. Pekguleryuz, Mater. Sci. Eng. A, 2008. 480(1-2): pp. 189-197.
22. E. F. Emley, Principles of Magnesium Technology. 1966, London: Pergamon Press.
23. G.V. Raynor, The Physical Metallurgy of Magnesium and its Alloys. 1959, New York: Pergamon Press.
24. H. E. Friedrich, B. L. Mordike, Magnesium technology : metallurgy, design data, applications 2006: Berlin ; New York : Springer, c2006.
25. P. Villars, L. D. Calvert; W. B. Pearson, Pearson's handbook of crystallographic data for intermetallic phases. 1985: Metals Park, Oh : American Society for Metals.
26. A. L. Greer, A. M. Bunn, A. Tronche, P. V. Evans, D. J. Bristow, Acta Mater., 2000. 48(11): pp. 2823-2835.
27. M. A. Easton, D. H. StJohn Acta Mater., Volume 49, Issue 10, 13 June 2001, pp. 1867-1878
28. X. Zhang, D. Kevorkov, I.-H. Jung, M. P. J. Alloys Compd., 482(1-2), 2009, pp. 420-428
29. w. Bulain, E. fahrenhorst , Metallography of Magnesium and its alloys. 1944: F. A. Hughes & Co limited abbey house London N.W.1.
30. L. W. F. MacKenzie, B. Davis, F. J. Humphreys, G. W. Lorimer, Mater. Sci.Technol., 2007. 23(10): pp. 1173-1180.

31. F. J. Humphreys, M. Hatherly, Recrystallization and Related Annealing Phenomena. 2 ed. 2004: Great Britain by Galliard Ltd., UK, .
32. H. Paul, J. H. Driver, Z. Jasienski, Acta Mater., 2002. 50(4):p p. 815-830.
33. X. Huang, K. Suzuki, A. Watazu, I. Shigematsu, N. Saito, J. Alloys Compd., 2008. 457(1-2): pp. 408-412.
34. N. Stanford, and M.R. Barnett, Mater. Sci. Eng. A, 2008, 496(1-2): pp.399-408
35. L. L. Rokhlin, Magnesium alloys containing rare earth metals : structure and properties. Vol. 3. 2003, London: Taylor & Francis
36. F. Hehmann, F. Sommer, B. Predel, Mater. Sci. Eng.A, 1990. 125(2): pp. 249-265.
37. R. S. Busk, J. of Metals, 1950. 188: pp. 1460-1464.
38. A. M.Becerra, Masters Thesis at McGill University, 2006.
39. T. Uesugi, M. Kohyama, K. Higasi, Mater. Sci. Forum,, 2003. 419-422: pp. 225-230.
40. G. E.Dieter, Mechanical Metallurgy. 1976, New York: McGraw-Hill.
41. J. Hirsch, K. Lücke, Acta Metall., 1988. 36(11): pp. 2863-2882.
42. K. Hirai, H. Somekawa, Y. Takigawa, K. Higashi, Scr. Mater., 2007. 56(3): pp. 237-240.
43. M. Suzuki, T. Kimura, J. Koike, K. Maruyama, Scr. Mater. 2003. 48(8): pp. 997-1002.
44. Y. Chino, M. Kado, M. Mabuchi, Mater. Sci. Eng. A, 2008. 494(1-2): pp. 343-349.
45. S. R. Agnew, M. H. Yoo, C. N. Tomé, Acta Metall., 2001. 49(20): pp. 4277-4289
46. P.B. Legrand, Philos. Mag. B, 1984. 49(2): pp. 171-184.

4.2 Effect of Sr on the texture of rolled Mg-Mn-based alloys *

*This section has been submitted as: **M.**, **Masoumi,** M., Pekguleryuz, "Effect of Sr on the texture of rolled Mg-Mn-based alloys" Scripta Materialia, August 2011.

Mg-1wt.%Mn-xwt.%Sr (MJ) alloys have been synthesized with Sr additions in the range of 0–1 wt.%. It was found that, compared to the Mg-1wt.%Mn (M1) alloy, the overall texture intensity of basal poles was weakened for rolled as well as rolled-annealed MJ alloys containing 0.5 and 1.0wt.%Sr. The texture weakening is attributed to particle-stimulated nucleation (PSN) that leads to the formation of new grains in the vicinity of second phase particles, with different orientations to that of the deformed matrix.

4.2.1 Introduction

Automotive applications of magnesium (Mg) sheets have received significant attention for the purpose of vehicle weight-reduction. Mg sheet alloys are commercially produced by hot rolling of direct-chill (DC) cast ingots. Rolling orients the {0001} basal planes of the hexagonal closed packed (HCP) Mg crystals parallel to the sheet surface [1,2], leading to preferred orientation known as basal texture. The possibility to enhance the formability of Mg alloys by weakening the basal texture has already been verified [3, 4]. Therefore, considerable effort is currently being conducted to weaken the basal texture or to attain a random texture in rolled Mg sheet by modifying existing alloys or developing new alloys [4, 7]. Non-basal or weak textures have been reported in Mg-RE (RE: rare earth elements) alloys [4-6] and in Mg alloys with low levels of Li [7].

Strontium (Sr) has been used in Mg alloys as an alloying element for different purposes. Sr has been added to Mg-Al alloys to improve the creep resistance [8]. Sr at 0.2wt.% has been used in the AZ80 forging alloy to grain refine and improve forgeability [9]. However, the effect of Sr on the texture of rolled Mg sheet alloys has not been previously studied. This paper discusses the basal-texture weakening of M1 alloy, which has been used as sheet material [10], via Sr alloying. This is part of a larger investigation which aims to develop alternative Mg alloys for sheet and twin-roll casting processes [5-7, 11, 12].

4.2.2 Experimental Procedure

A 125mm×100mm×6mm plate of each MJ alloy was cast into a tool steel mould preheated at 400 ^{o}C. The chemical analysis of the alloy samples taken from the as-cast plates is presented in table 1. AZ31 alloy (Mg-3wt.%Al-0.9wt.%Zn-0.6wt.%Mn)was used as a benchmark. Plate specimens 40mm×40mm×6mm were machined from the cast material and homogenized for 8 h at 450 ^{o}C.

Table 4.3 composition of alloys used in this study

Alloy	Alloy Symbol	Mn (wt.%)	Sr (wt.%)
Mg-1%Mn	M1	1.08	<0.001
Mg-1%Mn-0.2%Sr	MJ10(0.2Sr)	0.94	0.17
Mg-1%Mn-0.5%Sr	MJ1(0.5Sr)	0.92	0.48
Mg-1%Mn-1.0%Sr	MJ11(1.0Sr)	0.94	1.02

The thickness of the homogenized plate samples was reduced to 1.4 mm through seven rolling passes, with equal reductions of about 0.65 mm for each pass, using a laboratory-scale Stanat rolling mill. The rolling specimen was preheated at 400 ^{o}C for 15 minutes before the first rolling pass and for 5 minutes before each subsequent pass. The rolled sheet samples were then annealed at 450 ^{o}C for 15 minutes after the last rolling pass. Specimens for microstructural examination were taken from the sheet thickness; i.e. the plane of rolling and sheet normal directions (RD-ND), and were prepared by conventional grinding and polishing and then etched with acetic-picral. The microstructure was studied using both optical microscopy and scanning electron microscopy (SEM).

The overall texture was evaluated by X-ray diffraction (XRD) using a Bruker D8 X-ray diffractometer. Recalculated pole figures were constructed using the texture analysis software, TexTools. Grain orientation was studied via electron-back scattered diffraction (EBSD) using a Phillips XL30 SEM at 20 kV and 70^{o} tilt angle.

4.2.3 Results and Discussions

Figs. 4.10a-c present the as-rolled microstructure of AZ31, M1 and MJ11(0.5Sr) alloys. The AZ31 alloy (Fig. 4.10a) has a deformed structure (with the presence of twining and shear bands), however it seems the sheet partially recrystallized following rolling at 400 ^{o}C. The shear bands appear as dark strings as they contain very fine grains inside the bands. The microstructure of Mg-Mn alloys was analyzed using EBSD since the optical microscopy of these alloys in the deformed (i.e. rolled and forged) state was difficult to achieve due to the poor response of these alloys to etching [13], even when a variety of ethchants was used. The microstructures of selected specimens in the rolled condition are shown in Figs. 4.10 b&c. In these two figures, the high angle boundaries (HAB) (>15^{o}) and low angle boundaries (LAB) (>3^{o}) are delineated with black and white lines, respectively. Both alloys (M1 & MJ11(0.5Sr)), despite having deformed structures (presence of low angle boundaries), are also partially recrystallized following rolling at 400 ^{o}C. Twins can also be observed in as-rolled structure of both alloys. The microstructures of the AZ31, M1 and MJ alloys after annealing at 450 ^{o}C for 15 min are shown in Figs. 4.11 a-e**.** The AZ31 sheet exhibits heterogeneous grain size distribution with a mixture of large and small grains. While the average grain size was 9 μm, there were grains as large 30 μm and as small as 4μm. The grain size of the rolled-annealed MJ alloys decreases slightly from ~13 to ~8 μm with an increase in the Sr content (from 0 to 1 wt.%). During the rolling of the MJ alloys, the coarse second-phase particles of the cast structure were broken up into smaller fragmented particles, which were aligned parallel to the RD (the direction of material flow). The area fraction of second phases, f_{sp}, increases from 1.5% to 5.4% with increasing Sr content from 0 to 1 wt.%. The SEM/WDS (Wavelength Dispersive Spectroscopy) analyses of M1 revealed that the matrix was α-Mg (Mg-Mn solid solution), and the second phases particles were Mg-Si (Mg_2Si) and Mn-Si phases, which could be either Mn_9Si_2, or Mn_6Si [14]. The SEM/WDS analyses of MJ11(0.5Sr) also reveals that the matrix was α-Mg and the particles were a mixture of Mg-Sr and Sr-Si, most likely to be $Mg_{17}Sr_2$ and Sr_3Si_5 [14].

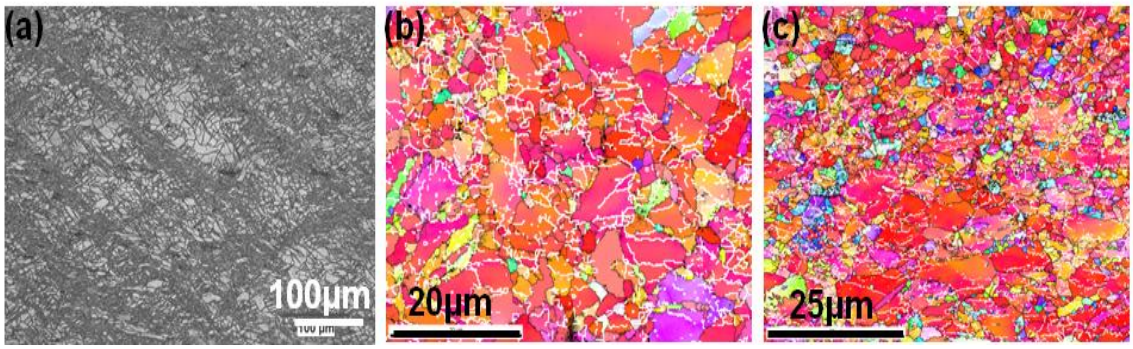

Fig. 4.10 *(a) as-rolled Microstructures of AZ31. EBSD maps from the RD-ND plane of the as-rolled at 400 ^{o}C: (b) M1 alloy (c) MJ11(0.5Sr) .*

The texture of specimens following rolling at 400 ^{o}C are shown in Figs. 4.12 a-e. In all alloys the basal planes are aligned parallel to the sheet surface presenting a basal texture. The basal texture intensity of the AZ31 alloy was 4.6 multiples of a random distribution (MRD) (Fig. 4.12a). This texture is typical of conventional AZ31B sheet [1,2]. The M1 alloy exhibited a strong basal texture, having the intensity of more than 8 MRD. It seems that the addition of a small amount of Sr (0.2 wt.%) to the M1 alloy did not have any significant effect on the texture of M1 alloy. However, the addition of Sr, in excess of 0.5wt.%, to the M1 alloy had a significant texture weakening effect, as indicated by the lower peak intensity. The addition of 0.5 wt.%Sr and 1 wt.%Sr reduced the texture intensity to approximately one half and one-third of the M1 alloy respectively (the texture intensity of rolled MJ11 alloys is even weaker than that of AZ31 alloy). Additionally, Sr alloying broadens the angular distribution of basal poles, both in RD and TD. The texture contour broadens from 33° in M1 alloy towards 42° by the addition of 1 wt% Sr. Annealing at 450 ^{o}C for 15 minutes had a minor effect on the texture of the alloys; the maximum intensity decreased but the general features of the pole figure did not alter (Figs. 4.12 f-j).

In order to better quantify the distribution of basal planes, the percentage of basal planes versus the angle of deviation from the sheet ND were plotted both in as-rolled and annealed conditions (Fig. 4.12 k&l). As shown, the addition of Sr reorientated the basal

planes away from the sheet ND when compared with the M1 alloy. In other words, the percentage of basal planes that have an orientation away from the ND increased.

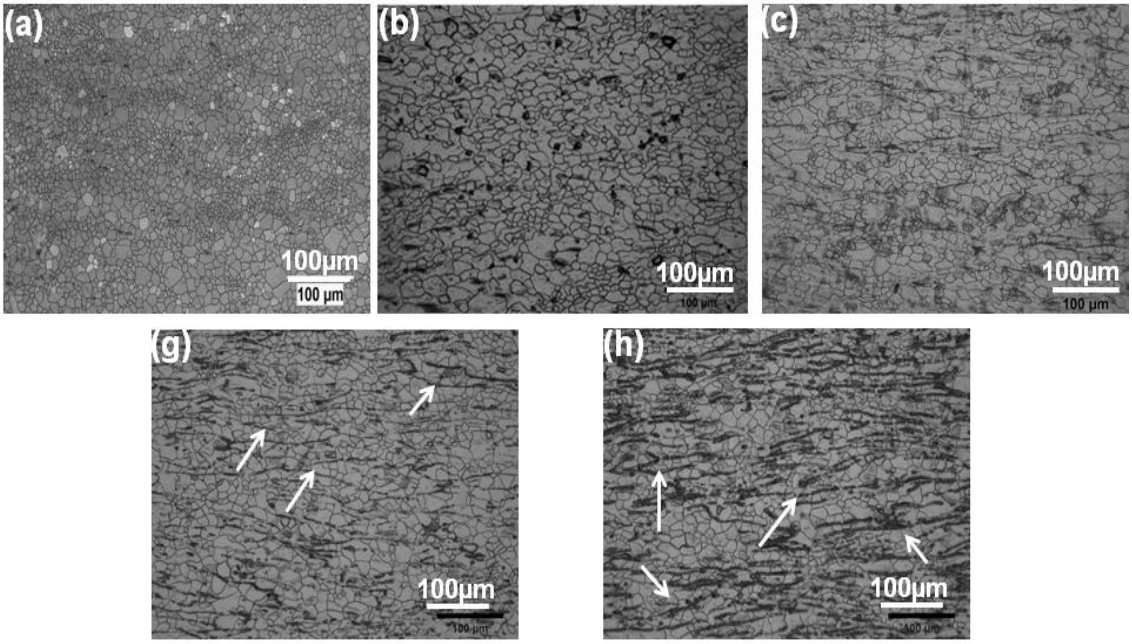

Fig. 4.11 Microstructures of the alloys in the rolled-annealedcondition (d) AZ31 (e) M1 (f) MJ10(0.2Sr) (g) MJ11(0.5Sr) (h) MJ11(1.0Sr).

It is well known that gliding dislocations do not shear non-coherent precipitates. As a result, dislocation pile-up or looping at the particle-matrix interface occurs [18,19]. The polarity of the tension-compression strain fields of these dislocations leads to lattice rotations in the vicinity of the precipitate-matrix interface [18,19]. Local strain accumulation is relieved by the formation of cell and sub-grain formation upon annealing. When recrystalization is assisted by particles, the mechanism is known as particle-stimulated nucleation (PSN) [19]. The sub-grains that form during the recovery stage coalesce through rotation according to the five-degrees of freedom of low-angle boundaries (tilt, twist, rotation) and nucleate into new grains with substantially different orientations than that of the parent grain, hence, PSN offers a way to alter or weaken the texture [18-20].

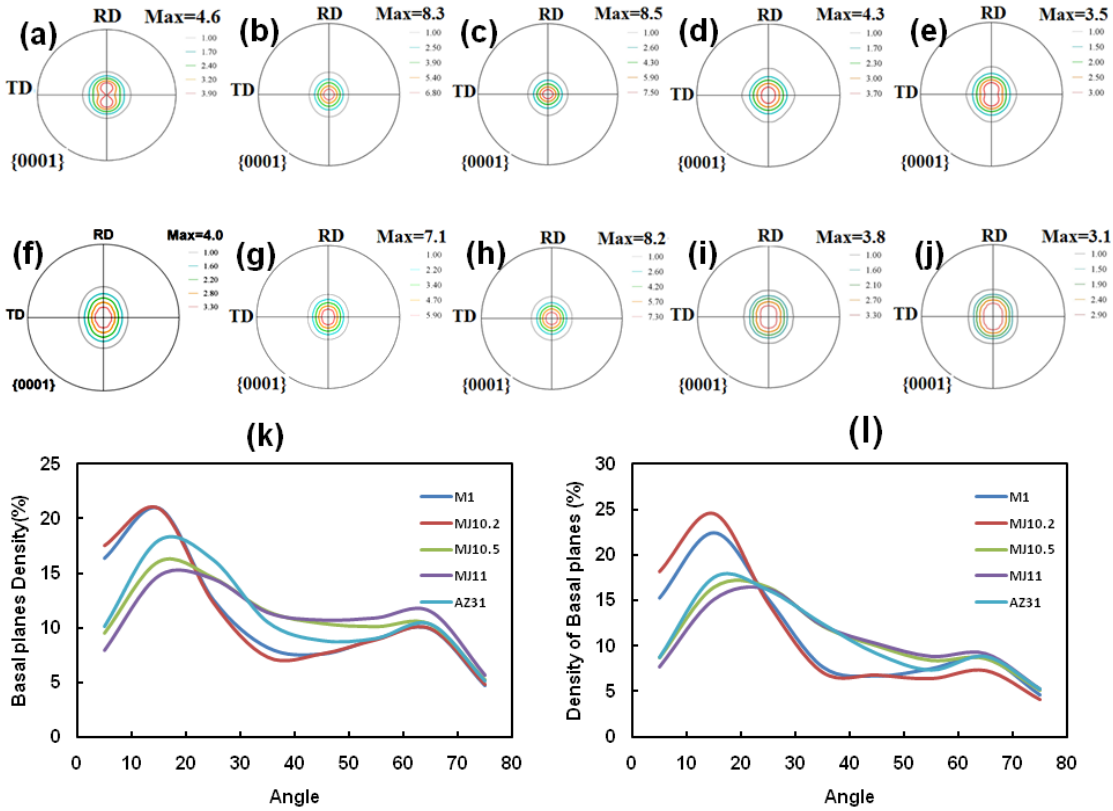

Fig. 4.12 Surface texture pole figures of alloys, rolled at 400 °C (a) AZ31 (b) M1 (c) MJ10(0.2Sr) (d) MJ11(0.5Sr) (e) MJ11(1.0Sr), annealed at 450 °C for 15 min: (f) M1 (g) MJ10(0.2Sr) (h) MJ11(0.5Sr) (j)MJ11(1.0Sr). Density of basal planes versus deviation angle from sheet normal direction (k) as-rolled and (i) annealed.

Generally it was thought that recrystallization textures do not significantly change in Mg alloys. However, recent studies have related texture weakening in Mg alloys to PSN [11, 12, 21, 22]. Also, it has been shown that during static recrystallization, stringers of second phases are more effective than dispersed particles in taking part in PSN, where particle stringers act successfully as one very large particle since they can create a shared deformation zone [18, 19]. Since Sr produces second phases which are thermally stable at the rolling temperature (400 °C), and their amount increases with increasing Sr (which increases the potential sites for PSN), it is concluded that the second phases may have led to PSN in MJ alloys causing texture weakening. Indeed, it can be observed that there is a close association between some of the recrystallized grains and the stringers (shown by

white arrow in Figs. 4.11 d&e). In these areas, the recrystallized grains have grown until they impinged upon another row of stringers or newly recrystallized grains.

To verify the interaction of the particles with the recrystallized grains, EBSD analysis was performed on MJ11(0.5Sr) annealed at 450 ^{o}C for 4 min, i.e., a duration that is not sufficiently long to attain a fully recrystallized structure (Figs. 4.13 a&b). Fig. 4.13b is the magnified view of the area indicated by the white square in Fig. 4.13a. Some small recrystallized grains, with little or no deformation sub-structure typical of strain-free recrystallized grains, associated with stringer were observed (Fig. 4.13a).

As explained earlier, in order for a particle/stringer to stimulate recrsytallization nucleation, a misoreintaion gradient towards particles is necessary [18, 19]. To verify this, a linescan analysis was carried out to estimate the misorientation (relative to the starting orientation) in grain B in the direction of the line marked CD (Fig 4.13c). It was found that that there was a continuous increase in misorientation towards the stringer, corresponding to a lattice rotation relative to the starting point (which is required for the formation of a new HAB [18]). Figs 4.13 d&e show the pole figures of grains A&B in Fig. 4.13b (representing the deformed matrix) and the recrystallized grains next to stringer. As seen in Fig. 4.13c, the deformed grains show a near basal texture, whereas the recrystallized grains next to stringer (Fig 4.13e) show a much wider spread of orientations. This confirmed that the new recrystallized grains assisted by PSN had a different orientation which contributed to the texture weakening. It should be noted that some of the recrystallized grains are adjacent to high angle boundaries and are likely to have nucleated through the grain boundary bulging mechanism. These grains have orientations very similar to those of the parent grains (shown in Fig 4.13b with white circle). Therefore we conclude that the nucleation of new grains in the MJ alloys was associated with both grain boundary bulging and second phase particles, and that the latter leads to texture weakening.

This study confirms for the first time that Sr can be used as an alloying element to weaken the texture of Mg sheet alloy M1. Such texture weakening of Mg sheet is very important as it promises improved sheet formability [3], which is highly significant for the automotive industry.

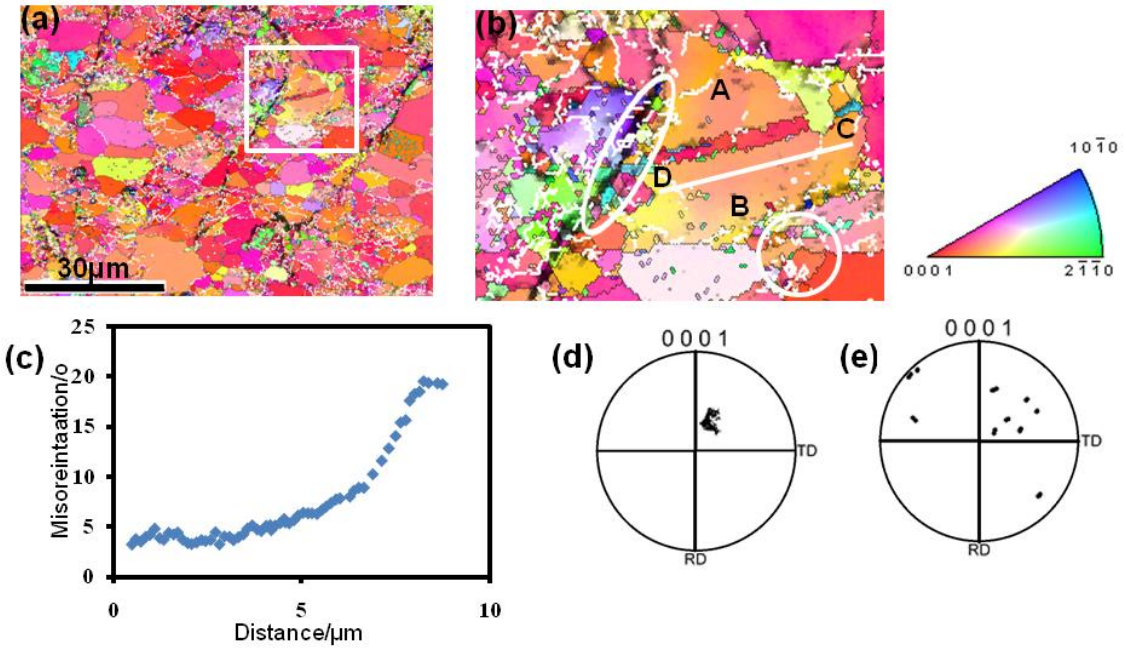

Fig.4.13 The MJ11(0.5Sr) after annealing for 4 min at 450 °C: (a) EBSD map on the RD–TD plane and (b) magnified area in the white square c) misorientation gradient along the CD direction shown in Fig4.13b d) texture pole figure of grain A and B e) texture pole figure of fine grain close to stringer.

4.2.4 References

1- F. Kaiser, J. Bohlen, D. Letzig, K.-U. Kainer, A. Sfyczynski, C. Hartig, Adv. Eng. Mater., 2003. 5(12): pp. 891-896.

2- M.R. Barnett, M.D. Navea, C.J. Bettlesb, Mater. Sci. Eng. A 2004. 386: pp. 205–211.

3- E. Yukutake, J. Kaneko M. Sugamata, , J. Jpn Soc. Technol. Plast. 2003. 44: pp. 276-280.

4- J. Bohlen, M.R. Nürnberg, J.W. Senn, Letzig, D., S.R. Agnew, Acta Mater., 2007. 55(6): pp. 2101-2112.

5- L.W.F. Mackenzie, M.O. Pekguleryuz, Scr. Mater., 2008. 59(6):p p. 665-668.

6- M. Masoumi, M. Hoseini, M. Pekguleryuz, Mater. Sci. & Eng. A, 2011, 528, (7-8): pp. 3122-3129.

7- L.W.F. Mackenzie, M. Pekguleryuz, Mater. Sci. Eng. A, 2008. 480(1-2): pp. 189-197.

8- E. Baril, P. Labelle, M.O. Pekguleryuz, J. Metals (JOM-US), TMS, Nov 2003, pp. 34-39.

9- M. Fujita, N. Sakate, S. Hirahara, Y. Yamamoto, SAE Paper 950422. 1995 doi:10.4271/950422.

10- E.F. Emley, Principles of Magnesium Technology. 1966, London: Pergamon Press.

11- M. Masoumi, F. Zarandi, M. Pekguleryuz, Scr. Mater., 2010, 62 (2010), pp. 823–826

12- M. Masoumi, F. Zarandi, M. Pekguleryuz, Mater. Sci. and Eng. A, 2011, 528 (3), pp. 1268-1279

13- W. Bulain and E. Fahrenhorst, Metallography of Magnesium and its Alloys, F. A. Hughes & Co Limited Abbey House, London, N.W.I. (1944).

14- A. A. Nayeb-Hashemi, J.B. Clark, Bulletin of alloy phase diagrams. Vol. 1-2. 1986.

15- P. Villars, L.D. Calvert and W.B. Pearson, Pearson's Handbook of Crystallographic Data for Intermetallic Phases, American Society for Metals, Metals Park, OH (1985)

16- K. Hantzsche, J. Bohlen, J. Wendt, K.U. Kainer, S.B. Yi, D., Letzig, Scr. Mater., 2010. 63(7): pp. 725-730.

17- G.T. Higgins, J. Nucl. Mater. 8 (1963), pp. 153.

18- F.J. Humphreys and M. Hatherly, Recrystallization and Related Annealing Phenomena (2nd ed.), Great Britain by Galliard Ltd., UK (2004).

19- L.W.F. MacKenzie, B. Davis, F.J. Humphreys and G.W. Lorimer, Mater. Sci. Technol. 23 (10) (2007), pp. 1173–1180.

20- R.E. Reed-Hill, R. Abbaschian, Physical Metallurgy Principles, third ed., PWS, Boston, MA.

21- F.J., Humphreys, Acta Metall., 1977. 25(11): pp. 1323-1344.

22- E.A. Ball and P.B. Prangnell, Scr. Mater. 31 (2) (1994), pp. 111–116.

4.3 The influence of Sr on the Microstructure and Texture Evolution of Rolled Mg-1%Zn Alloy *

*This section has been accepted to be published: **M. Masoumi,** M. Pekguleryuz, "The influence of Sr on the Microstructure and Texture Evolution of Rolled Mg-1%Zn Alloy" Accepted for publication in Materials Science and Engineering: A.

In this study, the microstructure and texture of rolled and rolled-annealed alloys based on Mg-1wt.%Zn and containing various levels of Sr (from 0.1 to 1.0 wt.%) were investigated. The Sr addition refined the as-cast rolled-annealed grain structure of the Mg-1wt.%Zn alloy. The grain refining effect of Sr was more pronounced at lower levels of Sr addition. The as-rolled Z1 and ZJ alloys exhibited heavily deformed structures. The density of shear bands in as-rolled alloys appears to decrease with an increase in the Sr content. Also, the overall texture intensity of basal poles was weakened for rolled as well as rolled-annealed Mg-Zn-Sr (ZJ) alloys compared to the Mg-1wt.%Zn (Z1) alloy. It was also observed that Sr additions expanded the basal poles in the transverse direction. Texture weakening was attributed to the particle stimulated nucleation (PSN) mechanism.

4.3.1 Introduction

Since the early 1990s, automotive applications of Mg alloys have received considerable interest for vehicle weight-reduction. To date, the application of Mg alloys in cars has been limited to die-cast parts such as steering-wheel cores, brake-pedal brackets, instrument panels, transmission cases and engine blocks [1-3]. Recently, heightened interest in using Mg sheet for automotive-body applications has highlighted the importance of Mg sheet alloys.

The major shortcomings of Mg sheet alloys are the high cost and limited formability [4, 5]. The latter is due to the hexagonal close-packed (HCP) structure of Mg, which offers limited active slip systems at moderate temperatures. The rolling of magnesium wrought alloys orients the {0001} basal planes of the HCP Mg parallel to the sheet surface [6-8]. This preferred orientation, known as the "basal texture", further contributes to the poor formability and as a consequence considerably limits the variety

of components which can be manufactured from Mg sheet. The possibility to enhance the formability of magnesium alloys by texture weakening has been reported [9]. It was shown that the *r*-value (Lankford coefficient), deep drawing and stretch forming of the commercial AZ31 (Mg-3wt.%Al-1wt.%Zn) alloy is strongly affected by texture variation [9]. Therefore, considerable effort is currently being directed to obtain random or weakened texture in magnesium sheet alloys by modifying existing alloys or developing new alloys [10-12]. Non-basal or weak textures have been reported in Mg-RE (RE: rare earth elements) alloys [11-15], annealed twin roll cast AZ31 [16, 17] and Mg alloys with low levels of Li [10]. Mackenzie and Pekguleryuz investigated the effect of Ce on the texture of rolled Mg-Zn alloys [11]. The deformation texture of Mg-Zn alloys was found to be similar to that of conventional Mg alloys. However, the addition of a small amount of cerium significantly weakened the texture. Additionally, it was reported that the basal poles were broadened towards the transverse direction (TD) and the (0002) peaks were ~45^{o} away from sheet normal direction (ND) [11]. The authors also observed further basal texture weakening after subsequent annealing. The authors did not observe any evidence of PSN, and therefore concluded that a form of "solute drag" might be responsible for texture weakening [11]. Bohlen *et al* [12] studied the effect of RE elements on the texture of Zn based alloys with 1 wt% and 4 wt% additions of Zn. ZM21 (Mg-2wt.%Zn-1wt.%Mn) and ZK10 (Mg-1.5wt.%Zn-0.4wt.%Zr) alloys were also investigated as benchmarks. ZM21 and ZK10 showed the strongest basal texture, with 8 multiples of a random distribution (MRD) while other alloys containing RE showed weaker basal texture (about 4 MRD) [12]. The authors could not relate the texture weakening to higher amount of second phases in Mg alloys containing RE as the same amount of intermetallic phases (but different intermetallics types) observed in ZM21 and ZK10. It was hypothesized that soluble Zn and RE additions were responsible for modification of rolling texture [12].

Strontium (Sr) has been used in Mg alloys as an alloying element for different purposes. Sr has been shown to reduce the grain size of Mg alloys containing Al [18]. Sr is also an effective grain refiner of Mg alloys, since it acts as a growth-poisoner, and also prevents abnormal grain growth [19]. Sr at 0.2% has been used in the AZ80 forging alloy

to grain refine and improve the forgeability of the alloy [20]. However, to date, the effect of the Sr on the texture evolution of Mg alloys during rolling and subsequent annealing has not been investigated.

This paper reports the effects of Sr on the microstructure and the texture of Mg-Zn alloy sheet. Unmodified AZ31 alloy microstructures and textures are also presented for comparison. This is part of a larger investigation, which aims at developing alternative Mg alloys for sheet and twin-roll casting processes [10, 11, 16, 17].

4.3.2 Experimental Procedure

Alloys were prepared in a Norax Canada induction furnace (20 KW, 5 KHZ) and a graphite crucible. Pure Zn (99.99wt.%, supplied by Alfa Aesar) and pure Sr (99.5wt.%, supplied by ELKEM) were added to molten Mg (99.5wt.%, supplied by MEL), under a protective gas mixture of sulphur hexafluoride, SF_6, and carbon dioxide, CO_2 (as a carrier gas). The melt temperature was monitored via a K-type (chromel-alumel) thermocouple. The molten alloys were poured from a casting temperature of 720 ^oC into a tool-steel mould preheated at 400 ^oC to produce plate castings 125mm × 100mm × 6mm. Commercial AZ31B supplied by Timminco (now Applied Magnesium) was also cast as a control alloy. The chemical compositions of the alloy samples taken from the plates are given in Table 4.4. Note that the alloy designations are given according to the ASTM alloy standards for magnesium alloys where Z=zinc and J=strontium. The castings were homogenized in a SPX Blue M electric furnace for 8 h at 400 ^oC. Test specimens 40mm × 40mm × 6mm were machined from the homogenized castings.

The homogenized samples were reduced to 1.4 mm thickness through seven rolling passes, with equal reduction of about 0.65 mm in each pass, using a laboratory-scale Stanat rolling mill. The total reduction ratio was 75%. Rolling started with an initial reduction ratio of about 10% and the final reduction ratio was about 30%. Specimens were preheated at 400 ^oC for 15 minutes prior to the first rolling pass and for 5 minutes before the following passes. Samples were finally annealed at 400 ^oC for 5 minutes after the last rolling pass.

Table 4.4 Chemical Composition of the Alloys

Alloy*	Mn	Sr	Zn	Si	Al
Z1	0.001	<0.001	1.0	0.1	0.010
ZJ10 (0.1Sr)	0.001	0.12	1.0	0.1	
ZJ10(0.3Sr)	0.001	0.27	1.05	0.04	0.010
ZJ11(0.5Sr)	0.001	0.49	0.98	0.1	0.010
ZJ11 (1.0Sr)	0.001	0.91	0.97	0.1	0.010
AZ31	0.67	-	0.89	0.02	3.0

*Z=Zn; J=Sr; A=Al

Specimens for microstructural examination were taken from the thickness side; i.e. the plane of rolling and sheet normal directions (RD-ND). They were prepared by grinding on SiC paper, polished with diamond paste and etched in acetic-picral. The microstructure was studied using conventional optical microscopy, electron probe micro-analysis (EPMA - JEOL 8900) and scanning electron microscopy (SEM) with a resolution of 70 nm.

The overall crystallographic orientation was evaluated by X-ray diffraction (XRD) using a Bruker D8 X-ray diffractometer using Co Kα radiation. Incomplete pole figures of {0001}, $\{10\bar{1}0\}$ and $\{10\bar{1}1\}$ were recorded, and the orientation distribution function (ODF) was constructed using TexTools texture-analysis software. Recalculated pole figures were derived from the ODFs. The XRD specimens were ground successively to remove almost 10% of the sheet thickness and then polished with 1 μm diamond slurry. They were then chemically polished in 10% nital solution for 60 seconds to eliminate any residual stress on the surface. The grain orientation was also studied using the electron back scattered diffraction (EBSD) method in a SEM at 20 kV accelerating voltage and 70^{o} tilt angle. The EBSD specimens, after polishing with 1 μm diamond slurry, were electropolished using a solution 10% nital cooled to 0 ^{o}C at 20 V.

4.3.3 Results and Discussion

4.3.3.1 As-cast Microstructures

AZ31 Alloy

The AZ31 alloy in the as-cast condition shows an equiaxed grain structure with an average grain size of 105 μm (Fig. 4.14a). Second phases were observed both in the matrix and in the grain boundaries. Previously, it has been shown that the AZ31 alloy contains α-Mg matrix (with dissolved Al, Zn and Mn) and two different second phases: (i) $(Al,Zn)_{49}Mg_{32}$ phase [18] and (ii) Al-Mn precipitates which could be a mixture of $Al_{11}Mn_4$, Al_8Mn_5, Al_9Mn_{11} and β-Mn(Al) intermetallics [21].

Z1 & ZJ Alloys

The as-cast grain structure of Z1 alloy was refined following the addition of Sr (Figs. 4.14 b-f). The Z1 alloy has a relatively coarse equiaxed grain structure with an average grain size of ~280 μm. A mixture of coarse and relatively fine semi-equiaxed grains was observed in all ZJ alloys. The average grain size of the Z1 alloy decreased from ~280 μm to ~150 μm following the addition of 0.1 wt.% Sr. As the Sr level increased from 0.1 wt.% to 1.0 wt.%, the grain size reduced slightly from~150 μm to ~120 μm. A similar grain refining effect of Sr in Mg-Al alloys has previously been reported [22-24]. Sr additions at ~ 0.02 wt% gave the optimum grain refining effect in Mg-Al alloys [24]. Sr, being surface active in Mg, acts as a growth poisoner and also prevents abnormal grain growth [19].

Second phases with a plate-like morphology and round shape were observed in Z1 and all ZJ alloys, both in the matrix and at the grain boundaries. The SEM/WDS (wavelength dispersive spectroscopy) analyses of Z1 and ZJ10(0.5) alloys are shown in Figs. 4.15, which indicate that the matrix of Z1 is α-Mg (Mg-Zn solid solution), and the precipitates are Mg-Zn and Mg-Si phases, which could be $MgZn_2$ and Mg_2Si, respectively [25]. The matrix of ZJ11(0.5Sr) is α-Mg (Mg-Zn solid solution) and particles are Zn-Sr-Si, Sr-Si and Zn-Sr which could be $SrZn_5$, SrSi and Sr_5Si_3 [25]. The area fraction of the second phases, f_{sp}, in ZJ alloys was determined by image analysis: as Sr increases from 0 to 1.0 wt.%, the f_{sp} increases from ~1.5% to ~4.5%.

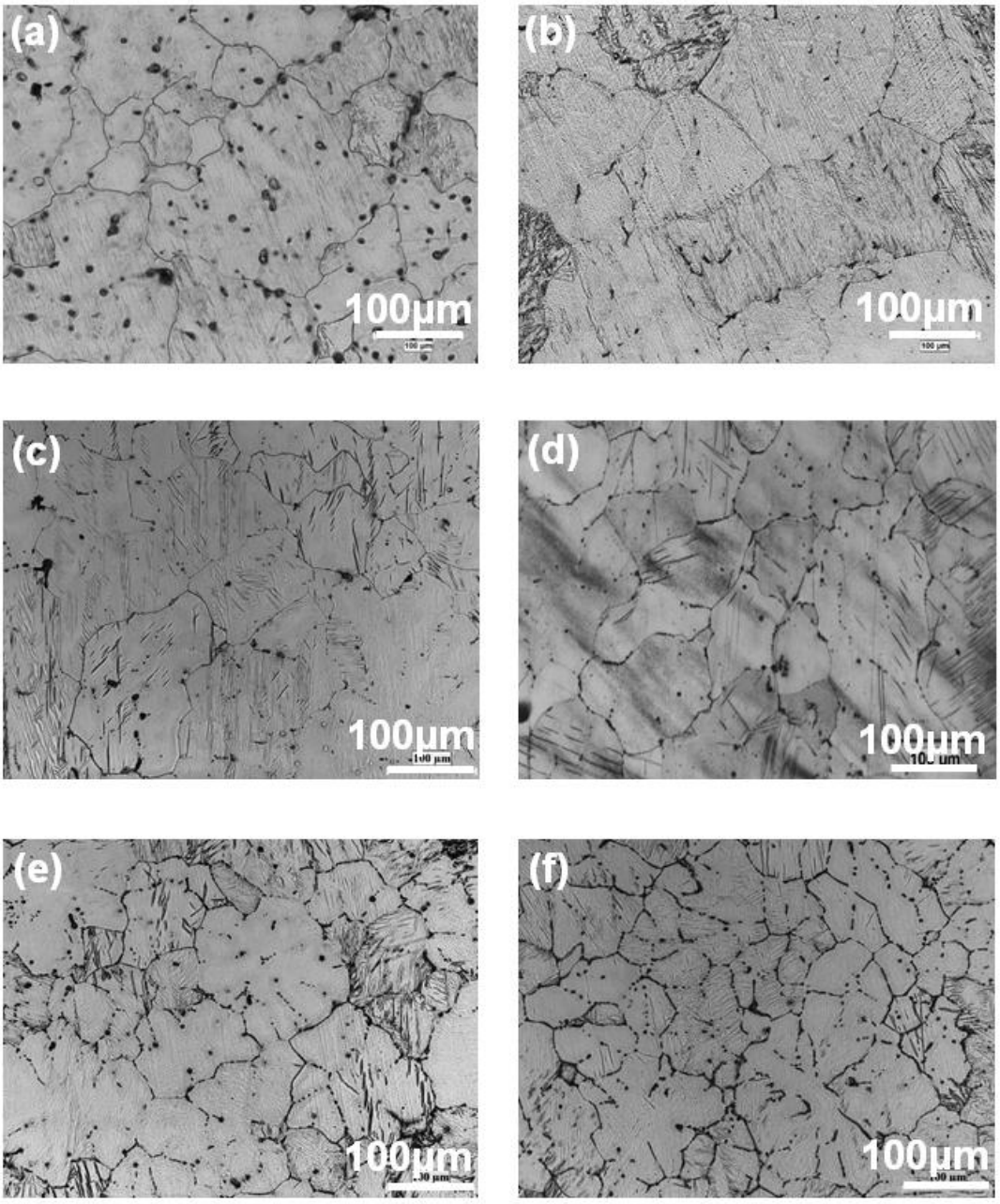

Fig.4.14 As-cast microstructure of (a) AZ31 (b) Z1 (c) ZJ10(0.1Sr) (d) ZJ10(0.3Sr) (e) ZJ11(0.5Sr) (f) ZJ11 (1.0Sr).

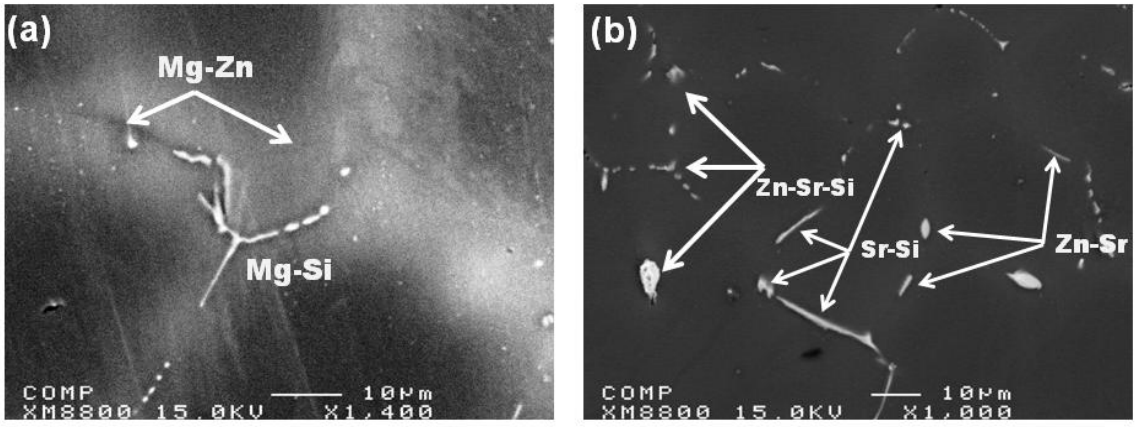

Fig.4.15 SEM micrograph showing second phase particles (a) Z1 (b) ZJ11(0.5Sr).

4.3.3.2 Microstructures of rolled and rolled-annealed alloys

The microstructures of hot rolled sheets at 400 ^{o}C are shown in Figs. 4.16 a-f. AZ31 alloy (Fig. 4.16a) had a deformed structure (with the presence of twining and shear bands), however, the sheet appeared to partially recrystallize following rolling at 400 ^{o}C. The shear bands appeared as dark strings since they contained very fine grains inside the bands. Shear bands corresponded to narrow regions of intense shear, which have previously been observed in rolled materials, at an angle of about 35^{o} to the rolling plane and parallel to the transverse direction [26]. The as-rolled Z1 and ZJ alloys (3 b-f) exhibited heavily deformed structures. The density of shear bands appeared to be less in Z1 and ZJ alloys compared to AZ31, and decreased with an increase in the Sr content, particularly above 0.3 wt.%Sr.

Microstructures of annealed samples are shown in Figs. 4.17 a-f. All specimens were nearly fully recrystallized following annealing for 5 min at 400 ^{o}C. AZ31 sheet exhibited a non-uniform recrystallization structure with characteristic shear bands with very fine grains inside the shear bands. The bimodal microstructure was clearly observed. The microstructures of annealed Z1 and ZJ alloys exhibited a recrystallized grain structure comprised of small equiaxed grains with no evidence of abnormal growth or other grain size inhomogeneities.

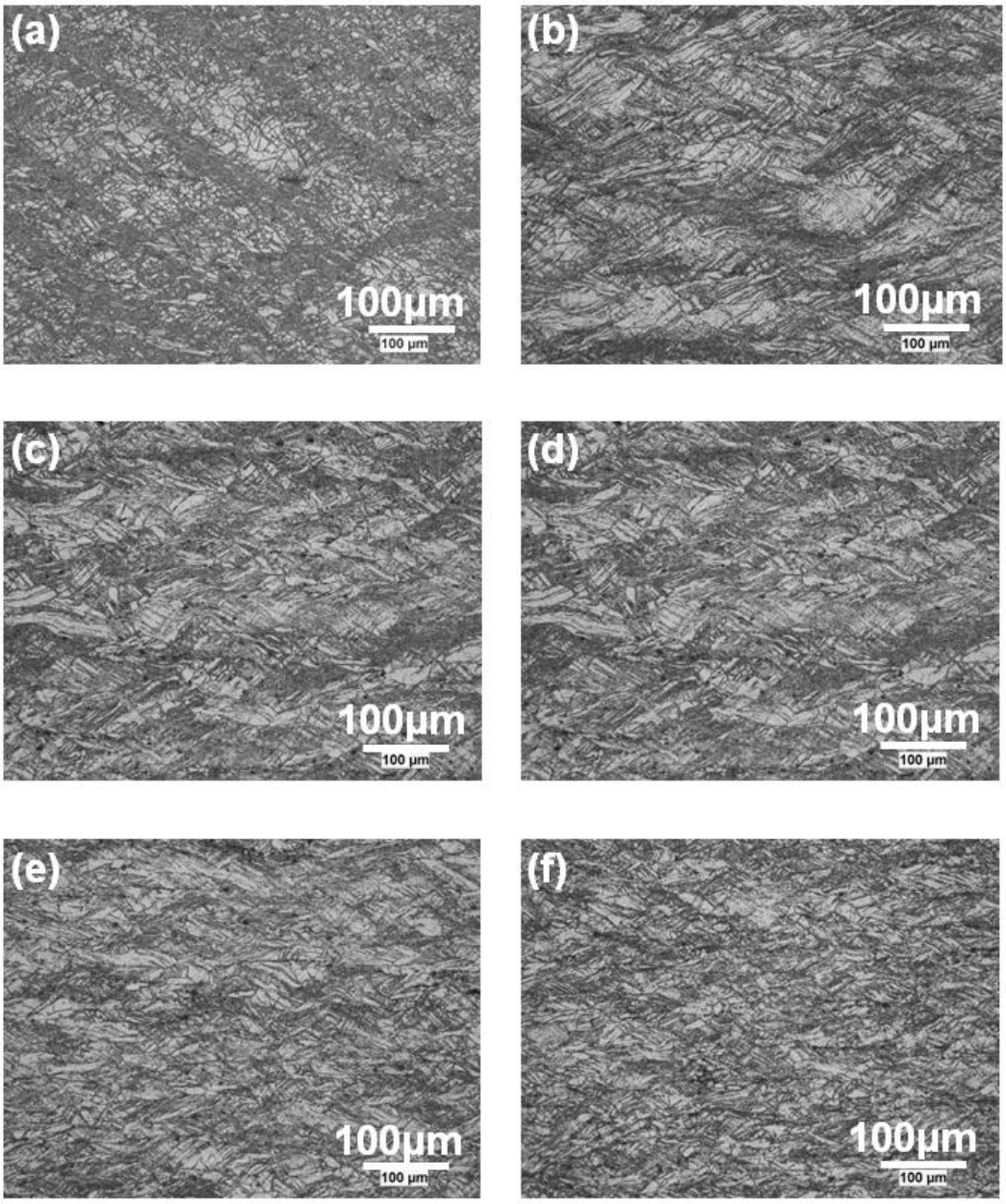

Fig. 4.16 Microstructures of the alloys in the rolled condition (a) AZ31, (b) Z1 (c) ZJ10(0.1Sr), (d) ZJ10(0.3Sr), (e) ZJ11(0.5Sr) and (f) ZJ11(1.0Sr).

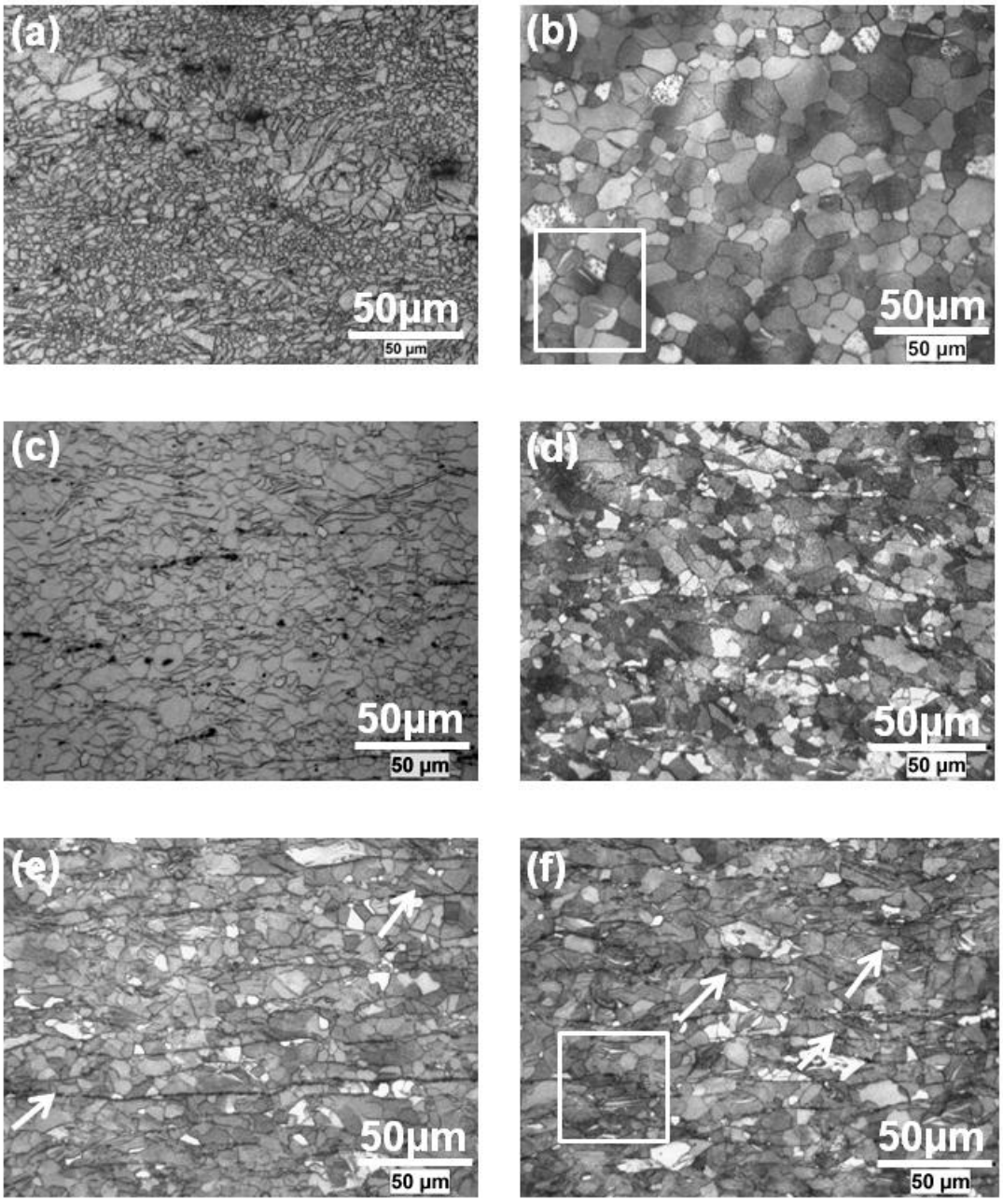

Fig. 4.17 Microstructures of the alloys in the rolled-annealedcondition (a) AZ31, (b) Z1(c) ZJ10(0.1Sr), (d) ZJ10(0.3Sr), (e) ZJ11(0.5Sr) and (f) ZJ11(1.0Sr).

During the rolling of the ZJ alloys, the coarse second-phase particles of the cast structure are broken up into smaller fragmented particles, which are aligned parallel to the rolling axis (the direction of material flow). The grain size of the rolled-annealedZJ alloys has decreased slightly from ~11 to ~6 μm with an increase in the Sr content (from 0 to 1wt.%). The finer grain size of ZJ alloys compared to Z1 alloy is likely due to the pinning effect of second phases [26]. The grain structures of ZJ alloys are more homogeneous than AZ31. The SEM/WDS analyses of rolled ZJ11(0.5) alloys reveal that the matrix is α-Mg (Mg-Zn solid solution), and the second phase particles are Sr-Si compounds which could be SrSi and Sr_5Si_3 [25].

4.3.3.3 Texture of rolled and rolled-annealedalloys

Rolled Alloys

The textures of rolled alloys are presented in Figs. 4.18a-f. In general, all alloys present a basal texture in which most of grains are oriented such that their {0001} basal planes are fairly parallel to the sheet surface. However, the peak intensity of basal poles is positioned quite inclined from the sheet normal direction (ND) towards the rolling direction (RD) forming a two-pole basal texture. The formation of two-pole basal in rolling direction, has been previously attributed to the activation of <c+a> slip [27]. This is not readily acceptable since the splitting of the basal poles towards RD is seen more often in warm rolling of Mg alloys rather than in hot rolling, whereas, <c+a> slip occurs much more easily at higher temperatures. The phenomenon of basal-pole splitting has been also attributed to the formation of $\{10\bar{1}1\}$ compression twinning followed by $\{10\bar{1}2\}$re-twinning [28]. This hypothesis is more probable since the phenomenon happens usually at low temperatures and under high speed deformation, both of which encourage the formation of twins [26]. Closer observation of the microstructure also confirms the presence of twining even in annealed samples Fig. 4.19 (Fig 4.19a&b are the magnified view of the area inside the white square in Fig. 4.17b&f). This phenomenon seems to also be alloy dependent, since the authors have not observed the two-pole basal in M1 (Mg-1wt.%Mn) alloy and ME (containing Ce) alloys which rolled under the same condition [15].

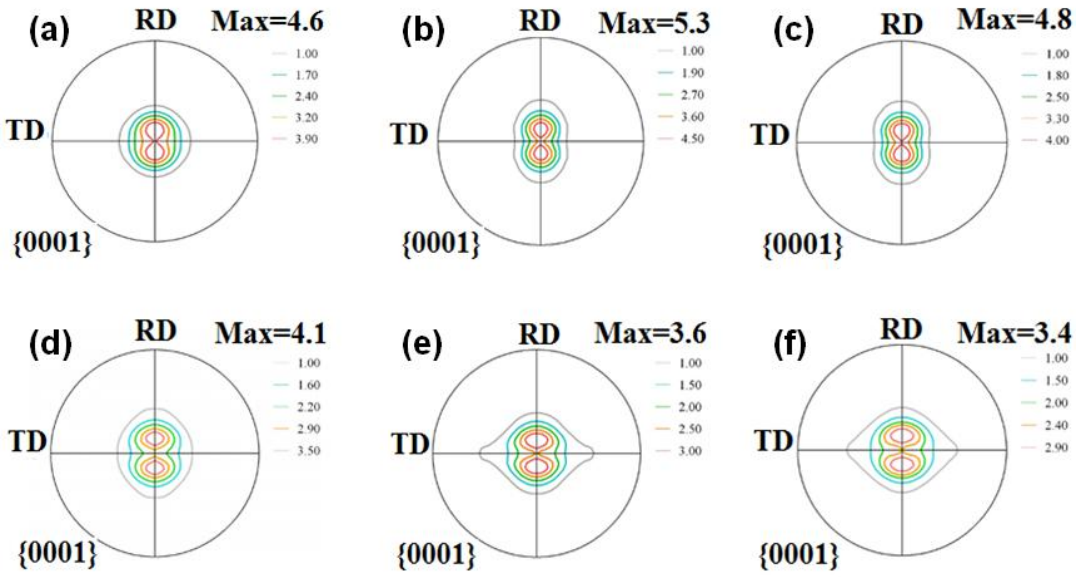

Fig. 4.18 Surface texture pole figures of alloys rolled at 400 ^{o}C: (a) AZ31, (b) Z1 (c) ZJ10(0.1Sr), (d) ZJ10(0.3Sr), (e) ZJ11(0.5Sr) and (f) ZJ11(1.0Sr).

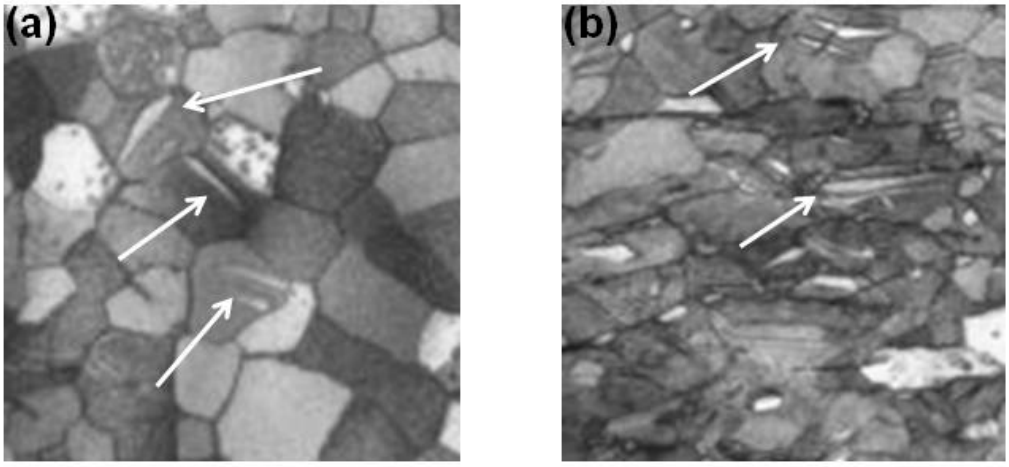

Fig. 4.19 *twins* in annealed a) Z1 b) ZJ11(1.0Sr).

The Z1 alloy had the strongest texture intensity of 5.3 multiples of a random distribution (MRD). The angular distribution of basal poles in Z1 was also broader towards the RD than towards the TD. The AZ31 alloy also had a basal texture, with the intensity of 4.6 MRD. This texture is typical of conventional AZ31B sheet [6-8]. The

weaker texture of AZ31 compared to Z1 alloy can be attributed to a higher density of shear bands in this alloy [29] (Fig. 4.17a). It has previously been shown that heavily deformed shear bands are preferential nucleation sites for the recrystallization of new grains with different orientations than that of the parent grains, which leads to texture randomization in some materials [29-31]. However, it should be noted that in Mg alloys, such a random texture within the shear bands makes them more prone to slip deformation, especially via basal slip. Consequently, grains within shear bands would soon gain a basal orientation (basal planes parallel to the sheet surface) upon further rolling. However, further deformation may also produce new shear bands where recrystallized grains within the newly formed shear bands contribute to the final weakened texture. Due to the relatively low volume fraction of newly generated shear bands, they would play a minor effect in texture weakening.

In a previous study Koike *et al.* [32] have shown that non-basal slip can be activated at grain boundaries. This was been attributed to plastic compatibility stresses at the grain boundaries [32]. It can be expected therefore, that the degree of non-basal activity would depend on the grain size in most Mg alloys. The weaker as-rolled texture of AZ31 alloy, compared to Z1 alloy, could also be attributed to finer grain size of AZ31.

Sr addition to the Z1alloy had a significant texture weakening effect, as indicated by the lower maximum texture intensity. This effect was minor in the ZJ10(0.1) alloy, since the addition of a higher amount of Sr further decreased the maximum intensity of the ZJ alloys, and at 1 wt.%Sr, the texture intensity was about two-thirds that of Z1 alloy. Another interesting aspect of texture evolution is that the (0001) texture contour of rolled ZJ11 alloys expanded in the transverse direction (TD) more than the rolling direction (RD). The addition of Sr had no significant effect on the angular distribution of basal poles in the RD, but the texture contour was significantly broadened in the TD, from 30^{o} in Z1 alloy towards 57^{o} at ZJ11(1 wt.%Sr).

In order to better quantify the pole spread in basal texture, the percentage of basal planes as a function of the angle of deviation ($\Delta\theta_{ND}$) from the sheet normal direction (ND) were plotted (Fig. 4.20). As shown, the addition of Sr reoriented the basal planes away

from the sheet ND when compared with the Z1 alloy. In other words, the percentage of basal planes that have an orientation away from the ND increased. With Sr > 0.3 wt.%, the $\Delta\theta_{ND}$ of basal-pole peak intensity in ZJ alloys moved from $\pm 15^{o}$ as seen in Z1, ZJ10(0.1Sr) and AZ31, to $\pm 25^{o}$.

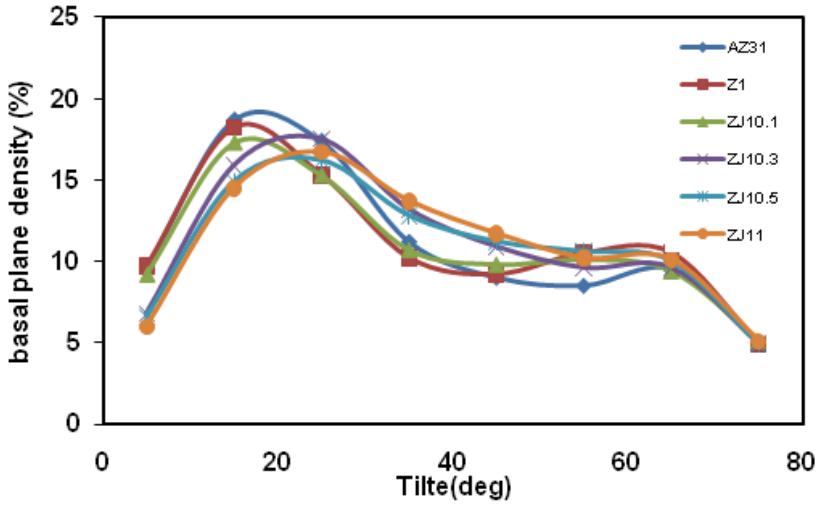

Fig. 4.20 Density of basal planes versus deviation angle from sheet normal direction in as-rolled condition.

Rolled-annealed

The texture of annealed AZ31 (Fig. 4.21a) was similar to that of the rolled alloy shown in Fig. 4.18a. The maximum texture intensity of Z1 and ZJ alloys was somewhat reduced by annealing at 400 ^{o}C for 5 mins. The pole figures of annealed Z1 and ZJ alloys resemble those of rolled samples, but the basal contours in the rolled-annealed samples are broader (both in TD and RD). As an example it can be seen that the contour in the pole figure of ZJ11(0.5Sr) spreads in TD from 58^{o} to 72^{o} and in RD from 43^{o} to 45^{o}.

In this study, samples were reheated between rolling steps, through which static recrystallization may have occurred, that may in turn have induced a change in texture. This would suggest that the grains formed due to partial recrystalization may have an orientation different from the parent grains; this would partially explain the texture

weakening observed for rolled alloys [11, 16, 17, 26, 33]. This idea is discussed in more detail in the following section "The Mechanism of Texture Evolution".

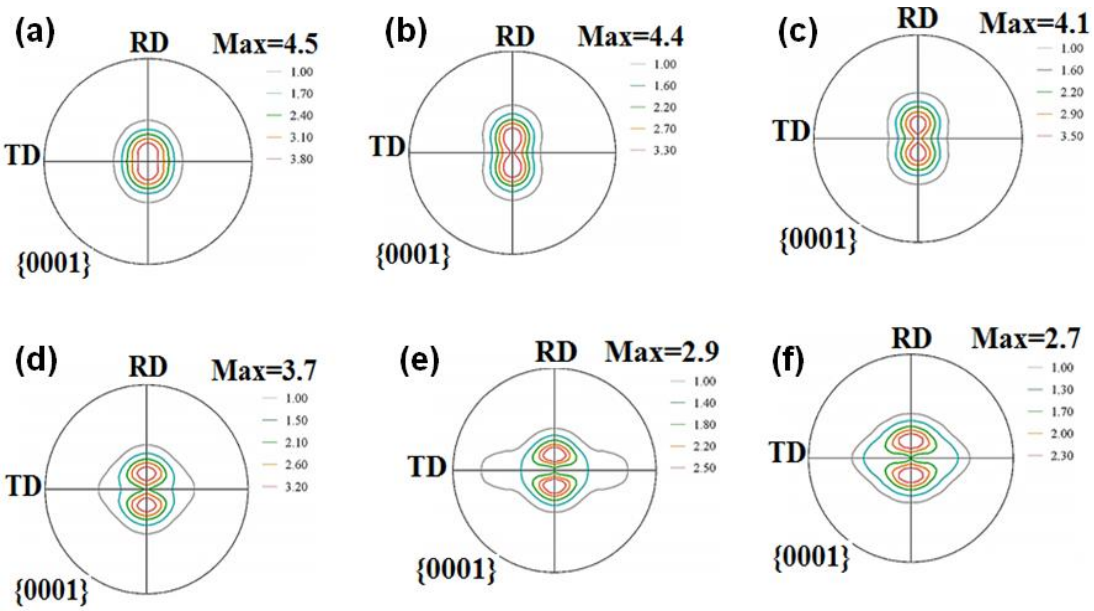

Fig. 4.21 Surface texture pole figures of alloys rolled and annealed at 400 ^{o}C for 5 min: (a)AZ31, (b) Z1 (c) ZJ10(0.1Sr), (d) ZJ10(0.3Sr), (e) ZJ11(0.5Sr) and (f) ZJ11(1.0Sr).

4.3.3.4 The Mechanism of Texture Evolution in ZJ Alloys

Texture weakening (randomization) in Mg alloys has been attributed to different mechnisms. Previously, texture weakening was related to abnormal grain growth [34]. This does not appear to have occurred here since the recrystallized grain structures of the ZJ alloys in this study were all quite uniform.

It is well known that the axial (*c/a*) ratio effects the deformation and texture of HCP metals [35]. In HCP metals, the *c/a* ratio effects the difference in the critical resolved shear stress (CRSS) between basal slip and non-basal slips. The reduction of *c/a* can enhance the activity of the non-basal slip in Mg alloys [36]. The *c/a* ratio of 1.624, as in Mg, results in low CRSS on the basal plane, favouring basal slip. Ti on the other hand with a much lower *c/a* ratio (1.58) than Mg, has a high basal CRSS but low prismatic CRSS [36], this causes the spread of basal poles towards the TD direction. It is known

that solutes in solid-solution can alter the axial ratio of Mg [37], however, this cannot be the case for ZJ alloys, since Sr does not have any considerable solubility in Mg at the rolling temperatures used in this study (400 ^{o}C), which means that it cannot significantly influence the lattice parameters. This is further substantiated by the fact that the presence of small amounts of Sr (0.1wt.%) did not produce a similar expansion in texture contour; on the contrary, high levels of Sr well above any possible solid-solubility limit lead to the basal pole spread towards TD.

Particles, depending on their size, spacing and amount, can increase the driving force for recrystallization and act as nucleation sites by locally accumulating strain [26, 38]. It is well known that gliding dislocations do not shear non-coherent precipitates. As a result, dislocation pile-up or looping at the particle/matrix interface occurs. The polarity of the tension-compression strain fields of these dislocations leads to the local bending of the crystal at the precipitate-matrix interface. The local strain (and bending) is relieved by the formation of cell and sub-grain formation upon annealing. The sub-grains that form during the recovery stage coalesce through rotation according to the five-degrees of freedom of low-angle boundaries (tilt, twist, rotation) and nucleate into new grains with substantially different orientations than that of the parent grain, thereby leading to texture weakening [39]. When recrystalization is assited by particles, this mechanism is known as particle-stimulated nucleation (PSN) [26]. This recrystallization mechanism is different from the grain-boundary bulging mechanism that results in recrystallized grain orientations closely associated with those of the parent grains. It was shown that during static recrystallization, stringers of second phases are more effective than dispersed particles in taking part in PSN, where particle stringers act successfully as one very large particle [26].

In this study, samples were reheated between rolling steps. Generally it is thought that recrystallization textures do not significantly change in Mg alloys. However, recent studies have shown that texture alteration can occur during recrystallization of Mg alloys [11, 16, 17, 33]. Previously, Masoumi *et al.* [16, 17] have shown that particle-stimulated nucleation can be responsible for the rotation of basal poles towards TD in twin-roll-cast AZ31 sheet when annealed. In this study, static recrystallization may have occurred

through reheating of specimens between rolling steps. The newly formed grains in a partially recrystallized structure may have had an orientation different from the parent grains, which may explain the observed texture weakening in the rolled alloys.

Since Sr produces second phases which are thermally stable at the rolling temperature (400 ^{o}C) and their amount increases with increasing Sr (which increases the potential sites for PSN), it could be inferred that that the second phases led to PSN in ZJ alloys, causing texture weakening and as a result causing basal pole rotation towards TD. Indeed, it was observed that there was a close association between some of the recrystallized grains and stringers (as shown by arrows in Figs. 4.17 e&f). In these areas, the recrystallized grains grew until they impinged upon another row of stringers or newly recrystallized grains.

To verify the interaction of the particles with the recrystallized grains, EBSD analysis was performed on ZJ11(1.0Sr) annealed at 400 ^{o}C for 3 min, i.e., a duration that is not sufficiently long to attain a fully recrystallized structure (Figs. 4.22 a-b). Fig. 4.22b is the magnified view of the area indicated by the white square in Fig. 4.22a. In these two figures, the high angle boundaries (>15^{o}) and low angle boundaries (>3^{o}) are delineated with black and white lines, respectively. Some small recrystallized grains, with little or no deformation sub-structure typical of strain-free recrystallized grains, associated with stringer can be observed in Fig. 4.22b. It can also be clearly observed that the recrystallized grains associated with precipitates exhibited a random texture.

Figs 4.22 c&d show the pole figure from one of the parent grains (grain A in Fig. 4.22b) and the recrystallized grains next to stringer (area inside the white oval in Fig. 4.22b). As seen in Fig. 4.22c, the parent grains showed a near basal texture, whereas the recrystallized grains (Fig 4.22d) showed a much wider spread of orientations. This confirmed that the new recrystallized grains assisted by PSN had a different orientation which contributed to texture weakening. It should be mentioned that some of the recrystallized grains are adjacent to high angle boundaries and are likely to have nucleated through the grain boundary bulging mechanism. These grains have orientations very similar to those of the parent grains (shown in Fig 4.22b with white circle). We conclude that the nucleation of new grains in the ZJ alloys was associated with both grain

boundaries bulging and second phase particles, and that the latter leads to texture weakening.

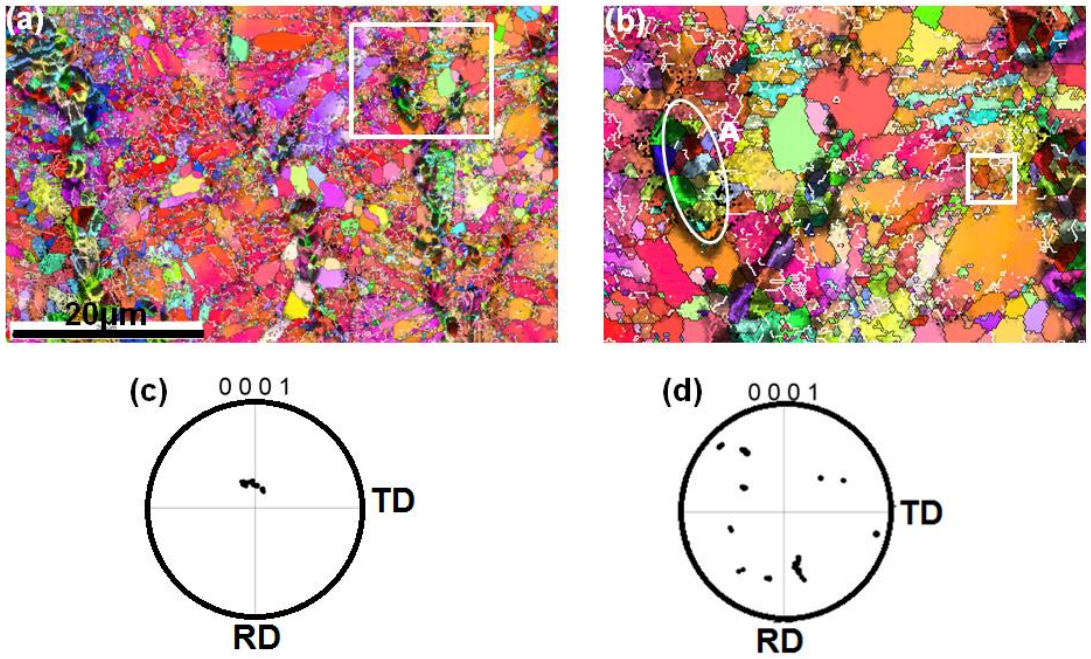

Fig. 4.22 The ZJ11(1.0Sr) after annealing for 3 min at 400 °C: (a) EBSD map on the RD–TD plane and (b) magnified area in the white square c) texture pole figure of grain A d) texture pole figure of fine grain close to stringer.

4.3.4 Conclusions

This study investigated the microstructure and texture of Mg-Zn-Sr in as-cast and rolled and annealed conditions. The following information was attained:

1. As-cast Z1 and ZJ alloys are mainly characterized by equaiaxed grains; however, the grains are refined by the addition of Sr.
3. Annealing reduced the grain size, this reduction increased with an increase in Sr, suggesting that second phase particles have an effect on grain growth.
4. The basal texture prevailed in rolled and annealed alloys; however, the addition of Sr significantly reduced the texture intensity.
5. Texture weakening is attributed to particle stimulated nucleation.

4.3.5 References

1. B. Engl, , Light Metal Age, 2005. 63(5), pp. 14-19.
2. M. Pekguleryuz and M. Celikin, Int. Mater. Rev. 55 (4) (2010), pp. 197–217
3. M. Pekguleryuz, P. Labelle, D. Argo, J. Adv. Mater. & Proc., 2003. 35(3): pp. 32-38.
4. E. J. Vinarcik, Light Metal Age., 2004. 62(3-4): pp. 56-57.
5. E. Doege, , K. Droder, , J. Mater. Process. Technol., 2001. 115: pp. 14–19
6. A. Jager, P. Lukac, V. Gartnerova, J. Haloda, M. Dopita, Mater. Sci. and Eng. A 2006. 432: pp. 20–25.
7. F. Kaiser, J. Bohlen, D. Letzig, K.-U. Kainer, A. Sfyczynski, C. Hartig, Adv. Eng. Mater., 2003. 5(12): pp. 891-896.
8. M.R. Barnett, M.D. Navea, C.J. Bettlesb, Mater. Sci. Eng. A 2004. 386: pp. 205–211.
9. E. Yukutake, J. Kaneko M. Sugamata, , J. Jpn Soc. Technol. Plast. 2003. 44: pp. 276-280.
10. L.W.F. Mackenzie, M. Pekguleryuz, Mater. Sci. Eng. A, 2008. 480(1-2): pp. 189-197.
11. L.W.F. Mackenzie, M.O. Pekguleryuz, Scr. Mater., 2008. 59(6): pp. 665-668.
12. J. Bohlen, M.R. Nürnberg, J.W. Senn, Letzig, D., S.R. Agnew, Acta Mater., 2007. 55(6): pp. 2101-2112.
13. R. K. Mishra, A. K. Gupta, P. R. Rao, A. K. Sachdev, A. M. Kumar, A. A. Scr. Mater., 2008. 59(5): pp. 562-565.
14. N. Stanford, M. Barnett, Scr. Mater., 2008. 58(3): pp. 179-182.
15. M. Masoumi, M. Hoseini, M. Pekguleryuz, Mater. Sci. & Eng. A, 2011, 528, (7-8): pp. 122-3129.
16. M. Masoumi, F. Zarandi, M. Pekguleryuz, Scr. Mater., 2010, 62 (2010), pp. 823–826
17. M. Masoumi, F. Zarandi, M. Pekguleryuz, Mater. Sci. and Eng. A, 2011, 528 (3), pp. 1268-127
18. M. M. Avedesian, H. Baker, , Magnesium and Magnesium Alloys 1999: ASM International, Materials Park, OH 44073-0002, USA, . pp. 314.
19. J.E. Gruzleski, A. Aliravci, Low Porosity, Fine-Grain Sized Strontium Treated Magnesium Alloy Castings, US Patent US005143564A. Sep 1992.

20. M. Fujita, N. Sakate, S. Hirahara, Y. Yamamoto, SAE Paper 950422. 1995 doi:10.4271/950422.
21. P. Cao, D. H. StJohn, M. Qian, Mater. Sci. Forum, 2005. 488-489: pp. 139-142.
22. P. Zhao, Q. Wang, C. Zhai, Y. Zhu, Mater. Sci. and Eng. A, 2007. 444(1-2): pp. 318-326.
23. J. Bai, Y. Sun, Shan, X. Feng, Xue, T. Zhu, Mater. Sci. and Eng. A,, 2006. 419(1-2): pp. 181-188.
24. C.A.,Aliravci, J.E. Gruzleski, F.C. Dimayuga, AFS Transactions, 1992: pp. 92-115.
25. P. Villars, L.D. Calvert and W.B. Pearson, Pearson's Handbook of Crystallographic Data for Intermetallic Phases, American Society for Metals, Metals Park, OH (1985)
26. F.J. Humphreys and M. Hatherly, Recrystallization and Related Annealing Phenomena (2nd ed.), Great Britain by Galliard Ltd., UK (2004).
27. S.R. Agnew, M.H. Yoo, C.N. Tomé, Acta Metall., 2001. 49(20): pp. 4277-42
28. S.L. Couling, J.F.Pashak, L. Sturkey, Trans ASM, 1959. 51: pp. 94-107.
29. X. Huang, K. Suzuki, A. Watazu, I. Shigematsu, N. Saito, J. Alloys Compd., 2008. 457(1-2): pp. 408-412.
30. H. Paul, J. H. Driver, Z. Jasienski, Acta Mater., 2002. 50(4): pp. 815-830.
31. N. Stanford, and M.R. Barnett, Mater. Sci. Eng. A, 2008, 496(1-2): pp.399-408
32. J. Koike, T. Kobayashi, T. Mukai, H. Watanabe, M. Suzuki, K. Maruyama, K. Higashi, Acta Metall., 2003. 51(7): pp. 2055-2065.
33. L.W.F. MacKenzie, B. Davis, F.J. Humphreys and G.W. Lorimer, Mater. Sci. Technol. 23 (10) (2007), pp. 1173–1180.
34. G.T. Higgins, J. Nucl. Mater. 8 (1963), pp. 153.
35. Y. N. Wang, and J. C. Huang, Mater. Chem. Phys., 2003. 81(1): pp. 11-26.
36. G.V. Raynor, The Physical Metallurgy of Magnesium and its Alloys. 1959, New York: Pergamon Press.
37. A. Becerra and M. Pekguleryuz, Effects of lithium, indium, and zinc on the lattice parameters of magnesium. J Mater Res, 2008. 23: pp. 3379.
38. F.J., Humphreys, Acta Metall., 1977. 25(11): pp. 1323-1344.

39. R. E. Reed-Hill, R.Abbaschian, Physical Metallurgy Principles. Third ed, 20 Park Plaza, Boston, MA: PWS.

4.4 A Look at Texture Alteration Micro-Mechanisms in the Mg alloys Studied in this Thesis

PSN has been determined to be the main mechanism for texture weakening observed for annealed TRC AZ31 as well as MJ and ZJ alloys. On the other hand, ME alloys also show weaker textures but do not exhibit PSN. In order to shed some light into these differences, some of the salient features of these alloy systems have been compiled. Table 4.5 presents the second phases (experimental and calculated), the elevated temperature solubility limits of the alloying elements, and the main second phase particles which could be responsible for PSN, estimated using EPMA and FactSage results.

The texture alteration in annealed TRC AZ31 was related to a higher amount of second phase particles that formed upon Scheil solidification, when compared to conventional AZ31. However, this texture alteration was not observed in rolled-annealed TRC AZ31, as most of the second phases dissolved in the matrix due to annealing at 420 ^{o}C followed by rolling at 400 ^{o}C. Also, in MJ and ZJ alloys it was observed that as the amount of second phase particles increased the texture intensity was reduced; this could be due to higher amount of available PSN sites. However, in ME alloys it was observed that an increase in the amount of intermetallics did not lead to a continuous increase in texture weakening, ruling out PSN as the mechanism for weaker textures in these alloys. The mechanism was instead concluded to be associated with the solubility of Ce in Mg. Second phase particles in MJ and ZJ after rolling were detected as $Mg_{17}Sr_2$ and Sr_5Si_3, whereas $Mg_{12}Ce$ was present in ME alloys. The following explanations for PSN arise from these results:

1. A significant amount of second phase particles are needed to achieve an observable amount of texture weakening via PSN.
2. Only certain intermetallics lead to PSN.
3. Other mechanisms become dominant in certain alloys and prevent PSN.

Table 4.5 second phases in Mg sheet alloys studied in this work [4-7].

Alloy/ texture weakening mechanism	**Maximum Solubility (wt.%)**	**Solubility at 400 C (wt.%)**	**Second phases (Factsage)**	**Second phases (Factsage) / Scheil mode**	**Second phases (EPMA) As-cast**	**Second phases (EPMA) Rolled**	**Stringer Phases** (via EPMA & FactSage)
AZ31 annealed/ none				$(Al,Zn)_{49}Mg_{32}$			$(Al,Zn)_{49}Mg_{32}$ Al_5Mn_8
TRC AZ31 annealed/ PSN				$(Al,Zn)_{49}Mg_{32}$	Mg-Al-Zn, Mg-Al, Al-Mn		$(Al,Zn)_{49}Mg_{32}$ Al_5Mn_8
M1/none					Mg-Si, Mn-Si	Mn, Mn-Si	α-Mn, $MnSi_3$
Z1/none			Mg_2Si	Mg_2Si, $Mg_{51}Zn_{20}$	Mg-Zn		$Mg_{51}Zn_{20}$
ME11(0.5Ce)/Solute drag	0.74 (0.13at%) at 590°C	0.08 (0.014 at%)	$Mg_{12}Ce$		Mg-Ce, Mn-Si-Ce Mn-Ce Mn-Si	Mn-Ce, Mg-Ce	$Mg_{12}Ce$ α-Mn(Ce)
ME11(1Ce) / Solute drag	0.74 (0.13at%) at 590 °C	0.08 (0.014 at%)	$Mg_{12}Ce$ $CeSi_2$		Mg-Ce, Mn-Si-Ce Mn-Ce Si-Ce		$Mg_{12}Ce$ α-Mn(Ce)
MJ11(0.5Sr)/ PSN	0.11 (0.03at%) at 585 °C	0	Mn_3Si, Mn_6Si, Mn_9Si_2, $Mg_{17}Sr_2$	Mn_3Si, Mn_5Si_3, Mn_9Si_2, $Mg_{17}Sr_2$ Sr_5Si_3	Sr-Si, Mg-Sr		Sr_5Si_3 ($Mg_{17}Sr_2$*)
MJ11(1Sr) / PSN	0.11 (0.03at%) at 585 °C	0	Mn_3Si, Mn_6Si, Mn_9Si_2, $Mg_{17}Sr_2$	Mn_3Si, Mn_5Si_3, Mn_9Si_2, $Mg_{17}Sr_2$ Sr_5Si_3	Sr-Si, Mg-Sr		Sr_5Si_3 $Mg_{17}Sr_2$*
ZJ11(0.5Sr) / PSN	0.11 (0.03at%) at 585 °C	0	Zn-Sr-Si Sr-Si Zn-Sr	Mg_2Si, SrSi, Sr_5Si_3, $SrZn_5$	Sr-Si, Mg-Sr	Sr-Si	Sr_5Si_3, ($Mg_{17}Sr_2$*)

* Though $Mg_{17}Sr_2$ is not seen in EPMA of rolled samples, it cannot be entirely excluded.

One explanation of the different mechanism of texture weakening in ME compared to MJ and ZJ alloys, may be the fact that $Mg_{12}Ce$ is quite different from the other intermetallics ($Mg_{17}Sr_2$ or Sr_5Si_3) in the other alloys, and that it does not play a role in PSN. $Mg_{12}Ce$ has been recently redesignated as $Mg_{11}Ce$ [1, 2] which has a tetragonal $ThMn_{12}$ (Pearson symbol tI26) vacancy defect structure with crystal parameters a=1.03 nm and c=0.60 nm and has a melting point of ~616°C. $Mg_{17}Sr_2$ has a hexagonal $Ni_{17}Th_2$ structure (Pearson symbol hP38) with crystal parameters of a=1.0533nm c=1.0341nm and has a melting point of ~609°C. On the other hand, Sr_5Si_3 is a high temperature

intermetallic (melting point 1150^{o}C) with Cr_5B_3-type crystal structure (Tetragonal, I4/mcm) with crystal parameters of a=0.8055 nm and c=1.5688 nm [3]. In AZ31, $(Al,Zn)_{49}Mg_{32}$ has a cubic structure with structure parameter of 1.4 nm. These data are summarized in Table 4.6 along with Mg crystal structure data.

Table 4.6 Crystal structure and parameters of second phase particles in this study [4,8].

Phase	**Crystal structure**	**Crystal parameters (**nm)
Mg	HCP	a=0.32, c=0.52
$Mg_{17}Al_{12}$	BCC	a=1.05
$(Al,Zn)_{49}Mg_{32}$	BCC	a=1.4
$Mg_{12}Ce$	Tetragonal	a=1.03, c=0.60
$Mg_{17}Sr_2$	HCP	a=1.05, c=1.03
Sr_5Si_3	Tetragonal	a=0.805, c=1.56

As explained in previous chapters, in order for PSN to occur, dislocation pile-up or looping at the particle-matrix interface is needed. It has been established that non-coherent or semi-coherent precipitates which are not sheared by dislocations can accumulate plastic strain at the interface. From the data in table 4.6 it may be concluded that $Mg_{12}Ce$ would act as a semi coherent particle, with near coherency at one edge (lattice parameter c for this phase and Mg is 0.6 and 0.52, respectively). However, the differences between the crystal parameters of Mg and other particles are much larger, hence these phases form non-coherent particles, which the dislocations cannot cut and can therefore accumulate sufficient strain for PSN to occur. Furthermore, the particle size plays an important role in PSN [9]. α-Mn particles are too fine to accumulate strain around them, so they would not lead to PSN. It would appear that a more detailed analyses of the behaviour of the particles during hot-rolling and of particle-dislocation interactions is required to determine the precise mechanism of action for this intermettalic.

As shown in Table 4.5, note that while Ce has a small but finite solubility in the Mg matrix, Sr has none. Ce may be interacting with basal dislocations, decreasing work hardening due to basal slip and activating other slip systems. Further analysis is required to determine the reasons why Ce as a solute is more effective than Al, Zn or Mn in activating other slip systems. Such an experiment would require a systematic study

involving TEM analysis, which is out of the scope of the current work, but would pose an interesting question for the basis of further studies.

4.4.1 References

1. X. Zhang, D. Kevorkov, I.-H. Jung, M. Pekguleryuz, J. Alloys Compd., 482(1-2), 2009, pp. 420-428
2. X. Zhang, D. Kevorkov, M. Pekguleryuz, J. Alloys Compounds, 2009. 475(1&2): pp. 361-367.
3. Palenzona and M. Pani, J. Alloys Compounds, 2004. 373: pp. 214–219.
4. P. Villars, L.D. Calvert and W.B. Pearson, Pearson's Handbook of Crystallographic Data for Intermetallic Phases, American Society for Metals, Metals Park, OH (1985)
5. H. Okamoto, J. of Phase Equilibria, 1991. 12(4): pp. 505–507.
6. A.A. Nayeb-Hashemi, J.B.C., Bull. Alloy Phase Diagr., 1986. 7 (2): pp. 149–155.
7. L. L. Rokhlin, Magnesium alloys containing rare earth metals : structure and properties. Vol. 3. 2003, London: Taylor & Francis
8. G. Bergman, J. L. T. Waugh and L. Pauling, Acta Crystallogr. 1957. 10, pp. 254.
9. F.J. Humphreys and M. Hatherly, Recrystallization and Related Annealing Phenomena (2nd ed.), Great Britain by Galliard Ltd., UK (2004).

CHAPTER 5

CONCLUSIONS

Detailed studies of the microstructural and texture evolution in Mg alloy sheet were carried out in this thesis. An experimental investigation of microstructure and texture development of twin-roll cast AZ31 was undertaken. Texture evolution in novel alloys was also investigated. Specifically, the effects of cerium and strontium on the microstructure and texture of Mg-1wt.%Mn and Mg-1wt.%Zn alloy were studied. The experiments were carried out by means of thermal analysis, optical microscopy, scanning electron microscopy (SEM), energy dispersive spectrometry (EDS), electron probe micro-analysis (EPMA), electron back scattered diffraction (EBSD) and X-ray diffraction (XRD) techniques. The following conclusions were made:

A. *The Effect of Cooling Rate on the Microstructure of AZ31 Magnesium Alloy*

The cooling rate (CR) experienced by TRC Mg sheet varies from the sheet surface to the sheet mid-thickness, which in turn produces a non-uniform grain structure. AZ31 is the only TRC Mg sheet alloy which is industrially produced in small amounts globally. The effect of changing the CR from 0.55 to 38 ^{o}C/s on the microstructure of AZ31 was systematically studied and general relationships were determined between the CR and the salient features of the microstructure. As the cooling rate increased from 0.55 to 38 ^{o}C/s:

1) The grain sizes of Mg alloy AZ31 decreased.
2) The secondary arm spacing SDAS became finer. A relationship between secondary denrite arm spacing, μm, and the cooling rate, CR was established as $\lambda = 85.15\ (CR)^{-0.42}$.
3) The fraction area of secondary phases increased; this is attributable to non-equilibrium Scheil solidification mode.
4) The size of the second phase particles decreased from ~7 to ~1.5 μm.

B. *Microstructure and Texture Studies on Twin-Roll Cast AZ31*

AZ31 alloy sheet is drawing the interest from automotive companies for the fabrication of light-weight vehicle body structures. In order to reduce the microstructural defects and improve magnesium formability, a thorough understanding of microstructure and texture evolution of TRC Mg sheet is necessary. To date, very few academic studies exist regarding the microstructure and deformation structures of twin-roll cast AZ31. This study generated important knowlegde regarding the unique metallurgical structure of TRC AZ31, specifically:

1. The CR near the sheet edge (surface) was at rapid solidification rate (325 ^{o}C/s), while the mid-thickness solidified by a Scheil solidification mode (150 ^{o}C/s).
2. As a result of varying the CR:
   a. The as-cast structure of TRC AZ31 sheet was mainly characterized by large dendritic columnar grains along with small equiaxed grains near the edge and the mid-thickness of the sheet.
   b. As a result of the rapid solidification rate, the sheet surface was depleted of second phases due to solute supersaturation, while the amount of second phases in the mid-thickness was higher than the equilibrium amount.
   c. Macrosegregation of Al, Zn and Mn was observed in the centerline of the sheet.
3. A basal texture prevailed in the as-received TRC sheet due to the rolling deformation applied during the TRC process. It was found that the large grains, predominant in the structure, were the main contributors to the overall basal texture of the sheet, even though the small grains had a random texture. This basal texture is undesirable since it accentuates the limited formability of Mg due to its hexagonal close-packed crystal structure.
4. A significant finding of this thesis is the design of a post TRC annealing treatment that weakens the basal texture. Annealing at 420 ^{o}C alleviated the basal texture in the TRC AZ31 sheet, thereby improving the ductility and the strain-hardening response (*n*-value).

C. *The influence of Ce and Sr on the Microstructure and Rolling Texture of Mg-1wt./%Mn and Mg-1wt./%Zn alloys*

The introduction of alloying additions that can alter or weaken the undesirable basal texture in Mg sheet alloys, with the purpose of improving sheet formability, is a significant contribution of this thesis. Mg-Mn and Mg-Zn binary alloys show good rollability and weldability. These alloys were selected as base alloys to which Ce and Sr were added for texture weakening.

Mg-Mn-Ce

1. The grain and microstructures of the hot rolled sheet alloys were determined:
    a. As-cast Mg-1wt%Mn (M1) and Mg-1%Mn-x%Ce (ME) alloys characterized mainly by large columnar grains; however, the grains were significantly refined by the addition of Ce.
    b. All alloys partially recrystallized during hot rolling with the additional feature of shear bands and twins.
    c. Alloying with Ce had a minor effect on annealing grain size, suggesting that the second phase particles have a minor effect on grain growth.
2. The basal texture prevailed in rolled and annealed sheet; however the addition of Ce significantly reduced the texture intensity. Texture weakening was related to the solid solubility of Ce in Mg.

Mg-Mn-Sr

1. The grain and microstructures of the hot rolled sheet alloys were determined:
    a. As-cast Mg-1wt%Mn (M1) and Mg-1%Mn-x%Sr (MJ) alloys are characterized mainly by large columnar grains; however, the grains were significantly refined by addition of Sr.
    b. All alloys partially recrystallized during hot rolling with the additional feature of twinned structure.
    c. Alloying with Sr slightly refined the grain size of the rolled-annealed MJ alloys.

2. The basal texture prevailed in rolled and annealed sheet; however, the addition of Sr significantly weakened the texture intensity. The particle stimulation nucleation during recrystallization has been determined to be the mechanism causing this effect.

Mg-Zn-Sr

1. The grain and microstructures of the hot rolled sheet alloys were determined:
   a. As-cast Mg-1wt.%Zn (Z1) and Mg-1%Zn-x%Sr (ZJ) alloys exhibited equiaxed grains; however, the grains were significantly refined by addition of Sr.
   b. Rolled Z1 and ZJ alloys exhibited a heavily deformed structure, however Z1 alloy had shear band characteristics.
   c. Alloying with Sr refined the grain size of the rolled-annealed MJ alloys, suggesting that second phases have a pinning effect.
2. The basal texture prevailed in rolled and annealed sheet; however, the addition of Sr significantly reduced the texture intensity. The mechanism of texture evolution was determined to be particle stimulation nucleation during recrystallization.

Recommendations for Future Work

1. The effect of Ce addition on stacking fault energy of Mg should be investigated.
2. Mg-Mn-Sr and Mg-Zn-Sr alloy compositions should be optimized to exhibit the ideal combination of weak texture and acceptable rollability and mechanical properties..
3. The reasons why the second phases in Mg-Mn-Ce did not lead to PSN, while the second phases in all other alloys did contribute to PSN should be investigated.
4. The effect of Ce and Sr on the texture of AZ31, the most common Mg sheet alloy, should be studied.
5. The microstructure and texture of Mg-Mn-Sr and Mg-Zn-Sr alloys should be studied in the twin-roll cast condition.

CHAPTER 6

CONTRIBUTIONS TO ORIGINAL KNOWLEDGE

This thesis offers a broad, new perspective regarding the microstructure and texture development during hot-rolling of magnesium alloys, which can be categorized as:

1. An understanding of AZ31 sheet alloy with respect to the development of its downstream rolling microstructure and texture under a wide variety of initial casting conditions including twin-roll casting, and the effect of annealing to create weak rolled and annealed sheet textures in twin-rolled cast AZ31 alloy,
2. The application of alloy modification to create weak rolling/annealing textures in a number of new magnesium alloy compositions. The resulting weak textures potentially improve the formability of magnesium sheet.
3. An understanding of the mechanisms of weak texture development in a number of rolled magnesium alloys.

The detailed contributions of the study are:

AZ31 alloy

1. The effect of initial cooling rate on the microstructure of the main sheet alloy AZ31 was investigated for the first time.
2. The alleviation of basal texture TRC-AZ31 by post-annealing, leading to higher ductility and improved strain hardening response was reported for the first time.
3. This study also explains in detail the metastable microstructure of the TRC AZ31 alloy and how this can lead to P of new strain free grains during post-annealing treatment, which contributes to the randomization of the texture.

Novel magnesium alloys

4. Ce was added to create sheet textures with weaker preferred orientations than the Mg-Mn base alloy. The texture weakening of Mg-Mn-Ce compared to Mg-Mn was attributed to the solid solubility of Ce in Mg rather than particle stimulated nucleation (PSN) or *c/a* ratio alteration.
5. Sr was applied for the first time to weaken the Mg sheet texture. This addition was used on a Mg-Mn base alloy and a Mg-Zn base alloy. The mechanism of weak texture development in Mg-Mn-Sr and Mg-Zn-Sr alloys was attributed to PSN of new grains at second phase stringers.

APPENDIX

SIGNED WAIVERS FROM ANY CO-AUTHORS OF UNPUBLISHED MANUSCRIPTS